DISSERTATION

Strong light-matter interactions and exciton-polaritons in carbon nanotubes

ARKO GRAF

A thesis submitted to the

COMBINED FACULTY OF
NATURAL SCIENCES AND MATHEMATICS

HEIDELBERG UNIVERSITY, GERMANY

A thesis submitted for the degree of

DOCTOR RERUM NATURALIUM

Date of examination

APRIL THE TWENTY-SIXTH, 2019

Strong light-matter interactions and exciton-polaritons in carbon nanotubes

1. Gutachter: Prof. Dr. Jana Zaumseil
2. Gutachter: Prof. Dr. Malte C. Gather

Je planmäßiger die Menschen vorgehen,
desto wirksamer vermag sie der Zufall treffen.
(Friedrich Dürrenmatt, Die Physiker)

Abstract

Exciton-polaritons are quasiparticles with hybrid light-matter character, offering a unique combination of photonic properties, such as a light mass, with those of excitons, for example strong nonlinearities and fast relaxation. Strong light-matter coupling enables a rich set of polaritonic quantum phenomena as well as applications. While originally observed in inorganic materials, organic semiconductors have recently attracted tremendous attention since their large oscillator strength facilitates particularly strong light-matter coupling and enabled polariton formation at room temperature. In particular, electrical excitation is pursued to apply these quantum-mechanical effects in practical polariton devices. However, a lack of organic materials with sufficiently high charge-carrier mobility and suitable device architectures impede their full utilization.

Nanomaterials, in particular low-dimensional materials, present a novel material class that combines the excitonic properties of organic and electric characteristics of inorganic materials. In this thesis, single-walled carbon nanotubes (SWCNTs) were employed to demonstrate, for the first time, exciton-polariton formation in the near infrared (nIR) at room temperature. SWCNTs are identified as an ideal material facilitating strong light-matter coupling due to their high oscillator strength. Moreover, by implementing a strongly coupled microcavity into a light-emitting field effect transistor (LEFET), electrically pumped polariton emission at high current density was observed. These practical polariton devices emit in ranges relevant for telecommunication and support high currents due to the excellent optoelectronic properties of SWCNTs. Pumping polaritons at high rates presents a major step towards electrical lasing with carbon-based materials.

For the realization of these experiments it was crucial to overcome current limitations in post-growth sorting of SWCNTs, which are intrinsically restricted to low-volume and damage the nanotubes. For this purpose, selective polymer wrapping by high-speed shear-force mixing, which can be easily scaled up, was developed. By using shear forces, the SWCNT-yield was drastically increased while, at the same time, the SWCNT-quality could be improved. In addition to strong light-matter coupling and polariton emission, the selected SWCNTs were employed in organic light-emitting diodes. These devices showed pure nIR emission with narrow linewidth at efficient electrical performance. This work paves the way for fundamental investigations as well as advanced applications of SWCNT-based optoelectronic devices.

ZUSAMMENFASSUNG

Exziton-Polaritonen sind quantenmechanische Quasiteilchen, die hybride Eigenschaften von Licht und Materie vereinen. Dadurch können z.B. die geringe Masse von Photonen (Licht) mit den Nicht-Linearitäten und der schnellen Relaxierung der Exzitonen (Materie) kombiniert werden. Die Polaritonen, welche durch die starke Licht-Materie-Wechselwirkung entstehen, ermöglichen die Erforschung neuartiger, quantenmechanischer Phänomäne sowie vielfältiger Anwendungen. Während zunächst anorganische Materialien verwendet wurden, werden nun zunehmend organische Halbleiter untersucht. Letztere ermöglichen, durch ihre große Oszillatorstärke und Exzitonenbindungsenergie, das Auftreten von besonders großen Wechselwirkungen bei Raumtemperatur. Um elektrische Bauelemente auf Grundlage von Polaritonen herzustellen, ist die elektrische Anregung der Quantenteilchen erforderlich. Deren weitere Entwicklung wird durch das Fehlen von organischer Materialien mit ausreichend hohen Ladungsträgertransport sowie einem geeingeten Aufbau eines solchen Bauelemente verzögert.

Nanomaterialien mit verringerter Dimensionalität können exzitonische Eigenschaften von organischen mit den elektronischen Charakteristika von anorganischen Materialien kombinieren. Im Rahmen dieser Dissertation wurden einwandige Kohlenstoffnanoröhrchen (Single-Walled Carbon Nanotubes - SWCNTs) für die erstmalige Erzeugung von Exziton-Polaritonen im nahen Infratrotbereich bei Raumtemperatur eingesetzt. SWCNTs wurden dabei, durch ihre besonders große Oszillatorstärke, als ideales Material für starke Licht-Materie Wechselwirkung identifiziert. Desweiteren wurden diese Exziton-Polaritonen elektrisch erzeugt, wobei besonders hohe Stromdichten erreicht wurden. Dies wurde durch eine erfolgreiche Integration der stark gekoppeleten Kavitäten in lichtemittierende Feldeffekttransistoren erreicht. Die außergewöhnlichen optoelektronischen Eigenschaften von SWCNTs ermöglichen, neben dem Betrieb unter sehr hohen Ladungsträgerdichten, die Emission in anwendungsrelevanten Welllenlängenbereichen für optische Telekommunikation. Das Erzeugen von hohen Dichten an Polaritonen stellt dabei einen Meilenstein auf dem Weg zu elektrisch gepumpten Lasern mittels Kohlenstoff-basierten Materialien dar.

Für die erfolgreiche Umsetzung dieser Experimente war es essentiell einige Limitierungen, wie z.B. die geringen Ausbeuten/Volumina und die Schäden der SWNCTs während der Selektion, zu überwinden. Durch die Adaption der skalierbaren Methode des Scherkraftmixens für die Selektion mittels Polymerumwickelung konnten große Mengen an qualitativ hochwertigen SWCNTs selektiert werden. Die Benutzung von Scherkräften führte gleichzeitig zu einer deutlich gesteigerten Ausbeute im Vergleich zu herkömmlichen Methoden. Neben deren Verwendung für starke Licht-Materie Kopplung wurden diese SWCNTs auch erstmals als Emittermaterial in organischen Leuchtdioden verwendet. Diese elektrisch effizienten Leuchtdioden weisen eine schamlbandige Emission im nahen Infrarot auf. Die vorliegende Dissertation eröffnet neue Wege für die Erforschung grundlegender wissenschaftlicher Phänomene sowie weiterführenden Anwendungen von SWCNT-basierten optoelektronischen Bauteilen.

ACKNOWLEDGEMENTS

The scientific work presented in my thesis as well as my personal development would not have been possible and far less joyful without the people that supported, challenged and accompanied me during the past years.

Most of all I'm grateful for Prof. *Jana Zaumseil*'s and Prof. *Malte C. Gather*'s supportive guidance and mentorship throughout this time. Both have taught me how you can achieve your goals by being passionate, open-minded and thinking big. You have and will be my examples of living one's dream and enabling the people around you. Jana, thank you for your almost unconditional support even if it meant to move your lab across the globe in a trunk. Malte, I owe you a big part of my career path and I'm most grateful for your mentorship (even though I had to bring back Jana's lab equipment to Heidelberg).

I'm not less grateful to all members and alumni of the *nanomaterials for optoelectronics* (NMOE) group in Heidelberg and the *Gather lab* in Scotland. Spending day and night with you in the offices, labs and other spaces for leisure activities was my greatest pleasure. Learning from and with you was fantastic, my friends. Comrade *Yuriy Zakharko*, thanks for explaining to me how wavefunctions in botany enable communication with our nature. Darth Vader *Caroline Murawski*, thank you for working with me while risking your descendant. Judoka *Martin Held*, I enjoyed deep-diving into LEFETs with you. Doppelkopf-expert *Laura Tropf*, thank you for introducing me to the world of polaritons. Master *Jan Lüttgens*, I enjoyed drilling with you in basements. Best host *Markus Karl*, thank you for all. Champion Dr. *Nils Kronenberg*, I thank you for taking care of my backhand. Pivot player *Marcel Rother*, thank you for taking care of everything I didn't take care of even if it meant to absorb it with your shoulder. Hammonia *Max Brohmann*, thanks for going with me through the toughest miles. To all students that I had the opportunity to supervise (*Hoon*, *Tobias*, *Laura*, *Austin*, *Emma*, *Thinnes*, *Jan*, *Franziska*, *Eugen*, *Charles*, and *Victoria*): thank you for teaching me how to teach and how not to teach. To all other group and institute members: thank you for the wonderful time.

Last but not least, I want to thank all *collaborators* who inspired and supported me to go new paths. Among these are *Benjamin Flavel*, Prof. *Ralph Krupke*, *Moritz Pfohl*, Prof. *Christophe Voisin*, Prof. *Christoph Brabec* and many more.

Finally, I want to thank my *family*, *friends* and *girlfriend* for their love.

TABLE OF CONTENTS

List of Figures

CHAPTER 1

INTRODUCTION

The progress of humankind has always been linked to the control and understanding of light. Alongside the evolution of light sources from fire, to light bulbs and light-emitting diodes (LEDs), the principle of light generation evolved from burning to glowing and atomic transition. This evolution was accompanied by technological and scientific progress as well as the utilization of new materials. Nowadays, the control of light on an atomic scale is at the core of a broad application portfolio ranging from illumination and displays, through laser welding and micro structuring, to data storage and communication. In these practical devices, different materials are used for the generation, conversion, guidance and absorbance of light. Recently, a novel field has been unlocked for the application of light (photons) by mixing photonic properties with those of matter (excitons). Strong coupling between photons (light mass) and excitons (strong interactions) has led to the observation of quantum-mechanical phenomena, for example Bose-Einstein condensation (BEC), long-range coherence, superfluidity, and many more. The formed hybrid light-matter particles, called exciton-polaritons, pave the way to all-optical transistors and low-threshold lasers as well as tailoring chemical reactions and biological processes.

Exciton-polaritons were initially observed in inorganic materials. As these experiments are often restricted to low temperatures, require complex manufacturing or advanced optical excitation, their practical applications are limited. As an alternative, organic materials offer room temperature stability of polaritons as well as an ease of fabrication. Organic materials, however, come along with issues including their stability against heat, air and light; only moderate electrical conductivity; and the lack of efficient near-infrared emitters. Low-dimensional nanomaterials promise to bridge the gap between inorganic and organic materials. In particular, single-walled carbon nanotubes (SWCNTs) combine desirable properties of organic (carbon-based, room tem-

perature stability of excitons and solution processing) and inorganic materials (high electrical conductivity, high photo and thermal stability).

In this thesis, strong light-matter coupling of SWCNTs and surrounding metal-clad microcavities is shown for the first time. The required large amounts of purely semiconducting SWCNTs are selected by polymer wrapping using shear-force mixed dispersions. The suitability for electrical generation of light is verified by OLEDs based on SWCNT emitters resulting in pure near infrared electroluminescence. Electrical pumping and tuning of exciton-polaritons is achieved in cavity-integrated light-emitting field-effect transistor (LEFET). The excellent electrical performance of these LEFET-cavities enables pumping of exciton-polaritons at high rates – a major step towards practical polariton devices.

This thesis is organized as follows. In Chapter 2 the underlying theoretical principles and an overview of the current state of research are presented. These include the optoelectronic properties of SWCNTs, devices for electrical light generation based on solution-processed materials, and strong light-matter coupling and the formation of cavity exciton-polaritons. Next, Chapter 3 summarizes the utilized experimental methods used throughout this thesis including materials, experimental techniques and computational models.

As the base of the experimental work, Chapter 4 introduces the selective dispersion of high-quality SWCNTs by shear force mixing (SFM).[1] Compared to previous methods, SFM offers an effective and scalable technique to harvest large amounts of monochiral (6,5) SWCNTs in dispersion, which can be further processed into thin films by a range of deposition techniques. In Chapter 5, these SWCNTs are employed for the first demonstration of an OLED based on carbon nanotube emitters.[2] The OLEDs generate pure nIR emission at low voltages and exceptionally high outcoupling efficiency due to the in-plane orientation of the SWCNTs in the film.

Chapter 6 reports on strong light-matter coupling and the formation of optically excited exciton-polaritons in SWCNT-based microcavities.[3] SWCNTs are found to be an unique material for creating exciton-polaritons at room temperature and in the nIR due to the high binding energy of excitons in carbon nanotubes. Finally, Chapter 7 presents the results on strongly coupled LEFET-cavities using SWCNTs. In these devices, electrical pumping of exciton-polaritons is achieved at high densities.[4] At the same time, the LEFET-cavities can be utilized to tune the light-matter coupling and reversibly switch from strong to weak coupling.

This thesis concludes with an interpretation of the results in a broader context and an outlook on future research in Chapter 8. The advances, presented in this thesis, serve as proof-of-concept for further investigations. Among various future research paths, technological advances of strongly coupled LEFET-cavities needed for electrically pumped polariton lasers are discussed.

A comprehensive overview and review of the field of strong light-matter coupling in organic materials was published by the author of this thesis *et al.* in chapter nine of the *Handbook of Organic Materials for Electronic and Photonic Devices* (Ref. [5]).

CHAPTER 2

BACKGROUND

This chapter introduces the reader to the theoretical concepts and state-of-the-art in the research covered in this thesis. First, the optoelectronic properties of single-walled carbon nanotubes are derived from those of graphene and the experimental results in their excitonic structure review. Second, the principles of light-generating devices based on organic materials and their characterization are described. Last, the concept of strong light-matter coupling and exciton-polaritons is presented.

2.1 Single-walled carbon nanotubes (SWCNTs)

Low-dimensional materials gain increasing interest from the scientific community as well as from industry. The reduced dimensionality of nanomaterials leads to intriguing properties due to quantum confinement effects that promise to revolutionize fields from functional composites to electronic circuits. In particular, the low-dimensional carbon-based allotropes (Figure 2.1) spark interest for studying fundamental physics and enabling practical applications.[6, 7] The properties of the two-dimensional graphene, a single layer of graphite, are intriguing and led to the 2010 Nobel Prize in Physics being awarded to Andre Geim and Konstantin Novoselov. In graphene, all carbon atoms are sp^2 hybridized forming a honeycomb lattice. Graphene is generally known for its mechanical stability and electron conductivity, but exhibits many more fascinating properties.[8, 9] As will be shown in the following sections, the one-dimensional carbon nanotubes exhibit both similar properties, e.g. excellent electron transport, as well as different properties than graphene, for example, an electronic bandgap. Finally, yet importantly, zero-dimensional fullerenes are studied in a variety of application areas ranging from acceptor materials in solar cells[10] to drug delivery vehicles[11]. The research in this thesis focuses on studying the optoelectronic properties of SWCNTs and exploring their applications in light-

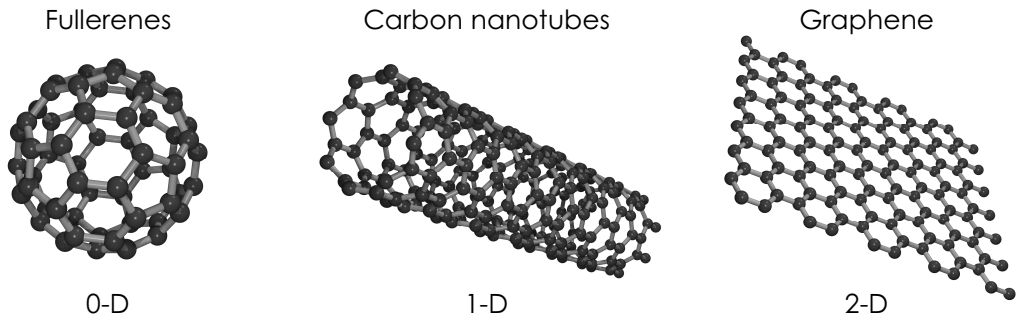

FIGURE 2.1. Carbon-based low-dimensional materials.
Molecular structures of low-dimensional carbon allotropes. From left to right, hollow carbon sphere (fullerene, 0-D), hollow carbon cylinders (single-walled carbon nanotube, 1-D), and monolayer of graphitic carbon (graphene, 2-D).

emitting devices. Therefore, the relevant characteristics of this low-dimensional carbon allotrope are presented in detail.

2.1.1 Structural properties

Single-walled carbon nanotubes (SWCNTs) are a carbon-allotrope in the form of a hollow cylinder. The wall of a carbon nanotube consists of hexagonal graphene lattice – triggering the vivid picture of SWCNTs as rolled-up graphene sheets. In this picture, there are innumerable ways to roll up graphene leading to a variety of different SWCNTs.[6, 12] Typical nanotube diameters range from less than one nanometer up to several nanometer while lengths of several µm up to mm can be observed.[13] The high aspect ratio (>1,000) results in the pronounced one-dimensionality that governs the exciting optoelectronic properties of SWCNTs. Perhaps surprisingly, both electronic and optical properties depend decisively on the exact tube diameter and rolling angle with respect to the graphene lattice.

Each SWCNT is completely described by the chiral vector

$$\boldsymbol{C}_\mathrm{h} = n\,\boldsymbol{a}_1 + m\,\boldsymbol{a}_2, \tag{2.1}$$

which denotes the vector around the circumference of the tube, and the tube vector $\boldsymbol{T}$ along the tube axis, describing the length $|\boldsymbol{T}|$ of the nanotube (Figure 2.2a). Here, $\boldsymbol{a}_1$ and $\boldsymbol{a}_2$ denote the graphene lattice vectors with length $a = \sqrt{3}a_{\text{C-C}}$ of 2.46 Å. The integer pair (n,m), which span the chiral vector, is termed chirality and used to uniquely distinguish different types of SWCNTs. Using the circumference of the nanotube[12]

$$C_\mathrm{h} = |\boldsymbol{C}_\mathrm{h}| = a\sqrt{n^2 + nm + m^2}, \tag{2.2}$$

the diameter can be calculated for each chirality (n,m)

$$d_\mathrm{t} = \frac{C_\mathrm{h}}{\pi} = \frac{a}{\pi}\sqrt{n^2 + nm + m^2}. \tag{2.3}$$

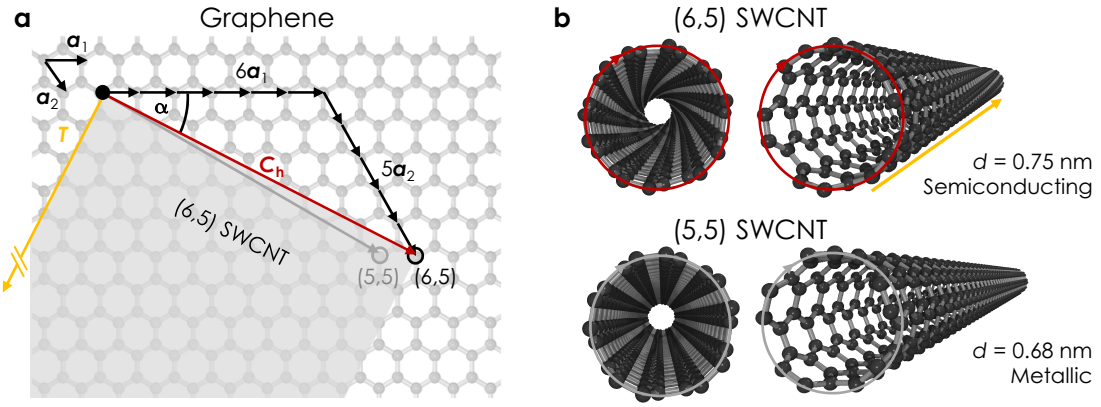

FIGURE 2.2. Structural properties of SWCNTs.
a, Molecular structure of the honeycomb graphene lattice (background). The chiral vector $\boldsymbol{C}_\mathrm{h} = 6\boldsymbol{a}_1 + 5\boldsymbol{a}_2$ (red) forms the circumference of (6,5) SWCNTs. The tube vector $\boldsymbol{T}$ (yellow) points in direction of the tube axis and defines the length of the nanotube. The chiral vector of (5,5) SWCNT is shown in gray. b, Molecular structure of (6,5) SWCNTs (top) and (5,5) SWCNTs (bottom). While they have similar diameter, their electronic type is fundamentally different (semiconducting vs. metallic).

Furthermore, the chiral angle α for the rolling direction with respect to $\boldsymbol{a}_1$ is given by

$$\cos(\alpha) = \frac{2n+m}{2\sqrt{n^2+nm+m^2}}. \tag{2.4}$$

This universal description of SWCNTs is exemplary illustrated in (Figure 2.2b) showing the atomic structure of a (6,5) and (5,5) SWCNT. While the diameter and chiral angle of these SWCNTs are almost identical (0.75 nm and 0.68 nm, 27° and 30° for (6,5) and (5,5) SWCNTs), the electronic structure is found to be fundamentally different – (6,5) SWCNTs are semiconducting whereas (5,5) SWCNTs are metallic. The reason for these elementary different electronic types among SWCNTs is elaborated in the following.

2.1.2 Electronic properties

In analogy to the molecular structure, the electronic structure of SWCNTs is derived from that of graphene. The electronic structure of graphene is governed by the delocalized π–electron system across the entire lattice.[14] This governs the materials' properties. As an example, these conjugated systems give rise to the ballistic charge transport in both graphene and SWCNTs.[15, 16] For the remainder of this section, only electrons (holes) within the π–orbitals are considered in the frame of the tight-binding model.[14]

Just like the structure in real space, the reciprocal lattice of graphene is a hexagonal lattice.[12] In this honeycomb lattice there are three main centers of symmetry denoted Γ-,

M- and K-point (Figure 2 3a). For SWCNTs, the periodic boundary condition along the nanotube-circumference results in a set of allowed wavevectors $\boldsymbol{k}$ that electrons can exhibit. This condition can be expressed as[12]

$$\exp\left[i\ (\boldsymbol{k}_\mathrm{a}+\boldsymbol{k}_\mathrm{c})\ (\boldsymbol{C}_\mathrm{h}+\boldsymbol{T})\right]=1. \tag{2.5}$$

with $\boldsymbol{k}_\mathrm{a}$ and $\boldsymbol{k}_\mathrm{c}$ being the reciprocal lattice vector along the tube axis and circumference, respectively. The condition along the circumference

$$|\boldsymbol{k}_\mathrm{c}|=j\ \frac{2\pi}{C_\mathrm{h}},\ \text{with}\ j=0,1,...,j_\mathrm{max}, \tag{2.6}$$

leads to discreetly spaced wavevectors in direction of $\boldsymbol{k}_\mathrm{c}$. In contrast, along the nanotube axis the allowed wavevectors are quasi-continuous for long SWCNTs, i.e. $|\boldsymbol{T}|\gg C_\mathrm{h}$. Hence, the allowed wavevectors for the free electron wavefunction in SWCNTs are a series of lines crossing the graphene band-structure, referred to as zone folding.[12] In Figure 2 3a the allowed wavevectors for (6,5) and (5,5) SWCNTs are plotted.[12] As will be shown in the following, if the K-point is crossed by such a line, the SWCNT is metallic; if the K-point is not crossed, it is semiconducting.

Following the idea of zone folding, the band structure of SWCNTs is composed of all cross-sections through the graphene band structure.[7, 12] In first approximation, the band structure $E(\boldsymbol{k})$ of graphene can be calculated using the nearest-neighbor tight binding model.[7, 12] The band structure of graphene shows characteristic cone-like structures with the valence and conduction band meeting at the K-points. This structure gives rise to the semi-metal character of graphene.[7, 12] By applying the boundary conditions for SWCNTs to the wavevector $\boldsymbol{k}$, all cross sections can be determined and added to derive the band structure of each chirality. Consequently, those SWCNTs that do not include a cross section with a K-point in their band structure exhibit a band gap and are thus semiconducting. Following Ref. [7], the band structure of (6,5) and (5,5) SWCNTs were calculated (Figure 2 3b). For (6,5) SWCNTs a direct bandgap is found, while (5,5) SWCNTs exhibit touching valence and conduction bands leading to its metallic character. In this model, a bandgap energy of 1.171 eV is calculated for (6,5) SWCNTs.

In order to understand the details of the electronic and optical properties of SWCNTs, the density of states (DOS), i.e. is the number of states, which can be occupied at a given energy, needs to be considered. Using an approximated linear and rotational-symmetric dispersion around the K-points, the analytic formula for the dispersion relation of a particular subband m is given by: (Ref. [7])

$$\frac{\partial E}{\partial k}=3\alpha\gamma\ \frac{\sqrt{E^2-{\epsilon_\mathrm{m}}^2}}{E}, \tag{2.7}$$

with m = 1,2,...,N, the interaction energy $\gamma=2.9$ eV (Ref. [6]) and $\epsilon_\mathrm{m}=|3(m-1)+1|\frac{a\gamma}{d_\mathrm{t}}$ for semiconducting and $\epsilon_\mathrm{m}=|3(m-1)|\frac{a\gamma}{d_\mathrm{t}}$ for metallic nanotubes. This leads to the simple expression for the DOS of SWCNTs

$$D(E)=\frac{2a\ \sqrt{3}}{\pi^2\ d_\mathrm{t}\ \gamma}\ \sum_\mathrm{m}\frac{|E|}{\sqrt{E^2-{\epsilon_\mathrm{m}}^2}}. \tag{2.8}$$

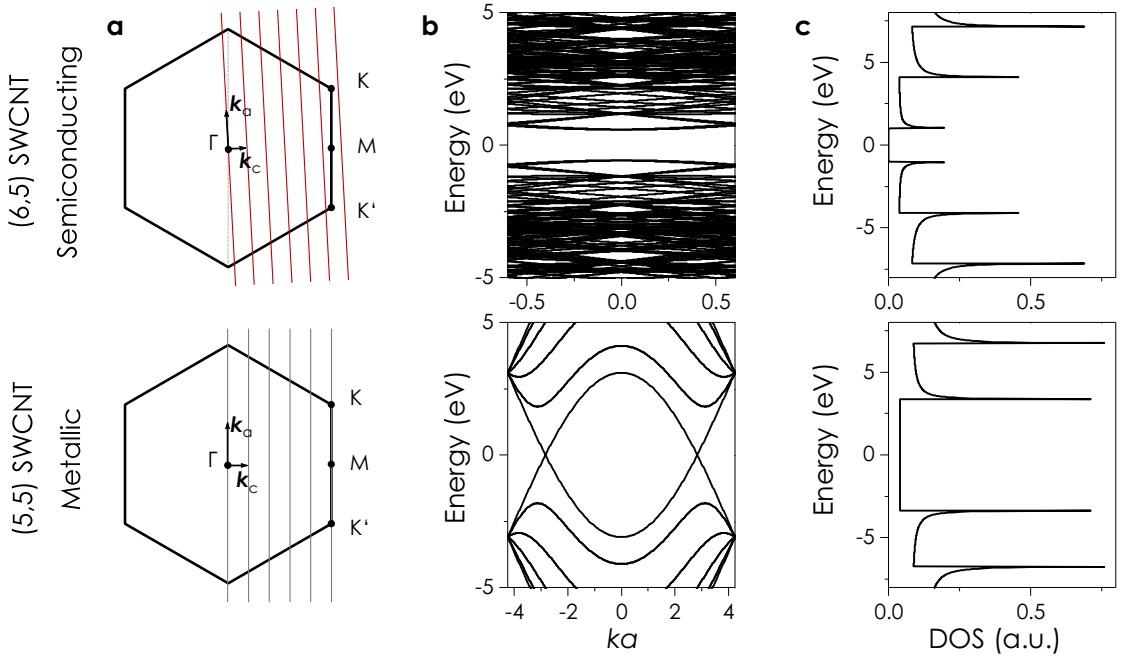

FIGURE 2.3. Electronic structure of SWCNTs.
Calculations are shown for (6,5) SWCNTs (top) and (5,5) SWCNTs (bottom). a, First Brillouin zone of graphene with high symmetry points of the hexagonal reciprocal lattice. The cutting lines represent the allowed wavevectors for the SWCNTs. In contrast to (5,5) SWCNTs, these cross-sections do not intersect with the K-points in case of (6,5) SWCNTs. b, Energy band structure calculated for both SWCNTs. A direct bandgap is formed in case of (6,5) SWCNTs. c, DOS for semiconducting (6,5) SWCNTs (DOS = 0 at 0 eV) and metallic (5,5) SWCNTs (DOS > 0 at 0 eV).

The DOS, calculated for (6,5) and (5,5) SWCNTs, is plotted in Figure 2 3c. Characteristic for a one-dimensional quantum system, van Hove singularities are found at $|E| = \epsilon_{\mathrm{m}}$ for electrons and holes. In addition, for (5,5) SWCNT the DOS is >0 for all energies indicating the metallic character. In contrast, for (6,5) SWCNTs, a bandgap opening between the first van Hove singularity of electrons and holes is observed. The absolute value of the bandgap energy (2.08 eV) clearly deviates from that calculated above using the tight binding model. Here, the simplification of linear and rotational-symmetric dispersion around the K-point,[7] does not include the trigonal warping which is found to be the dominant source of the deviation from the previous model.[17] Nevertheless, a rule-of-thumb relation between bandgap energy E_{g} and the tube diameter is found to be

$$E_{\mathrm{g}} = \frac{2a\,\gamma}{d_{\mathrm{t}}}. \tag{2.9}$$

In first approximation, the bandgap of semiconducting SWCNTs thus scales inversely with the tube diameter. In addition, the model predicts the Fermi level of SWCNTs to be in the center of

the bandgap, which is a result of the band structure of graphene.[7]

Experiments on individual SWCNTs confirmed the electronic structure introduced above, such as the electronic types, bandgap dependence on tube diameter and van Hove singularities in the DOS.[18] Hence, despite the approximation, for example neglecting the curvature effect in the nanotube wall, the presented model is a handy tool to describe the structural and electronic features of SWCNTs. In spectroscopic experiments, however, significant deviations from these models have been observed.[19] A more precise formalism – considering many-body effects – for describing the optical response of semiconducting SWCNTs is thus introduced in the next section.

2.1.3 Excitons in SWCNTs

In the previous section, the DOS of SWCNTs was derived using the tight-binding model to simulate the behavior of the delocalized electrons and holes. Further, the band structure of semiconducting SWCNTs revealed a direct bandgap. Thus, electrons can be optically excited into the conduction band, leaving a hole in the valence band. Optically allowed transitions are those between the i-th van Hove singularity in valence and conduction band and are associated with an energy E_{ii} (Figure 2.4a).[20] The bandgap energy is then given by the transition from the first van Hove singularity in the valence and conduction band E_{11}. In this picture, a direct bandgap of energy 1.171 eV was derived from the band structure for (6,5) SWCNTs. In contrast to these predictions, a significantly higher transition energy of 1.274 eV was found for (6,5) SWCNTs in experiments. Similar results were observed for more than 100 other chiralities.[21]

Precise description of the optical properties requires taking the low-dimensionality of SWCNT into account. The reduced dielectric screening, arising from the one-dimensional confinement of charges, leads to strong many-body interactions.[6] In sharp contrast to generating free-particles upon excitation, substantial Coulomb attraction results in the formation of bound electron-hole pairs, called excitons.[22]

Interestingly, these many-body interactions have two major components on shifting the transition energy (Figure 2.4b).[6] On the one hand, attractive electron-hole interaction leads to an exciton binding energy E_{b} – defined to be positive. This binding energy lowers the effective bandgap energy. At the same time, repulsion of the excited electron (hole) with the electrons (holes) in the valence (conduction) band, known as self-energy E_{self}, effectively increases the bandgap energy. Thus, the transition energy for the lowest optical excitation is described by:

$$S_{11} = E_{11} + E_{\mathrm{self}} - E_{\mathrm{b}}. \tag{2.10}$$

In case of SWCNTs, the self-energy is larger than the binding energy of the excitons, leading to an overall increase of the bandgap energy.[6, 22] Nevertheless, *ab initio* calculations predicted[22] and experimental work verified[23] a substantial exciton binding energy of several hundred meV for small diameter SWCNTs. In particular, the binding energy of excitons in (6,5) SWCNTs was found to be 285 meV. Hence, excitons in SWCNTs are stable at room temperature. Thus,

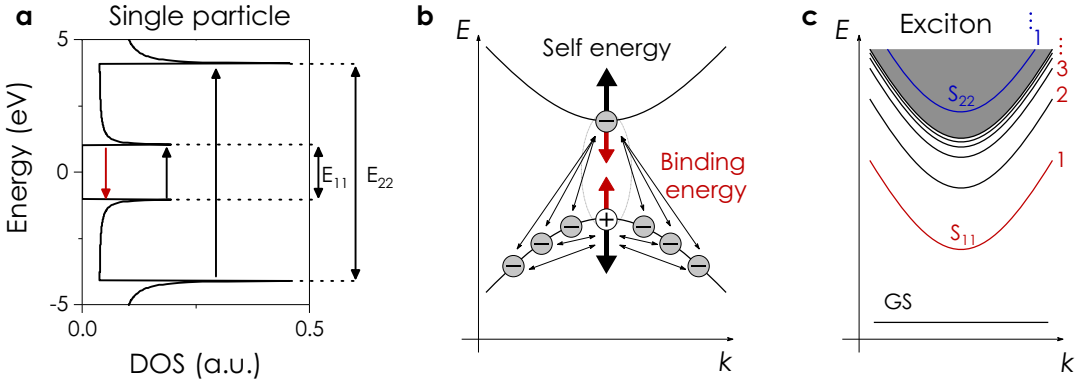

FIGURE 2.4. From single particle to exciton picture.
a, DOS of a semiconducting (6,5) SWCNT in the free-particle picture. Common optically allowed transitions, E_{11} and E_{22}, are labeled. b, Illustration of many-body effects due to Coulomb interactions for excitations in SWCNTs. Binding and self energy lead to an overall increase of the bandgap energy as compared to the free particle picture. c, Illustration of the excitonic states in SWCNTs for S_{11}- and S_{22}-exciton.

to describe the optical properties of SWCNTs, bound electron-hole pairs (excitons) must be considered. Figure 2.4c illustrates the excitonic transitions for the S_{11}- and S_{22}-exciton. Here, the excitons are considered as Hydrogen-like states with a corresponding Rydberg series for each excitonic transition.[24] A more precise description of excitons in SWCNTs is presented in the following.

The exact excitonic structure in SWCNTs is strongly governed by the band structure arising from graphene and the additional one-dimensional confinement. Generally, a two-fold valence and conduction band degeneracy arises from the symmetry of the zone-folding leading to four-fold degenerate optical transitions.[24] In analogy, an excitonic energy level is associated with four different excitons as the electron and hole can both be either in the K or K'-valley. These excitons (electron, hole) are described as (K,K), (K,K'), (K',K) and (K',K'). In real space the K and K' valley correspond to neighboring carbon atoms.[6] As the wavefunctions of the four combinations vary (and thus the many-body interaction), the degeneracy of these excitons is lifted.[25] Both excitons in which electron and hole are not in the same valley carry momentum. Thus they cannot be excited by a photon and are consequently called dark excitons.[25] The two excitons, (K,K) and (K',K'), have a bonding and anti-bonding wavefunction and are found at generally lower energy.[26] Both carry no momentum perpendicular to the tube axis. However, the even parity of the lower energy bonding (K,K) exciton results in an optically forbidden excitation.[24] Additionally, due to spin considerations, each excitonic state splits into one singlet and three triplet excitons with the latter being optically forbidden. All in all, 16 different excitons are formed, at each transition in the band structure, of which only one, the antibonding (K,K) singlet

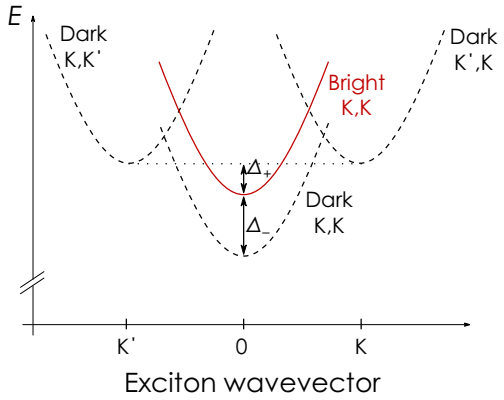

FIGURE 2.5. Excitonic structure in SWCNTs.
Schematic excitation energy dispersion of the S_{11}-exciton in SWCNTs. The differences in exciton wavevector and parity give rise to three different dark excitons and one bright exciton.

exciton, is an optically allowed transition.

The different excitons of the energetically lowest S_{11} transition are illustrated in Figure 2.5. In case of (6,5) SWCNTs, a characteristic energy splitting between the bright exciton and the energetically higher momentum-carrying dark excitons Δ_+ of ~25 meV was found[27] – in agreement with theoretical predictions[28]. Using the same model, the lower dark exciton in (6,5) SWCNTs was calculated to be about 55 meV below the bright exciton (Δ_-). The lower dark excitons are thus not accessible at room temperature since the thermal energy is not sufficient to enable efficient transitions to the bright exciton. Interestingly, these excitons can be brightened by symmetry breaking as observed in magnetic fields[28] or by introducing sp^3-defects in the SWCNT-lattice.[29] The triplet-singlet exchange energy (Δ_{ST}) of the bright exciton was found to be ~125 meV in (6,5) SWCNT.[30] Likewise, triplets are not thermally accessible. Brightening of these triplets can be achieved by enhancing the spin-orbit coupling, for example, by defects or molecular adsorption on the SWCNT-wall.[31] In first approximation, the exciton energy S_{11}, the energy splitting of the bright and dark momentum-exciton as well as low-energy dark exciton scale inversely with the nanotube diameter; the singlet-triplet exchange energy inversely to square of the diameter. In the remainder of this thesis, the bright excitons will be referred to as S_{ii}-excitons if not stated differently. These optically allowed transitions open the door to spectroscopically studying the fundamental properties of SWCNTs as well as to applications in optoelectronic devices.

2.1.4 Optical spectroscopy

As introduced in the previous section, strongly bound excitons are formed upon excitation in SWCNTs. Bright excitons can be optically excited, by the absorption of a photon. In experiments,

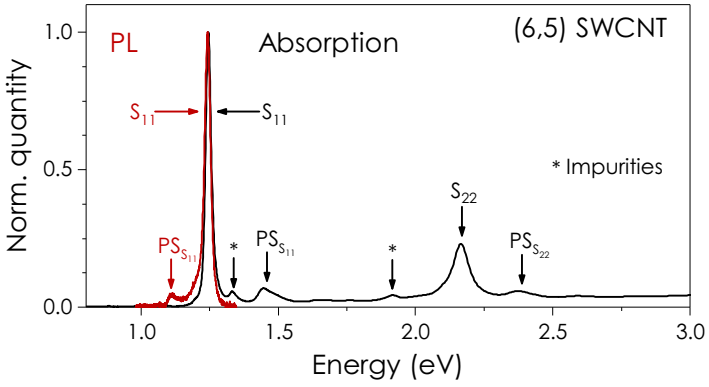

FIGURE 2.6. Absorption and PL of (6,5) SWCNTs.
Absorption and PL spectrum of (6,5) SWCNTs. A FWHM of the PL of 23.7 and 21.9 meV for absorption are observed. A minimal Stokes shift of 3.5 meV is present.

the exciton was found to be 13 nm in size along the (6,5) SWCNT.[32] Typically, in a excitonic transition 500 carbon atoms are involved which contribute to the overall S_{11}-exciton oscillator strength of ~5 (Ref. [33]). Similarly, the bright excitons can decay radiatively by emitting a photon. An experimentally measured absorption and emission spectrum of (6,5) SWCNTs in a polymer coating and dispersed in an organic solvent are shown in Figure 2.6. In absorption, two main peaks can be identified: the bright S_{11}- and S_{22}-excitons. Their energetic positions are in agreement with simulation in the framework of the exciton picture.[21] In this experimental data, the S_{11} absorption and emission peaks have a linewidth of 21.9 meV and 23.7 meV, respectively. Upon excitation of the S_{22}-exciton, emission is exclusively observed from radiatively decaying S_{11}-excitons. A Stokes shift, energetic shift of the PL with respect to the absorption of the S_{11}-exciton, of 3.5 meV is observed. In addition, all peaks show a pronounced phonon sideband (PS). The origin of these spectral characteristics and features are explored in the following.

In general, once generated excitons relax towards the lowest energetic state – in case of SWCNTs this is the S_{11}-exciton. This initial relaxation was found to be ultrafast (~40 fs from S_{22} to S_{11}) due to efficient coupling of excitons to lattice vibrations.[34] The S_{11}-exciton has a much longer lifetime which can vary between 10 and 100 ps depending on the environment, exciton diffusion and SWCNT quality as well as temperature.[26, 35] The S_{11}-exciton lifetime τ_X depends on radiative and non-radiative decay and is given by

$$\tau_X{}^{-1} = \tau_{rad}{}^{-1} + \tau_{nrad}{}^{-1}. \tag{2.11}$$

Here, τ_{rad} is the radiative lifetime, an intrinsic property of SWCNTs, and τ_{nrad} is the non-radiative lifetime. A radiative lifetime of ~5 ns (Ref. [36]) was experimentally verified for (6,5) SWCNTs corresponding to an homogenously broadened linewidth ($\hbar\tau_{rad}{}^{-1}$) of ~0.1 µeV. In addition to a very narrow linewidth, a small Stokes shift is expected to be present. The reason for this is the

very low molecular rearrangement between the ground and excited state in SWCNTs. These intrinsic properties were indeed observed for air-suspended pristine SWCNTs with reduced exciton diffusion and at low temperature.[35] Excitons in these SWCNTs exhibit lifetimes of few ns and extremely narrow linewidths on the order of µeV. Hence, non-radiative processes are strongly suppressed in this system. Starting from this ideal case, various parameters were identified to cause non-radiative decay and/or spectral broadening.

Most importantly, the inhomogeneities along the SWCNT were found to be a crucial parameter. These include defects in the carbon lattice and changes in the dielectric environment.[35, 37] As an example, for SWCNTs in contact with substrates and surfactants, spectral wandering was observed.[35, 38] This effect on inhomogeneous broadening is attributed to exciton diffusion along the nanotube leading to emission from parts of the SWCNTs that are in different dielectric environment. Exciton diffusion is highly enhanced in SWCNTs and typically up to 4 orders higher than in organic materials.[39] The exploration of the environment by diffusion of excitons and the resulting spectral fluctuations can be thought of as inhomogeneous broadening within a single SWNCT. A strongly reduced exciton lifetime for these SWCNTs also suggests non-radiative decay at quenching sites at the nanotube wall. In case of polymer-wrapped SWCNTs on a substrate, these effects can lead to typical exciton lifetime of ~30 ps and linewidths of few meV even at low temperature.[38]

Second, at room temperature, the linewidth of excitons in suspended SWCNTs increases to ~10 meV.[35] The thermal broadening is typically slightly lower than the thermal energy $k_{\mathrm{B}}T$ at room temperature.[40] A combination of environmental and temperature effects results in typical linewidths of >20 meV as observed above.

Other parameters can impact the exciton dynamics, for example, inter-tube interactions in high density samples,[26] dielectric screening,[41] length-dependent quenching at the ends of the nanotubes[39] and exciton annihilation processes[38]. All these processes strongly influence the emission efficiency. The probability of radiative recombination – also called PL quantum yield (PLQY) – is given by the ratio of the radiative decay rate ${\tau_{\mathrm{rad}}}^{-1}$ to the sum of all decay rates

$$\mathrm{PLQY} = \frac{{\tau_{\mathrm{rad}}}^{-1}}{{\tau_{\mathrm{rad}}}^{-1} + {\tau_{\mathrm{nrad}}}^{-1}}. \tag{2.12}$$

Knowing the intrinsic radiative lifetime, the impact of non-radiative processes and thus the quality of SWCNTs can be compared by measuring the PLQY.

In addition, phonon sidebands are observed for absorption and PL. These phonon sidebands are associated with optical brightening of the dark (K,K') excitons.[27] Momentum is conserved for these transitions since a phonon (vibrational D-mode) is involved in the absorption and emission process.

In summary, SWCNTs comprise unique optical behavior, e.g., a narrow linewidth, tunable nIR-emission, high photostability and a complex exciton fine structure. These properties make SWCNTs attractive nanomaterials for studying fundamental photophysics in one dimension

as well as for applications at single-photon light sources,[42, 43] telecommunications,[44] and bioimaging.[45] The experimental challenges in synthesizing in and separating different SWCNTs are discussed in the next section. These will focus on techniques suitable for optically emissive SWCNTs.

2.1.5 Synthesis and purification

As shown previously, the impact of minor structural variations on electrical and optical properties puts a high demand on the purity of SWCNTs for applications. Carbon nanotubes can be synthesized by various techniques, for example, laser ablation, arc discharge, plasma torch and chemical vapor deposition (CVD).[24] Generally, there are two strategies in synthesizing SWCNTs for optoelectronic devices. On the one hand, the nanotubes can be directly fabricated on the substrate by controlled growth form pre-patterned catalyst nanoparticles.[14] This approach has the advantage of avoiding any post-growth processing, as long as the nanotubes can be directly implemented on the same substrate. The downside is the missing electronic purity of the SWCNT, the high temperatures required limit the choice of substrate. Another approach is to generate a bulk amount of SWCNTs, e.g. as a powder, which are then processed and sorted to obtain, for example, nanotubes of different, but defined electronic nature. The main advantage is the high purity of semiconducting SWCNTs that can be achieved by appropriate post-growth processing as well as the solution processing of nanotube inks.[46–48] Here, the focus will be on the latter strategy with emphasis on the so-called CoMoCAT® (using cobalt molybdenum catalyst)[49] process in combination with post-growth selection by polymer wrapping as it was used throughout the work.

Despite strong efforts in tailoring the SWCNT-growth towards an exclusive chirality, i.e. monochiral growth,[50] state-of-the-art synthesis on an industrial scale still yields a mixture of semiconducting and metallic nanotubes.[51] Predominantly, CVD-based processes are used nowadays – owing to the narrow nanotube-diameter range that can be achieved.[52, 53] In particular, the CoMoCAT® process offers a narrow diameter distribution (0.7–0.9 nm), which can be optimized to yield dominant growth of (6,5) and (7,5) SWCNTs.[54] In this synthesis, a carbon source (carbon monoxide) is decomposed at metal, in this case a mixture of Co and Mo, at temperatures around 750 °C. The catalyst particle act as nucleation centers at which a carbon nanotube grow. Hence, the size and shape of the catalyst particle defines the diameter of the resulting SWCNT. Adjusting the synthesis conditions, for example, the temperature, the gaseous feed and the substrate, can be used to tailor the yielded chirality distribution. For the CoMoCAT® process these parameters have been optimized to reliably produce macroscopic amounts (few grams) of SWCNTs.[49]

The resulting mixture of SWCNTs require post-growth selection techniques to purify and sort the material by electronic grade and ultimately by single chiralities. Here, the focus will be on how semiconducting species can be extracted on a monochiral level. In general, all approaches

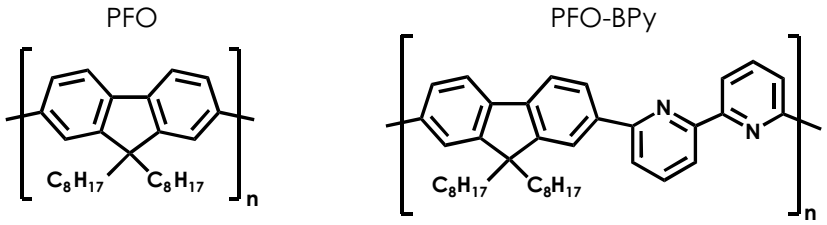

FIGURE 2.7. Molecular structure of PFO and PFO-BPy.

first disperse the SWCNT source material and then selectively solubilize the separated SWCNTs by, e.g., a surfactant or conjugated polymer.[47, 55–57]

Aqueous dispersions of SWCNTs can be obtained by using surfactants, such as sodium dodecyl sulphate (SDS) or sodium cholate, having a hydrophobic part pointing to the nanotube and hydrophilic part away from the nanotube.[58] This method creates an non-selective dispersion of all SWCNTs present in the sample. Selectivity towards electronic type and single chiralities can be achieved by, for example, gel chromatography[55], aqueous two-phase separation[59] or repetitive density gradient ultracentrifugation (DGU).[60] Here, DGU is described in more detailed as it is used throughout this thesis for benchmarking monochiral SWCNT dispersions prepared by polymer wrapping. In this method, due to differences in buoyant density of the nanotube with its surfactant shell, each chirality can separated in the density medium.[61] Thus, it is a universal approach and can be applied to different SWCNT sources and optimized for any chirality. As a result of the unselective dispersion, however, cross-contamination between semiconducting species and a remaining metallic content in these samples cannot be completely avoided.[62] Consequently, the PLQY of these samples is typically limited to well below 1% owing to remaining SWCNT-bundles and the metallic content.[62] In addition, this method is limited by the throughput of the DGU and is not easily scalable as it requires overnight centrifugation at >250,000g. It should further be noted that a density gradient medium (typically sugars such as Iodixanol or sucrose) is required at high concentration (10-20 wt%) to achieve the separation in the density gradient. Removal of the sugar (for example by extensive dialysis) as an additional processing step is often required, in particular for device applications.

More recently, it became clear that polymer-wrapping is a highly selective, high-throughput purification method for semiconducting SWCNTs.[63, 64] Depending on the combination of SWCNT and π-conjugated polymer (backbone and side-groups) structure, the polymer can wrap selectively around certain nanotube species forming densely packed supramolecular arrangements. If this is the case, this SWCNT chirality is preferentially "solubilized" (i.e. dispersed). If this is not the case, the polymer can still be adsorbed in an unordered aggregated way resulting in only weakly solubilized aggregates. These can be conveniently removed by centrifugation with relatively short and slow centrifugation thus leading to highly enriched supernatants. Among the many polymers identified for this purpose,[65] the polyfluorene (poly(9,9-dioctylfluorene), PFO)

and its copolymers exhibit the highest selectivity.[64] In these systems, π-π stacking of the backbone of the polymer along the SWCNT wall was found to be the dominant binding process.[64] The actual wrapping is found to be in helices around the SWCNT.[66] Interestingly, polymer wrapping can lead to almost monochiral dispersions. For example, PFO and PFO-BPy (Figure 2.7) as dispersants for CoMoCAT® material were found to be highly selective toward single chirality (7,5) and (6,5) SWCNTs, respectively.[47, 64] The selectivity and yield not only depend on the type of polymer but also on solvent[64] and molecular weight of the chains[67]. While the yield of the dispersion is increased for solvents with high viscosity and high molecular weight of the polymer, the selectivity is generally reduced. Interestingly, the polymer-wrapped SWCNT show good separation and much higher PLQY than surfactant based dispersion potentially due to efficient shielding form the environment. In ensemble measurements, typical PLQY range from 0.5 to 1.5% depending on the processing steps.[39, 64, 68] Optoelectronic applications will directly gain in performance by using the higher grade of SWCNT quality.

2.2 Devices for light generation

The following section reviews light-emitting devices based on organic materials. The emergence of organic electronics led to a tremendous development of devices and methodologies to generate light using carbon-based emitters. Primarily, two device architectures have been explored: organic light-emitting diodes (OLEDs, Figure 2.8a) and light-emitting field-effect transistors (LEFETs, Figure 2.8b). In both cases, a multilayer stack of materials is employed to efficiently inject and transport charge-carriers to generate light in the emissive material. One of the main differences between the two devices arises from the control of the injected charges. In contrast to the direct forward bias driving LEDs, an electric field generated by an additional electrode (gate) is used in FETs to control the charge injection and transport. Furthermore, as illustrated in Figure 2.8, the current flows perpendicular (parallel) to the top electrode in OLEDs (LEFETs). Consequently, the emission area is defined by the overlap of anode and cathode in case of OLEDs, whereas in LEFETs an emission line parallel to the source/drain electrodes is observed. The working principle and the device characteristics of both device types are introduced in the following.

2.2.1 Organic light-emitting diodes (OLED)

In 1965, W. Helfrich and W.G. Schneider reported on the first OLED using an anthracene crystal sandwiched between two electrodes.[69] In the experiments, electroluminescence was observed in the emission layer (EML) by applying more than 1,000 V to the 5 mm thick crystal. The crystal was directly contacted by an electron-injection electrode (cathode) and a hole-injection electrode (anode). Since then the development of new fabrication techniques as well as development of materials has led to more efficient and complex devices operating at low voltages.[70–72] Nowadays, OLEDs comprise a stack of thin layers (few nanometers to hundreds of nanometers).[73, 74] By

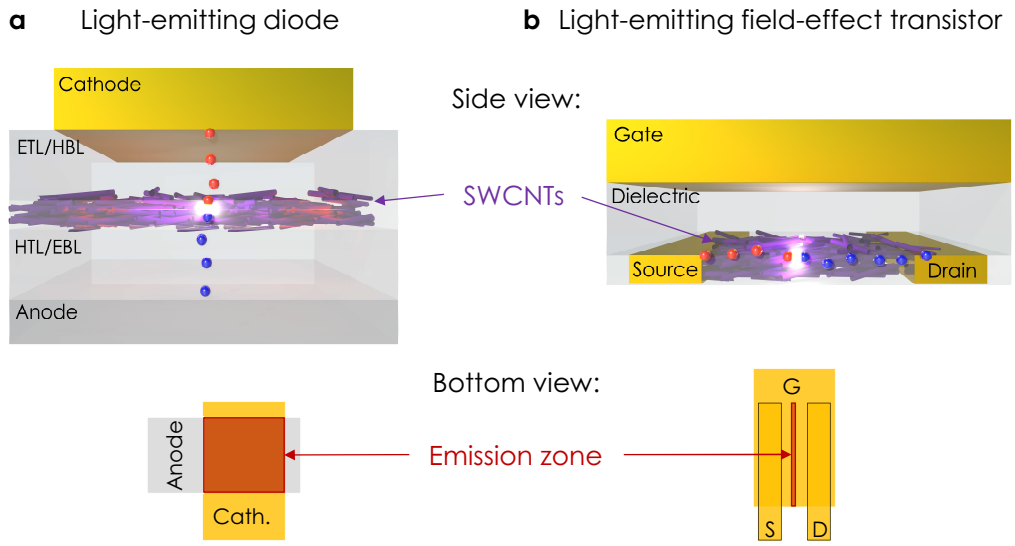

FIGURE 2.8. Illustration of devices for electrical generation of light.
a, OLED and b, LEFET schematics from side view (top) and bottom view (bottom). Electrons (red) and holes (blue) are injected and transported perpendicular to the cathode in case of OLEDs and parallel in LEFETs.

applying a forward bias, electrons and holes are injected into the stack and transported through multiple layers toward the EML. The injected charges form excitons in the EML, which in turn can decay radiatively. The emitted light is then outcoupled by using one or two transparent electrodes. In case of bottom-emitting OLEDs, a transparent bottom electrode on the substrate (here, anode) and a reflective top electrode (here, cathode) are used. The emission zone in an OLED is defined by the overlapping area of the electrodes. Hence, large-area homogeneous light emission can be achieved.[75]

Figure 2.9a depicts the energy levels of a pin-type OLED under forward bias. In this device p-(n-)doped layers are employed for efficient charge carrier injection and enhanced hole (electron) transport.[71, 74, 76] These layers are thus called hole and electron transport layers (HTL and ETL). Band bending at the interfaces of the doped transport layers to the electrodes enables the efficient injection of charges leading to almost Ohmic contacts.[76] For efficient electroluminescence, electron (hole) blocking layers are added between the transport layers and the EML.[76] The EBL and HBL prevent quenching at the interfaces to the doped layers and block the electrons and holes from passing through the EML. Often the emitter molecules are embedded in a host material with larger bandgap to prevent concentration quenching at the emitter molecules.[77]

Optimized OLEDs exhibit diode-like current-voltage characteristics. Generally, the current I can be described by the diode equation[78]

$$I = I_0 \left[\exp\left(\frac{q\,V}{n\,k_\mathrm{B}\,T} \right) - 1 \right]. \tag{2.13}$$

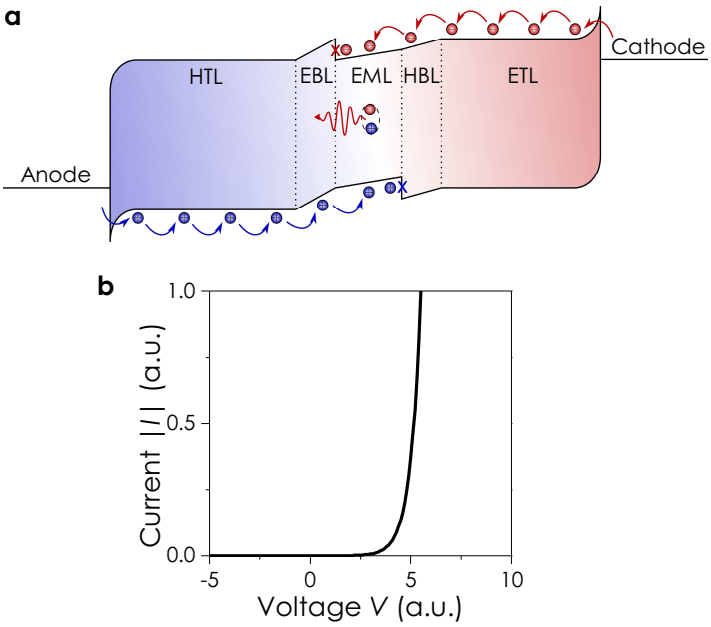

FIGURE 2.9. Energy diagram of an advanced OLED stack.
Highly efficient OLEDs comprise a pin-type structure. Doped injection layers and charge transport layer are used (ETL and HTL). Additional blocking layers (EBL and HBL) prevent charge diffusion and capture charge recombination in the EML.

Here, I_0 is the saturation current, q the elemental charge, V the applied voltage across the OLED, n the ideality factor, k_B the Boltzmann constant and T the temperature. This relation describes the Schottky diode behavior as well as the pn-junction in OLEDs.[78] Figure 2.9b shows the typical I-V characteristics for an OLED in forward (>0 V) and backward (<0 V) operation. Electroluminescence is typically only observed in forward direction and above a device-specific threshold voltage.[79]

2.2.2 Light-emitting field-effect transistor (LEFET)

In contrast to OLEDs, in LEFETs charge carriers are transported in the plane of the EML. A schematic device architecture of a top-gate/bottom emission LEFET is depicted in Figure 2.10a. In a LEFET, the charge-carrier accumulation and transport can be controlled by the applied gate voltage V_g. The gate electrode is electrically separated from the conductive channel by an insulating material (dielectric). The applied potential leads to charge carrier accumulation at the dielectric/semiconductor interface. By applying an additional bias between source and drain V_d, these charges can be transported through the semiconductor material in the channel region.[80] In case of LEFETs, both electrons and holes can be injected and accumulated simultaneously under appropriate biases (ambipolar regime). In this regime, excitons are formed within the channel (recombination zone) that lead to light emission from the LEFET.[81–83]

In the following, the electrical behavior of a LEFET, with position x in the channel of length L, is derived (Figure 2.10a). The main characteristics of FETs can be described in the gradual channel approximation which assumes linearly varying field $V(x)$ in the channel:[80]

$$\frac{Q\ \partial V(x)}{\partial x} = \frac{V_\mathrm{d}}{L}. \tag{2.14}$$

Considering only electron injection, the aerial charge carrier density Q as a function of position in the channel is given by

$$Q(x) = C\ (V_\mathrm{g} - V_{\mathrm{th,e^-}} - V(x)). \tag{2.15}$$

Here, the threshold voltage for electron injection $V_{\mathrm{th,e^-}}$ is introduced. The current flowing between source and drain I_d is given by

$$I_\mathrm{d} = W\ \mu_{\mathrm{e^-}}\ Q\ \frac{\mathrm{d}V}{\mathrm{d}x}, \tag{2.16}$$

with W being the width of the channel and $\mu_{\mathrm{e^-}}$ the charge carrier mobility of electrons in the semiconductor. Thus, the average current flowing in the channel is given by

$$I_\mathrm{d} = W\mu_{\mathrm{e^-}}\ \frac{\int_0^\mathrm{L}\ C\ (V_\mathrm{g} - V_{\mathrm{th,e^-}} - V(x))\ \mathrm{d}x}{L}\ V_\mathrm{d}. \tag{2.17}$$

It turns out that the current is solely determined by the applied gate and drain voltages. In the case of $V_\mathrm{g} - V_\mathrm{d} > V_{\mathrm{th,e^-}}$, electrons are accumulated in the entire channel and the source-drain current can be derived as

$$I_{\mathrm{d,lin}} = \frac{WC}{L}\ \mu_{\mathrm{e^-}}\ \left((V_\mathrm{g} - V_{\mathrm{th,e^-}})\ V_\mathrm{d} - \frac{{V_\mathrm{d}}^2}{2}\right). \tag{2.18}$$

Since for small drain bias, the current depends linearly on V_d, this regime is called the linear regime.[84] For biases of $V_\mathrm{g} - V_\mathrm{d} < V_{\mathrm{th,e^-}}$ and $V_\mathrm{g} > V_{\mathrm{th,e^-}}$, a pinch-off of accumulated electrons occurs within the channel at the position for which $V_\mathrm{g} - V(x) = V_{\mathrm{th,e^-}}$ is fullfilled.[80, 84] In this regime, called the saturation regime, the source-drain current is given by

$$I_{\mathrm{d,sat}} = \frac{W}{2L}\mu_{\mathrm{e^-}}C(V_\mathrm{g} - V_{\mathrm{th,e^-}})^2. \tag{2.19}$$

So far, only electron injection was considered. In an ambipolar semiconductor, however, both electrons and holes can be injected simultaneously.[81, 84] Holes will be injected if $V_\mathrm{g} - V_\mathrm{d} < V_{\mathrm{th,h^+}}$ and $V_\mathrm{g} - V_\mathrm{d} < V_{\mathrm{th,e^-}}$ are fulfilled – a regime called the ambipolar regime. The source-drain current then consists of a contribution from electrons and holes in the channel. By assuming balanced electron and hole current, i.e. $I_{\mathrm{th,e^-}} = I_{\mathrm{th,h^+}} = I_\mathrm{d}$, the current in the saturation regime is then given by

$$I_{\mathrm{d,amb}} = \frac{W}{2L}\mu_{\mathrm{e^-}}C(V_\mathrm{g} - V_{\mathrm{th,e^-}})^2 + \frac{W}{2L}\mu_{\mathrm{h^+}}C(V_\mathrm{g} - V_\mathrm{d} - V_{\mathrm{th,h^+}})^2. \tag{2.20}$$

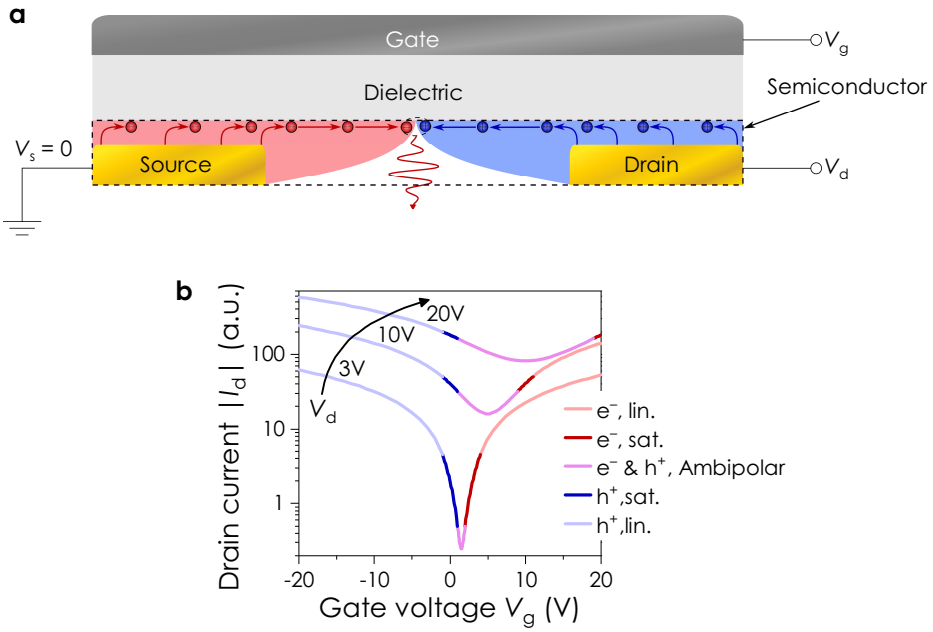

FIGURE 2.10. LEFET device in the true ambipolar regime.
Illustration of a LEFET device architecture and charge concentration along the channel. Parameters: $V_{th,e^-} = V_{th,h^+} = 1$, $\mu_{th,e^-} = \mu_{th,h^+}$.

In analogy to the linear and saturation regime for electron transport, these regimes exist as well for pure hole transport.

As an example, the transfer-characteristics (I_d vs. V_g) are plotted in Figure 2.10b for varying V_d. For these calculations, a threshold voltage of +1V (-1V) for electrons (holes) and an identical charge carrier mobility for electrons and holes was used. The calculated transfer-curves show the typical V-shaped transfer curve for ambipolar transistors. It can be seen that the absolute current in the true ambipolar regime is increased for higher drain biases. In case of LEFETs, the higher current correspond to an increased exciton-pumping rate in the device. In addition, charge carrier mobilities can be extracted from the transistor characteristics.[85]

In the presence of high drain bias and charge recombination in the channel, the gradual channel approximation does not precisely describe the potential within the device.[86] Instead a steep potential drop at the pinch-off points is observed. This leads to the shape of the charge carrier accumulation as depicted schematically in Figure 2.10a. The general considerations and trends derived with the presented gradual channel approximation still provide a good approximation. From the model, demands on material and LEFET structure can be deduced for generating maximum amount of light. First, it is desirable to have low thresholds for both charge-carrier injections. Second, high charge-carrier mobilities of both electrons and holes are desirable to achieve high currents in the transistors.

2.2.3 External quantum efficiency

An important measure to compare different light-emitting devices is the external quantum efficiency (EQE). The EQE, ultimately, describes the number of generated outcoupled photons per injected charges.[87] The EQE can be split into four different components describing separate processes within the device:[87, 88] First, the charge carrier balance, η_{balance}, accounts for a possible imbalance of electrons and holes injected into the EML. An excess of one type of charge will lead to quenching and thus reduce the charge-carrier balance. Second, electrical generation of excitons leads to a randomized spin of injected electrons and holes and thus singlet and triplet excitons are generated. Due to spin statistics, 75% of the excitons are triplets and 25% singlets. The spin-factor η_{spin} accounts for the material-specific ratio of how many of these excitons can decay radiatively during their lifetime. In fluorescent materials, all triplets will decay non-radiatively and the spin-factor is 0.25 reducing the overall efficiency.[73] Third, the emission efficiency η_{rad} of the material must be taken into account. This factor accounts for how many of the bright excitons will decay radiatively and is often equal to the PL quantum yield (PLQY).[89] Last, outcoupling of the generated light is an additional loss channel. Typical organic material have a refractive index of ~1.7 leading to total internal reflection at the interfaces towards the surrounding air.[90] Therefore, the outcoupling efficiency η_{out} accounts for optical losses in the multilayer stack. Hence, the overall EQE of light-emitting devices is described by

$$\text{EQE} = \eta_{\text{balance}}\,\eta_{\text{rad}}\,\eta_{\text{spin}}\,\eta_{\text{out}}. \tag{2.21}$$

The efficiency of light generation, called the internal quantum efficiency, comprises the charge-carrier balance, spin factor and the radiative efficiency. In state-of-the-art OLEDs, the internal efficiency can readily be close to unity. As described above, the advanced multilayer stack including doped transport layers ensure balanced charge carriers in the EML.[76, 88] Typically, efficient phosphorescent or thermally activated delayed fluorescence (TADF) emitters are used that ensure light generation at 100% efficeincy.[72, 88] For LEFETs, the charge-carrier balance is inherently obtained during operation in the ambipolar regime. The maximum internal quantum efficiency of ~30% was observed within LEFETs – mainly limited by the availability of efficient emitter materials that show ambipolar charge transport.[91] LEFETs, however, maintain these efficiencies even at very high current densities, which are typically multiple orders above those observed in OLEDs.

The outcoupling efficiency, in a standard device, is limited to ~25% for both OLEDs and LEFETs.[87, 91] The main loss channels are coupling of the generated light to substrate modes, wave-guided modes in the organic materials and coupling to lossy surface plasmons. Several approaches have been proposed and experimentally demonstrated to enhance the outcoupling form the device.[87, 90, 92, 93] Most methods, however, come along with significant complications in the device manufacturing and/or increased manufacturing costs. A promising alternative to these methods is the orientation of the emissive dipole moments parallel to the sample

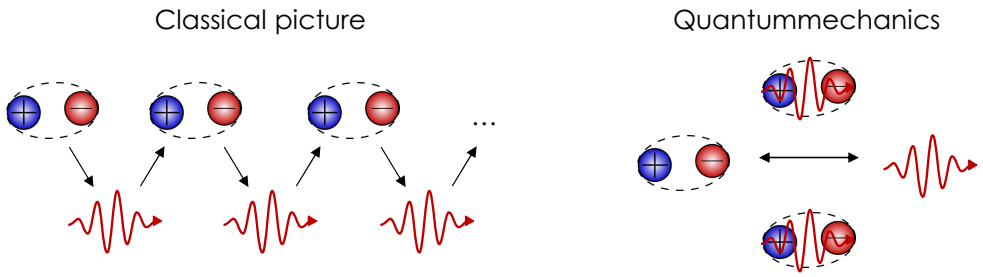

FIGURE 2.11. Light-matter interaction in classical and quantum-mechanical picture. Illustration of exciton-photon hybridization in the classical picture (left). Repetitive reabsorption of emitted photons leads to an energy exchange. In the quantum-mechanical picture (right), hybrid particles are formed which have a probability to be a photon and exciton simultaneously.

surface.[79, 93] Horizontally aligned emissive dipoles favor outcoupling by directed emission within the EML.

2.3 Cavity exciton-polaritons

Implicitly, the previous introduction to light-emitting devices is based on excitons that are weakly coupled to the surrounding optical fields. Hence, the transition probability is governed by Fermi's golden rule.[94] In multi-layer stacks, it was further shown that the device architecture leads to a cavity effect altering the emission spectrum and efficiency of the free emitter by the presence of the electromagnetic field. These effects can be readily explained with preferred emission into the increasing density of states in the final state, called the Purcell effect.[95] In the previous case, the energy landscape and transition energies are fundamentally identical – a regime associated with weak light-matter interaction owing to the low cavity quality (only one reflective electrode).

By using a second reflective mirror/electrode, optical cavities can be formed that support multiple back-reflection of the photons inside the cavity. If these cavities are tuned to overlap with the absorption of the excitonic emitter itself, strong exciton-photon interaction can lead to hybrid light-matter states. In a classical picture, this effect can be explained by repetitive reabsorption of the photons by the excitonic material and reemission leading to an energy exchange (Figure 2.11, left). Strong light-matter coupling is reached if the exchange between the light (photons) and matter (excitons) is faster than their dissipation. In the strong coupling regime, it is no longer valid to treat the system as a series of excitation and emission nor as a superposition of excitons and photons (Figure 2.11, right).[96] Instead, hybrid light-matter particles are formed – so-called exciton-polaritons. Interestingly, these quasiparticles combine properties of photons, for instance the low mass, with those of excitons, for example nonlinear interactions.[97, 98] The dynamic and emissive behavior of exciton-polaritons is governed by their hybrid character as will be described

in the following.

A comprehensive overview and review of the field of strong light-matter coupling in organic materials was published by the author of this thesis *et al.* in chapter nine of the *Handbook of Organic Materials for Electronic and Photonic Devices* (Ref. [5]).

2.3.1 Planar cavities

Photonic cavities can have various shapes and forms.[99–101] Here, planar Fabry-Pérot microcavities are considered (called cavities in the following). In such a cavity, a flat layer of refractive index n and thickness d is sandwiched between two planar reflective mirrors (Figure 2.12a). Light inside the cavity is reflected between the two mirrors leading to interference of the incident and reflected waves. Waves, which replicate during one roundtrip, will constructively interfere and experience an enhanced electric field inside the cavity. The wavevector k of a wave is described by a linear combination of its component parallel $k_{\parallel}$ and perpendicular $k_{\perp}$ to the surface. Thus, the first order cavity resonance is present if

$$k_{\perp}^{\mathrm{res}} = \frac{\pi}{d}. \tag{2.22}$$

Note, also multiples of $k_{\perp}^{\mathrm{res}}$ fulfill the standing wave condition but are not further considered. The dispersion of the cavity resonance can thus be expressed by

$$E_{\mathrm{C}}(k) = \frac{\hbar c}{n} k = \frac{\hbar c}{n}\left[\left(\frac{\pi}{d}\right)^2 + {k_{\parallel}}^2\right]^{0.5}. \tag{2.23}$$

Using $k_{\parallel} = E_{\mathrm{C}} \sin(\theta)/\hbar c$, leads to an expression of the cavity resonance as a function of viewing angle θ with respect to the normal of the cavity

$$E_{\mathrm{C}}(\theta) = E_0\left[1 - \left(\frac{\sin(\theta)}{n_{\mathrm{eff}}}\right)^2\right]^{-0.5}. \tag{2.24}$$

Here, the effective refractive index n_{eff} and the resonant energy at $\theta = 0°$, E_0 , was introduced. The effective refractive index might account for any penetration of the fields into the mirrors and for varying refractive indices within multilayer stacks inside the cavity.

If light of energy $E_{\mathrm{C}}(\theta)$ is incident on a cavity under an angle θ will be effectively trapped inside the cavity. Transfer-matrix simulations of the reflectivity of a planar metal-clad microcavity ($n = 1.5$ and $d = 210\,\mathrm{nm}$) is shown in Figure 2.12b. The typical parabolic cavity mode is observed as a minimum in reflectivity. By decreasing the thickness of the layer to 200 nm (Figure 2.12c), the cavity mode is shifted towards higher energy. At the same time, the parabolic shape of the dispersion is almost identical due to the same refractive index. In a Fabry-Pérot resonator, the cavity resonance can hence be easily tuned by adjusting the mirror spacing.

Due to the finite reflectivity of mirrors, photons inside the cavity will eventually leak out one of the mirrors. The lifetime of the photons inside the cavity τ_{C} is directly linked to the FWHM of the cavity resonance ΔE by[102]

$$\tau_{\mathrm{C}}\, \Delta E = \hbar. \tag{2.25}$$

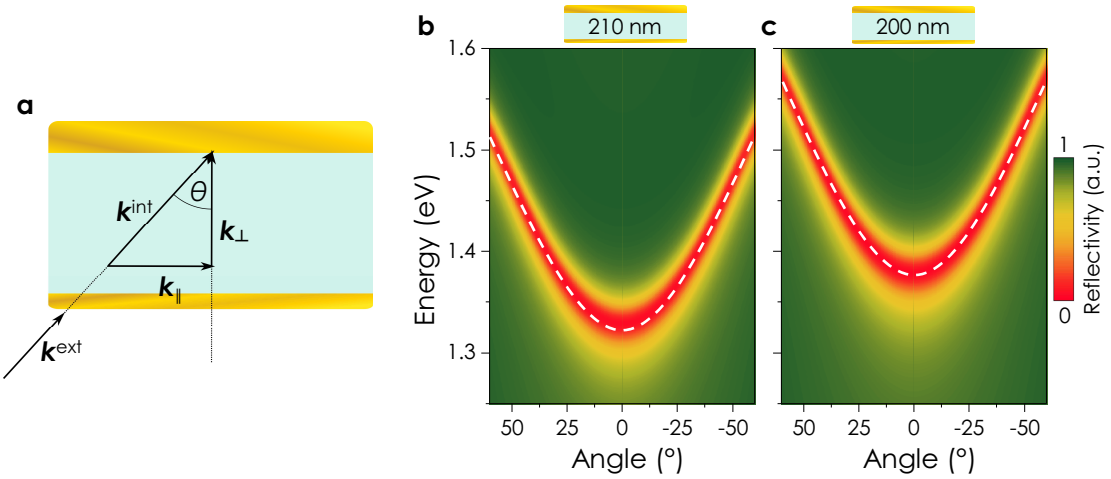

FIGURE 2.12. Planar optical cavities.
a, Schematic structure of a planar optical microcavity. The wavevector k is described by its perpendicular and parallel component. The viewing angle θ with respect to the normal of the cavity is used during angle-resolved characterization. b and c, Angle-resolved reflectivity spectra for a 210 and 200 nm thick cavity.

In case of the cavity depicted in Figure 2.12b, a FWHM of 48 meV and thus a photon lifetime of 14 fs is present. In general, for two identical mirrors with reflectivity R and neglecting any optical losses inside the cavity, the photon lifetime is given by

$$\tau_C = -\frac{d\ n}{c\ \ln(R)}. \tag{2.26}$$

It follows that, in order to increase the photon lifetime, highly reflective mirrors must be used. For universal comparison, cavities are characterized by their dimensionless quality factor, which is defined as[102]

$$Q = \frac{E}{\Delta E} = \frac{\tau_C\, E}{\hbar}. \tag{2.27}$$

For high-reflectivity dielectric mirrors, quality factors of >1,000 can be readily achieved.[101] The metal-clad cavity, presented in Figure 2.12b, has quality factor of 28 representing the short photon lifetime inside the cavity. Nevertheless, metal mirrors are often used for fundamental investigation due to the ease of fabrication and broad-band reflectivity.[103, 104] Even inside the investigated metal-clad cavity, photons pass on average seven times through the cavity during their lifetime before leaking out.

2.3.2 Strong light-matter coupling

As briefly described above, light-matter interaction results from repetitive reabsorption of the emitted light. Thus, a material with sufficient excitonic absorption at energy E_X close to photon

mode $E_C(\theta)$ must be placed inside the microcavity to enhance interactions. Note, owing to their comparatively larger mass, the dispersion of the exciton is much lower and thus neglected in the following.[105] This approximation is valid for excitons in SWCNTs as their mass is orders higher than those of photons.[106, 107] To describe light-matter coupling, the coupled oscillator model is introduced. In this model, the interaction between excitons $|X\rangle = \binom{1}{0}$ and the photons $|C\rangle = \binom{0}{1}$ is described by the coupling potential V_A. The system can be fully characterized by introducing the Hamiltonian, $\mathscr{H}$, which is given by:[96, 108]

$$\mathscr{H} = \begin{bmatrix} E_X - i\hbar\Gamma_X/2 & V_A \\ V_A & E_C(\theta) - i\hbar\Gamma_C/2 \end{bmatrix}. \tag{2.28}$$

Here, Γ_X (Γ_C) is the homogeneous decay rates of the exciton (photon) given by the inverse of their lifetime ${\tau_X}^{-1}$ (${\tau_C}^{-1}$). The new eigenstates E are described by

$$\begin{bmatrix} E_X - i\hbar\Gamma_X/2 & V_A \\ V_A & E_C(\theta) - i\hbar\Gamma_C/2 \end{bmatrix} \begin{bmatrix} \alpha \\ \beta \end{bmatrix} = E \begin{bmatrix} \alpha \\ \beta \end{bmatrix}. \tag{2.29}$$

The variables α (β) denote the Hopefield coefficients and are related to the exciton (photon) components of the new eigenmodes. Note, the losses of the oscillators are included in the imaginary parts of the respective matrix elements since in a time-dependent wavefunction $|\Psi(t)\rangle$ of the form

$$|\Psi(t)\rangle = e^{-iEt/\hbar} |\Psi(0)\rangle \tag{2.30}$$

imaginary terms account for the damping of the modes.[96]

By diagonalizing the Hamiltonian, the eigenvalues of the coupled system, called upper polariton (UP) and lower polariton (LP), are derived:

$$E_{UP/LP}(\theta) = 0.5(E_X + E_C(\theta) - i\hbar\Gamma_X/2 - i\hbar\Gamma_C/2) \pm \sqrt{{V_A}^2 + 0.25(E_X - E_C(\theta) - i\hbar\Gamma_X/2 + i\hbar\Gamma_C/2)^2}. \tag{2.31}$$

The new eigenstates $|UP\rangle$ and $|LP\rangle$ are given by the linear combination of exciton and photon

$$|UP\rangle = \alpha_{UP}|C\rangle + \beta_{UP}|X\rangle \quad \text{and} \quad |LP\rangle = \alpha_{LP}|C\rangle + \beta_{LP}|X\rangle. \tag{2.32}$$

The photon and exciton fraction of the polariton mode, $|\alpha|^2$ and $|\beta|^2$, are given by the projection of the corresponding polariton state onto the uncoupled (exciton or photon) state.[96] The photonic fraction is thus given by

$$|\alpha_{UP/LP}(\theta)|^2 = \frac{{V_A}^2}{{V_A}^2 + \left(E_{UP/LP}(\theta) - E_C(\theta)\right)^2}, \tag{2.33}$$

and excitonic fraction by

$$|\beta_{UP/LP}(\theta)|^2 = \frac{{V_A}^2}{{V_A}^2 + \left(E_{UP/LP}(\theta) - E_X(\theta)\right)^2}. \tag{2.34}$$

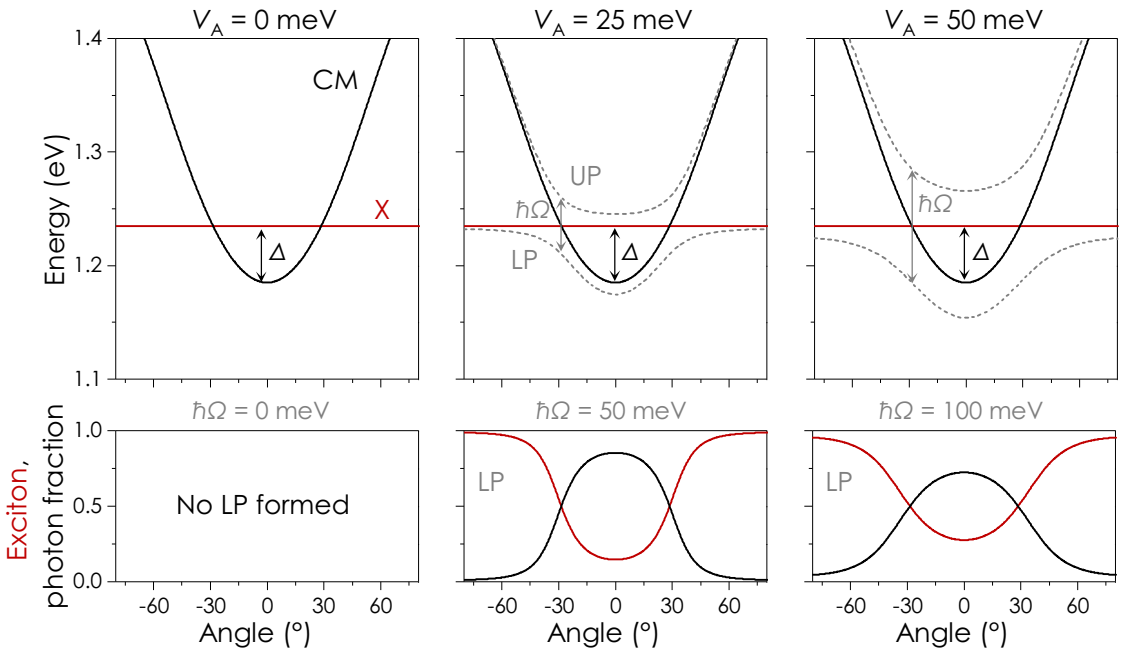

FIGURE 2.13. Coupled oscillator model for varying coupling strength.
From left to right, the dispersion the UP and LP (top) and the exciton and photon fraction (bottom) as calculated with the coupled oscillator model for increasing coupling strength.

As these fractions are a function of the viewing angle, the particular mixing of the exciton and photons thus depend on the direction of the wavevector.

A representative polariton dispersion depending on the coupling strength V_A is plotted in Figure 2.13. While in the absence of coupling the uncoupled exciton and photon dispersion are derived, an UP and LP are formed for increasing coupling strengths. As evident in the plots, avoided crossing of the exciton and cavity mode is observed if sufficient coupling is present. In this simulation the cavity detuning Δ, defined as $E_X - E_C(0)$, is kept constant. At the angle θ_{res}, at which exciton and cavity are in resonance, the minimum energy difference between upper and lower polariton is reached. This energy splitting is called Rabi energy and is given by[96]

$$\hbar\Omega = 2\sqrt{{V_A}^2 + 0.25\left(\hbar\Gamma_X/2 - \hbar\Gamma_C/2\right)^2}. \tag{2.35}$$

The Rabi frequency Ω similarly describes the rate of energy exchange.[96] For strong coupling to be present, the energy exchange must be faster than the median dissipation rate of excitons and photons in the system[96, 105] [97,107]

$$\Omega > \frac{\Gamma_X + \Gamma_C}{2}. \tag{2.36}$$

Hence, the Rabi splitting must be larger than the linewidths of the uncoupled oscillators resulting

in the condition

$$\hbar\Omega > \frac{\hbar\Gamma_X + \hbar\Gamma_C}{2}. \tag{2.37}$$

All values can be experimentally determined and are thus often used for experimental determination of strong light-matter coupling. The Rabi splitting scales with the square root of the oscillator of the emitter molecules and number of coupled oscillators, for example, molecules or quantum wells.[104] The condition for strong light-matter coupling leads to the following condition for the coupling potential required for strong light-matter coupling:[101, 108, 109]

$${V_A}^2 > \frac{\hbar{\Gamma_X}^2 + \hbar{\Gamma_C}^2}{8}. \tag{2.38}$$

Figure 2.13 visualizes the increasing mode splitting of the UP and LP for increasing coupling strength. By measuring the dispersion of the modes inside the cavity, the light-matter coupling can thus be directly investigated. For this purpose, typically angle-resolved spectroscopy is performed.[110–112] The hybrid light-matter character can be quantized by calculating the exciton and photon fraction in the polariton branches (Figure 2.13, bottom). In addition to the mode splitting, the light-matter hybridization across all angles increases for higher coupling strengths.

Further, the cavity detuning can be employed to tune light-matter content in these systems. Figure 2.14 shows the polariton branches and the exciton and photon fractions in the LP for different cavity detunings. In all cases, the Rabi splitting is identical at the angle of resonance. At these points, the LP consist of 50% exciton and photon. For increased negative detuning, this resonance is observed at larger angles and the LP becomes predominantly photonic at small angles. The specific strength of the light-matter hybridization and the cavity detuning strongly influence the exciton-polariton dynamics as shown in the next section.

2.3.3 Exciton-polaritons

The LP and UP that form in the strong light-matter coupling regime were shown to have a mixed exciton and photon fraction. The exciton-polaritons occupying these modes are thus hybrid light-matter quasiparticles.[105] Upon excitation, the polariton branches will be populated, which might be observed by polariton emission leaking from the cavity.[108] This behavior can be investigated by optically pumping the polariton branches either resonantly, i.e. $E_{\mathrm{Pump}} = E_{\mathrm{LP}}$,[113] or non-resonantly at higher energies.[114] In the latter case, incoherent excitons are created which rapidly relax within the excitonic structure of the material forming an exciton reservoir at the lowest excitonic state.[115] This exciton reservoir in turn is pumping the polaritons by radiative or non-radiative processes as illustrated in Figure 2.15. Since the polaritons carry excitonic properties, further relaxation along the LP towards the energetic minimum occurs before the polaritons will decay. The lifetime of the polaritons τ_{LP} is given by linear superposition

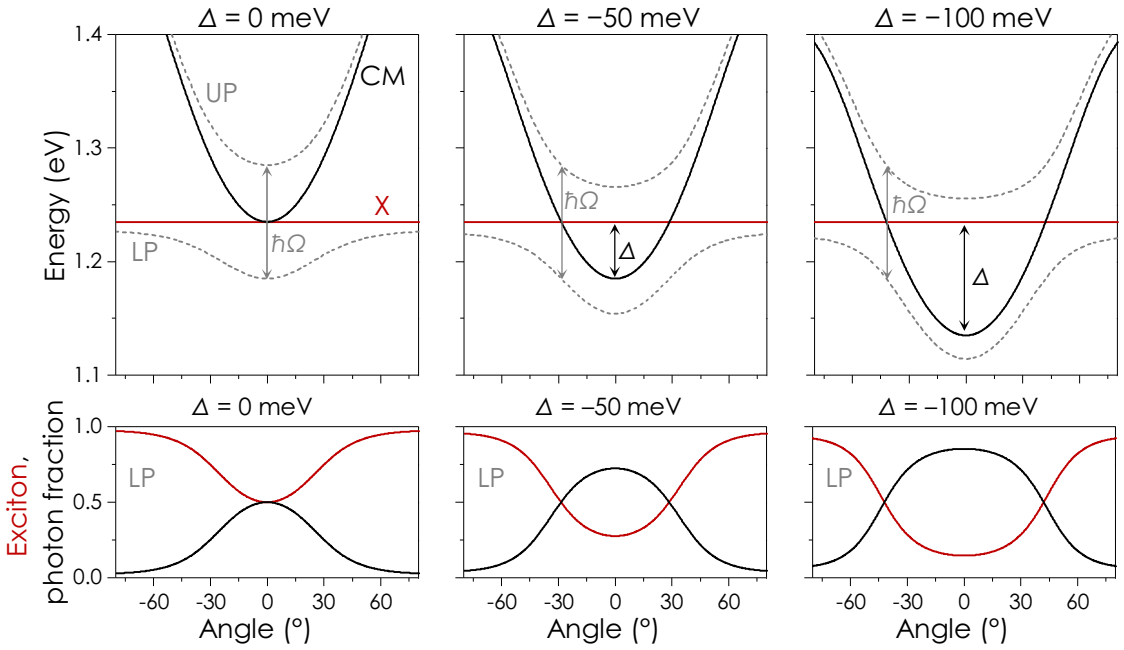

FIGURE 2.14. Coupled oscillator model for varying cavity detuning.
From left to right, the dispersion the UP and LP (top) and the exciton and photon fraction (bottom) as calculated with the coupled oscillator model for increasing negative detuning.

of the excitonic and photonic decays and is given by

$$\tau_{\mathrm{LP}}{}^{-1} = \alpha^2\ \tau_{\mathrm{C}}{}^{-1} + \beta^2\ \tau_{\mathrm{X}}{}^{-1}. \tag{2.39}$$

Due to their finite lifetime, the polaritons typically decay via their photonic component.[116] The emitted intensity from the cavity I can be directly correlate to the population of the polariton branch N by its photonic component:

$$I = \alpha^2\ N. \tag{2.40}$$

The observation of PL from the polariton modes is thus a powerful tool to investigate the polariton dynamics as well as absolute population.[108, 116, 117]

Generally, polaritons relax towards the lowest energetic state (ground state), which is found at k = 0 in the LP. Since exciton-polaritons are bosons, they can all occupy the same state.[108, 118] For relaxation much faster than the polariton lifetime, the polaritons in the LP can be thought of as an interacting boson gas at the ground state.[119] The interactions, arising from the excitonic component, lead to population of energetically higher states. If thermalization of the polaritons is observed, efficient scattering towards the ground state is present.[109] The population of polaritons N_{LP} is then described by Boltzmann exponential distribution[109]

$$N_{\mathrm{k=0}}(E_{\mathrm{k=0}} - E)\ \propto \exp\left(\frac{E_{\mathrm{k=0}} - E}{\mathrm{k_B}T}\right). \tag{2.41}$$

Here, $E_{k=0}$ is the energy of the ground state, k_B is Boltzmann constant and T denotes the effective temperature of the polariton gas. Note, despite thermalization of the polariton cloud, the polariton system is not in thermal equilibrium owing to the constant leakage and generation (in case of continuous pumping) of polaritons.[109]

If instead the relaxation towards the ground state is not sufficient, a relaxation bottleneck will occur and thus their distribution along the LP deviates from that of thermalized polaritons. Characteristically for a relaxation bottle neck, energetically higher states are more populated than in an ideal Boltzmann distribution.[114, 120–122] Overcoming the relaxation bottleneck can be accomplished by, for example, increasing the excitonic fraction of the LP, adjusting the cavity detuning, and increasing the polariton density.

Inherent to bosons, the scattering rate towards a given bosonic state depends on the occupation of this energy state. As an example, the scattering rate towards the ground state $R_{k=0}$ in the LP depends on the mean ground state occupation $\langle n_{k=0} \rangle$ itself:[123]

$$R_{k=0} \propto \left(1 + \langle n_{k=0} \rangle\right) R_{k=0}. \tag{2.42}$$

If the mean occupation is larger than unity, the relaxation rate towards this state itself increases resulting in a higher population, which increases the scattering rate further – a process called stimulated scattering. Due to this macroscopic ground state occupation, the wave functions of the polaritons start to overlap and a polariton condensate is formed.[124] The emission from these polariton condensates has many similarities to those of photon lasers: threshold-like behavior, coherence, linewidth-narrowing, and reduction in excited state lifetime.[97, 108, 117, 125, 126] In contrast to photon lasing that requires population inversion, the polariton lasing threshold is reached for a ground state occupation larger than unity. This results in lasing threshold that can be orders of magnitude below those observed for photon lasing.[117] In polariton lasers, the coherence arises from the collective wave function of the polariton condensate rather than from stimulated emission. In addition, the macroscopic wave function of polariton lasers enabled the observation intriguing physical phenomena, for example, superfluidity at room-temperature.[127]

2.3.4 Materials for strong coupling and polariton condensation

Various materials have been employed for strong light-matter coupling ranging from epitaxially grown quantum wells in inorganic materials[110] to perovskites[128] and 2D materials;[111] organic molecules[126] and polymers[125]; proteins[117] and bacteria[129]. Initially, the hybrid light-matter states were observed in GaAs quantum wells at cryogenic temperatures.[130] The observation of polariton condensation in these systems[131, 132] led to a rapid evolution in the field of cavity quantum electrodynamics.[109, 133–135] These early experiments typically involved complex device manufacturing and required cryogenic temperatures due to the low binding energy of the Wannier-Mott excitons (<25 meV) in inorganic materials.[135] Additionally, the relatively small oscillator strength in these materials limits the observed Rabi splitting to a

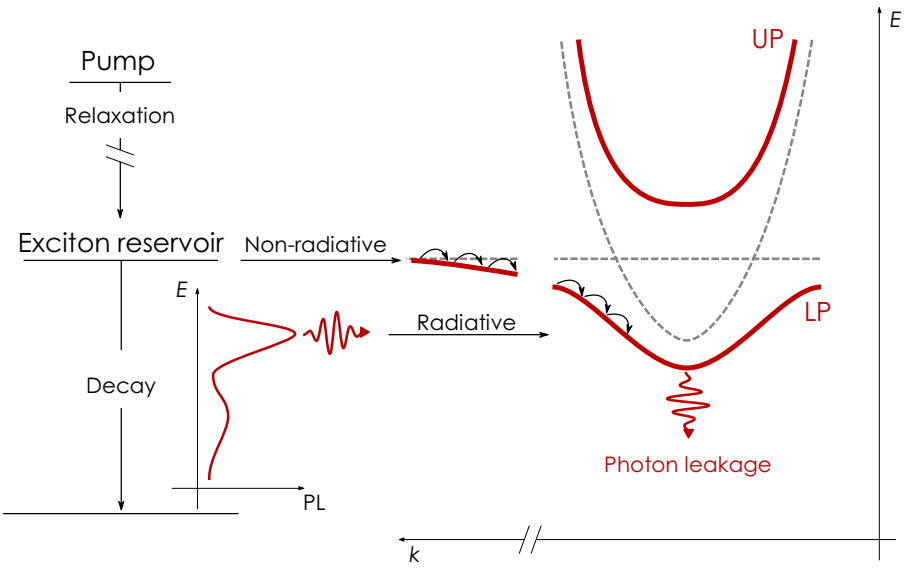

FIGURE 2.15. Lower polariton pumping scheme.
The dispersion of the UP and LP were calculate with the coupled oscillator model.

few meV.[132, 135] To bring these experiments closer to elevated temperatures, materials with higher exciton binding energies have been employed, such as GaN and ZnO.[136, 137]

Room temperature stability of exciton-polaritons and related phenomena was observed for organic materials in 1998 by Lidzey *et al.*.[138] This pioneering work revealed many advantages of the employed organic material. All experiments were performed in a metal-clad cavity at room temperature with Rabi splittings of more than 100 meV. Polariton lasing was first observed in organic materials by Kéna-Cohen *et al.* in 2010 using crystalline anthracene.[108] Characteristic fingerprints associated with polariton condensation were shown in this work, for example, stimulated relaxation, polariton lasing threshold, and a sharp decrease in lifetime. Subsequently, non-linear interaction and polariton lasing was shown using the polymer MeLPPP[125] and the oligomer TDAF[97, 124, 139]. This work revealed the long-range coherence that can be observed in polariton condensates (across ~100 µm) even though most organic material are inherently disordered. Recently, enhanced green fluorescent protein was employed to achieve polariton lasing with ns pulsed pump laser.[117] The spectral shift and the reduced threshold, with respect to photon lasing, emphasize the unique properties of polariton lasers.

In general, the disordered environment and fabrication of organic materials leads to a limited quality factor of the surrounding cavity and thus polariton lifetime. While for epitaxially grown inorganic materials quality factors of few thousands were achieved,[110] for organic materials quality factors are typically only a few hundreds.[125] For the hybrid exciton polaritons, these disorder effects can be overcome by the delocalization of the light field. Hence, macroscopic coherence[125] and superfluidity[127] were observed in polariton condensates. Challenges that

occur by using organic materials are associated with the limited stability of these molecular materials due to the reduced heat conductivity in organic materials as well as photobleaching. These limitations are particularly challenging with respect to electrical pumping as described in the next section.

2.3.5 Electrical pumping of polaritons

Polariton lasers might offer a path for lasing with materials that lack high PLQY but offer efficient relaxation paths and high electrical conductivity. As a result, exciton-polaritons may eventually enable electrically pumped lasing with carbon-based materials. Moreover, electrical generation of polaritons in organic devices presents a platform to study fundamental quantum-physical phenomena at room temperature and with simple fabrication.

Organic materials inherently offer room-temperature stability of exciton-polaritons due to their large exciton binding energy. Electrically pumped exciton-polaritons in organic materials were first observed by Tischler *et al.* in an OLED-cavity using J-aggregates.[140] The cavity was formed between two reflective metallic electrodes resulting in strong coupling with a Rabi splitting of 265 meV. Angle-resolved spectroscopy was used to confirm that the EL originates from the polariton branches with substantial signal originating from the UP. To date this work reported the highest pump rate, with a current density of $0.1\,\mathrm{A\,cm^{-2}}$, for organic cavities in the strong coupling regime.[141–146] Subsequent studies, however, improved on other aspects of the devices and investigated polariton behavior upon electrical excitation.

As an example, in TPP-filled cavities, no difference in the relaxation of the polaritons was observed for EL and PL.[141] Generally, electrical excitation might exhibit superior relaxation due to an increased electron-polariton and electron-exciton scattering. For other materials, this effect might improve the polariton relaxation significantly. Improvements of the cavity quality factor were achieved by the group of Lidzey using an OLED-cavity with a transparent ITO electrode and a DBR mirror.[143] In this work, a quality factor of ~60 was achieved in the strongly coupled cavity. Nevertheless, these polariton devices suffered from a significantly reduced EQE compared to an uncoupled reference OLED. An EQE of 0.1% was achieved in ultrastrongly coupled TADF-filled OLED-cavities at low current density and quality factor.[144] Electrical pumping of ultrastrongly coupled polaritons results in almost dispersionless emission with high color purity.[144–146] These devices might prove useful in information displays that require high color purity and viewing angle stability.

In conclusion, electrical excitation of polaritons at room temperature and high current densities remains an open challenge. From previous work, three main challenges can be defined: First, the relaxation of electrically injected polaritons must be studied and increased. In analogy to optical pumping, the relaxation bottleneck might be overcome at higher pumping rates or by employing materials with intrinsically efficient relaxation mechanisms. Second, the pumping rate must be increased in order to increase the ground state occupancy of the polariton states. Hence,

for electrical pumping, the current density in the devices must be increased. Third, the polariton lifetime must be increased to accumulate more polaritons within a lifetime cycle. Therefore, the quality factor of the cavity needs to be increased by employing highly reflecting mirrors.

CHAPTER 3

EXPERIMENTAL METHODS

This chapter lists the materials and describes the various experimental techniques and simulation software used in this thesis.

3.1 SWCNT selection

Polymer wrapped SWCNT dispersions by shear force mixing (SFM). Monodisperse (6,5) SWCNT dispersions were prepared by selective polymer-wrapping from CoMoCAT® raw material (Sigma Aldrich 773735, Lot #14J017A1). According to the supplier, this CoMoCAT® material has an overall SWCNT-content of 88%, of which 40% are (6,5) chirality. Hence, ~35 wt% of the raw material are (6,5) SWCNTs.

For selective polymer-wrapping with SFM, 0.5 g L^{-1} PFO-BPy (poly[(9,9-dioctylfluorenyl-2,7-diyl)-alt-co-(6,6'-{2,2'-bipyridine})], American Dye Source, M_W = 34 kg mol^{-1}) were dissolved in 140 mL toluene and then 0.38 g L^{-1} CoMoCAT® raw material were added. Hence, approximately 17 mg (6,5) SWCNTs were used initially. High-speed SFM (Silverson L5M-A) was then applied at maximum speed (10,230 rpm) for up to 96 h. During mixing, the temperature of the dispersion was kept constant at 20°C. After mixing, the dispersion was centrifuged at 50,000 to 60,000 g (Beckman Coulter Avanti J26XP centrifuge) for 45 to 60 min with an intermediate supernatant extraction and centrifuge tube exchange after 15 to 30 min. After the centrifugation step, the supernatant contained high purity (6,5) SWCNTs. By reusing the pellet, formed during this centrifugation, instead of adding raw CoMoCAT® material, SWCNTs were recycled up to eight times. Fresh PFO-BPy (0.5 g L^{-1}) and fresh toluene (140 mL) were added and previous SFM steps were repeated with the pelletized nanotubes.

To obtain further enriched dispersions, (6,5) SWCNTs were pelleted via ultracentrifugation at 284,600 g (Beckman Coulter Optima XP ultracentrifuge). Depending on the desired concentration,

these pellets were then redispersed in a small volume of toluene or washed with toluene to remove excess polymer. Polymer wrapped SWCNT dispersions by sonication. Bath (tip) sonication was applied to 10 mL (20 mL) of toluene with 2 g L^{-1} (0.5 g L^{-1}) PFO-BPy and 1.5 g L^{-1} (0.38 g L^{-1}) CoMoCAT® raw material for 6 h (5.5 h). The temperature of the dispersion was kept constant at 20°C for sonication either in the ultrasonic bath (Bandelin Sonorex Digitec DT 102 H) or in using the tip sonicator (Sonics Vibra Cell, pulsed mode at 20% power output). The dispersion was followed by centrifugation of the mixture at 60,000 g for 45 min with an intermediate supernatant extraction and centrifuge tube exchange after 15 min.

Surfactant-suspended SWCNT dispersions by sonication. (6,5) SWCNTs were prepared from 15 mg of the same CoMoCAT® raw material and suspended in 2 wt% aqueous sodium dodecyl sulfate (SDS, Merck KGaA) solution. Initial dispersion was performed by tip sonication (Weber Ultrasonics, 35 kHz, and 500 W, in continuous mode at 20% power output) for 1 h at 15°C. Next, the dispersion was centrifuged at 100,000 g for 1 h and decanted. Owing to the high affinity of (6,5) SWCNTs to the Sephacryl-S200 gel (Amersham Biosciences at 1.6 wt% SDS, water was added before application to a gel column. Here, 1 wt% sodium cholate (Sigma Aldrich) was used as the eluent. Density gradient ultracentrifugation was carried out in a 1 wt% sodium cholate solution with a stepped density gradient of iodixanol (from bottom to top of the centrifuge tube) 40 wt% /30 wt% + (6,5) SWCNTs /20 wt%. Surfactant-suspended SWCNT dispersions were carried out by Benjamin Flavel (Karlsruhe Institute of Technology).

3.2 Device fabrication

3.2.1 OLEDs

OLEDs were fabricated on pre-patterned ITO (indium tin oxide, 90 nm thick) on a 1.1 mm thick glass-substrates. After cleaning with acetone and isopropanol in a sonication bath and ozone treatment for 3 min, a 40 nm thick layer of PEDOT:PSS (poly(3,4-ethylenedioxythiophene) polystyrene sulfonate) was spin-coated onto the substrate. The samples were then annealed at 120°C for 20 min. Next, SWCNT dispersions were spin-coated at 2000 rpm and annealed for 30 min at 120°C in nitrogen environment. The HBL, ETL and cathode were then deposited on top by thermal evaporation at a base pressure of $2 \cdot 10^{-7}$ mbar (Angstrom EvoVac). Subsequently, BAlq (bis-(2-methyl-8-chinolinolato)–(4-phenyl-phenolato)-aluminum(III)) as HBL (10 nm thick) and BPhen (4,7-diphenyl-1,10-phenanthroline) doped with cesium as ETL (130 nm thick) were thermally evaporated. Finally, a 100 nm thick aluminum electrode was deposited. The OLEDs were then encapsulated under nitrogen atmosphere with a glass lid and getter material. The active device area, defined by the overlap of cathode and anode, was 16.1 mm^2 for all OLEDs. All thermally evaporated layers in the OLEDs were processed by Caroline Murawski (St Andrews University).

3.2.2 Metal-clad microcavities

Metal-clad microcavities were fabricated by sandwiching a layer of SWCNTs embedded in a polymer host (PFO-BPy) between two gold mirrors. First, a 60 nm thick gold bottom mirror was deposited onto a polished silicon wafer covered with 2 nm chromium for adhesion by thermal evaporation (Univex 350G). Next, polymer films (PFO-BPy) containing SWCNTs were spin-coated onto the bottom mirror at moderate speeds, ranging from 800 to 1500 rpm. For achieving the desired film thicknesses of ~250 nm, pellets of (6,5) SWCNTs were redispersed in PFO-BPy (25 g L^{-1} in toluene) by bath sonication for 5 min. Different amounts of SWCNT-pellets were used to adjust the concentration in the resulting layer. In this work, three different dispersions were spin-coated with peak absorbances of up to 240 cm^{-1} of the (6,5) SWCNTs, which corresponds to 0.43 g L^{-1} of (6,5) SWCNTs. A thermally evaporated gold top mirror completed the cavities. For the pure PFO-BPy reference cavity and for cavities with 1.71 wt% SWCNTs a 30 nm thick top mirror and for all other cavities a 20 nm thick top mirror was used.

A thickness gradient across the samples was formed owing to the intentionally low speeds during film fabrication. These long-range thickness variations enabled the study of thickness-dependent effects in cavities with identical concentration of SWCNTs. Thickness variations of the cavity across the spot under investigation during angle-resolved spectroscopy (diameter, ~3 nm) were negligible. Hence, all measurements for a given concentration were performed on the same sample.

3.2.3 LEFET-cavities

Cavity-LEFETs were fabricated by integration of a top-gate/bottom-contact LEFET on top of an electrically isolated bottom mirror resulting in an optical cavity with the gate electrode. The bottom mirror (2 nm Cr and 30 nm Au) was evaporated through a shadow mask onto a glass substrate (Schott AF32 Eco). Next, an aluminum oxide spacer layer was grown on top by atomic layer deposition (Ultratech Savannah S100) at 200°C using trimethylaluminium as precursor and water as the oxygen source. By varying the thickness of this spacer layer between 130 nm and 310 nm, the cavity detuning was adjusted. Subsequently, a LEFET was built onto this stack. First, interdigitated gold source/drain electrodes (2 nm Cr/ 30 nm Au), deposited by electron-beam evaporation, were structured by photolithography and lift-off. Channel lengths of 5, 10, 20 and 40 nm and widths of 10 and 5 mm were used. After the electrode deposition, highly concentrated (6,5) SWCNT dispersions were deposited via spin-coating at 1000 rpm on top of the source-drain electrodes. The nanotube concentration and layer thickness was adjusted by dispersing different amounts of (6,5) SWCNT pellets in small volumes of toluene. Before dispersion, the pellets were repeatedly washed to remove any residual PFO-BPy. After spin-coating, the SWCNT films were annealed at 300°C in a nitrogen atmosphere for 45 min to remove residual organic solvent and water.

Next, a hybrid dielectric of PMMA (poly(methyl methacrylate)) and HfOx (hafnium oxide) was applied. The devices were coated with an 11 nm thick PMMA layer (Polymer Source, syndiotactic, M_W = 300 kg mol^{-1}). PMMA (6 mg mL^{-1}) was dissolved in anhydrous n-butylacetate and spin-coated at 6000 rpm. After annealing at 80°C, a 61 nm HfOx layer was deposited by atomic layer deposition at 100°C using tetrakis(dimethylamino)hafnium as a precursor and water as the oxygen source. The cavity-LEFET was finalized by 60 nm of thermally evaporated silver which formed the top mirror of the cavity and the gate electrode of the transistor. All LEFETs were fabricated by Martin Held (Heidelberg University).

3.3 Characterization techniques

3.3.1 Structural and optical properties

Atomic force microscopy (AFM). Topography scans were carried out with an AFM (Bruker Dimension Icon) in tapping mode. On the one hand, the surface roughness and SWCNT distribution in dense networks were measured by AFM. In addition, samples with well-separated SWCNTs on a polished silicon wafer were scanned to measure the length of the nanotubes. For this purpose, dilute dispersions were spin-coated onto the cleaned wafer and rinsed with THF to remove residual polymer or surfactant.

Absorption and PL spectroscopy. Absorption spectra of dispersions and films were recorded with a Cary 6000i UV/Vis/NIR absorption spectrometer (Varian). PL spectra and PL excitation-emission map acquisition of SWCNT dispersions and films were recorded with an Acton SpectraPro SP2358 (grating 150 lines mm^{-1}) spectrometer with an OMA-V InGaAs line camera (Princeton Instruments). For excitation, the spectrally separated output of a WhiteLase SC400 supercontinuum laser source (Fianium Ltd.) was used. All spectra were corrected for background signal and wavelength-dependent detection efficiency and excitation power.

EL spectroscopy of OLEDs. The EL spectrum of OLED pixels was measured by placing the device 15 cm away from the entrance of an optical fiber. The collected nIR signal was then coupled into an Acton SpectraPro SP2358 spectrometer equipped with a liquid-nitrogen-cooled InGaAs line camera (Princeton Instruments OMAV). Alternatively, the emission in the visible part of the spectrum was detected by a fiber spectrometer with a silicon CCD detector (Ocean Optics USB4000-UV-VIS). The spectrum in the visible and the nIR were stitched by normalizing to the signal between 850 to 1050 nm.

Angle-resolved EL from OLEDs (goniometer). For angle-dependent EL spectra of OLEDs, a goniometer was used. For this purpose, the OLED was mounted on a rotational stage and EL spectra were taken in 5° steps. A polarization filter was used to block the transverse electric polarized light. The degradation of the OLEDs that occurred during the measurement was monitored by taking a reference spectrum before and after the angular scan. Significant degradation during

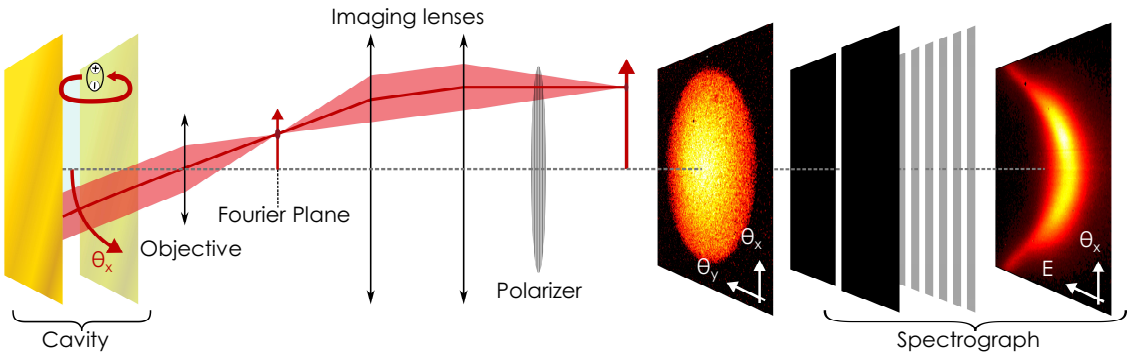

FIGURE 3.1. Angle-resolved spectroscopy by Fourier imaging.
Angle-resolved spectroscopy on a planar cavity by Fourier imaging.

detection of the angular EL spectra was absent as the peak intensity was found stay within 95% of the original intensity.

Imaging. Micrographs and hyperspectral images of nIR emission (PL and EL) were acquired with a home-build microscope setup equipped with a dichroic long-pass filter (cut-off wavelength, 850 nm), a spectrograph (Princeton Instruments IsoPlane) and a thermoelectrically cooled 640×512 InGaAs array camera (Princeton Instruments, NIRvana:640ST). Depending on the magnification, either a nIR-corrected lenses or objectives were used.

Fourier imaging.(Figure 3.1) For angular reflectivity spectra, the emission of a calibrated lamp was focused onto the sample by a nIR corrected objective with 0.8 NA (Olympus LMPL100xIR). The resulting spot diameter of 3 µm defined the investigated area on the sample. For angle-resolved PL measurements, the white light source was replaced by a laser diode (OBIS, Coherent Inc., 640 nm, continuous wave, 1 to 40 mW). The light reflected/emitted by the cavity was imaged onto the entrance slit of a spectrometer (Princeton Instruments IsoPlane) using a 4f Fourier imaging system and was recorded by a 640x512 InGaAs camera (Princeton Instruments, NIRvana:640ST). Additionally, a long-pass filter (cut-off wavelength, 850 nm) and a linear polarizer were placed in front of the spectrometer. Initial angle calibration of the system was done by fitting the measured cavity mode of a reference sample of known refractive index. For LEFET-cavities, the reflectivity of the cavity was then normalized to a spot on the same sample, which only comprised the top mirror (gate).

3.3.2 Electrical properties

For OLEDs. Current–voltage characteristics of OLEDs were recorded with a source-measurement unit (Keithley, SMU2400) under ambient conditions.

For LEFET-cavities. Current-voltage characteristics were recorded with an Agilent 4156C Semiconductor Parameter Analyzer or a Keithley 2612A source meter. Gate dielectric capacitances were measured with an Agilent E4980A Precision LCR Meter. The linear charge carrier mobilities were calculated from the transfer characteristics at a drain voltage $\pm 0.5\,\mathrm{V}$ assuming the gradual channel approximation for field-effect transistors and using a measured areal capacitance of 100-150 $\mathrm{nF\,cm^{-2}}$. The current density in these devices was calculated from the measured drain current by using the known width of the channel and assuming a 5 nm thick accumulation layer. All LEFETs were characterized by Martin Held (Heidelberg University).

3.3.3 Measures of efficiency

Photoluminescence quantum yield (PLQY). The efficiency of an emitter is characterized by its efficiency of radiative emission, called PLQY. It provides the probability of radiative decay and is given by[147]

$$\mathrm{PLQY} = \eta_{\mathrm{rad}} = \frac{\text{Number of emitted photons}}{\text{Number of absorbed photons}}. \tag{3.1}$$

An absolute experimental determination of the PLQY was carried out in an integration sphere (LabSphere, Spectralon Coating). For this purpose, an appropriate reference (used solvent, blank substrate etc.) was placed inside the sphere (Figure 3.2a). Firstly, the intensity of the excitation source (575 nm, spectrally separated output of a WhiteLase SC400 supercontinuum laser source from Fianium Ltd.) was recorded accounting for any substrate or host material absorption. All spectra from the sphere were transmitted via an optical fiber and coupled into an Acton SpectraPro SP2358 spectrometer with an OMA-V InGaAs line camera (Princeton Instruments). In addition, any background or substrate emission was recorded as well. Next, the sample under investigation was positioned in the sphere (Figure 3.2a). Again, the excitation source intensity was measured and the PL signal recorded. By multiplying the detected intensity with the corresponding wavelength, a quantity proportional to the number of photons was gained for all spectra. The difference in excitation source (PL signal) corresponded to absorbed (emitted) photons. Finally, the ratio of the two measures was taken yielding the absolute PLQY. Note, special care had to be taken to correct for the detector sensitivity and any wavelength dependent losses in the setup. Especially, for (6,5) SWCNTs, for which the excitation at 575 nm was in the visible spectrum whereas emission was observed in the nIR at 1000 nm. Further, for highly concentrated samples a self-absorption correction was applied (Figure 3.2c).[148]

External quantum efficiency (EQE). The EQE of a device takes into account all possible loss mechanisms that might occur from current injection, charge recombination, exciton formation and decay to outcoupling of the generated photons. In experiment, the injected charges can be often directly monitored by measuring the current flowing in the device. For determining the outcoupled photons, two approaches are applied. One way is to use a detector of much larger area

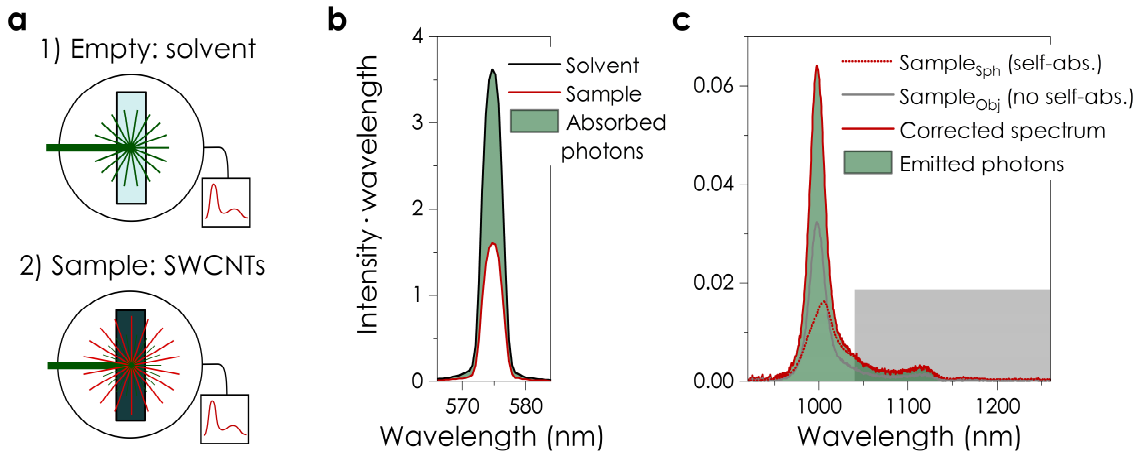

FIGURE 3.2. Photoluminescence quantum yield measurement in an integration sphere. a, Illustration of the absolute PLQY measurement used throughout this work. b, Exemplary excitation spectra without (black) any nanotubes and with (red) (6,5) SWCNTs in the integration sphere. c, Recorded emission spectrum for a highly concentrated dispersion in the integration sphere (red, dotted) and through an objective (grey). The self-absorption corrected spectrum is obtained by matching the two spectra in the shaded wavelength range (red, solid).

in close proximity to the device. Hence, it can be assumed that all photons are being detected. In a different approach, the detector can be placed at a known distance from the light-emitting device. The angular emission pattern is then used to reconstruct the overall outcoupled photons.

For OLEDs, a calibrated Ge photodetector (Thorlabs, PDA50B-EC) was employed to measure the EQE. To block emission in the visible part of the spectrum a dichroic 900 nm long-pass filter was placed in front of the sensor. The EQE was calculated from the forward emission intensity and spectrum assuming a Lambertian emission pattern.[87]

For LEFETs, total light output was measured with calibrated InGaAs photodiode (Thorlabs FGA21-CAL, active area 3.1 mm^2) directly at the glass substrate of the devices collecting most of the outcoupled light. The EQE was then calculated from the maximum photocurrent I_{diode} measured at the photodiode during a sweep of the gate voltage for a constant drain current (I_{d}). Taking into account the wavelength-dependent sensitivity of the photodiode S(λ), the EQE is given by

$$\eta_{\mathrm{EQE}} = \frac{I_{\mathrm{diode}}}{I_{\mathrm{d}}} \cdot \frac{\int \lambda \, \mathrm{EL}_{\mathrm{norm}}(\lambda) \, \mathrm{d}\lambda}{\int \mathrm{S}(\lambda) \, \mathrm{EL}_{\mathrm{norm}}(\lambda) \, \mathrm{d}\lambda} \cdot \frac{e}{hc} \,, \tag{3.2}$$

with $\mathrm{EL}_{\mathrm{norm}}(\lambda)$ being the normalized EL spectrum emitted by the respective LEFET.

3.4 Computational techniques

3.4.1 Complex refractive index

Optical simulations require the knowledge of the complex refractive index of the employed material. For widely used materials, these data were taken from the scientific database refractive index.info. In case of SWCNTs and PFO-BPy, ellipsometry experiments were conducted to determine their complex refractive index. In these measurements, homogeneous layers of the material under investigation were deposited onto a substrate of known refractive index. Here, thin layers of pure PFO-BPy and (6,5) SWCNTs embedded in PFO-BPy were spin-coated on a Si-wafer. Each material or composite combination was based on at least three different layer thicknesses. Ellipsometer measurements were carried out by Laura Tropf at the University of St Andrews using an ellipsometer from J.A. Woollam Co. (model M-2000DI). In this experiment, reflectivity spectra were taken at different angles of incidence for the different layer thicknesses for both TE and TM polarized light. All the data were then simultaneously fed into a fitting routine, which reconstructed a complex refractive index. In addition, the polarization data allowed determining the anisotropy of the refractive index.

3.4.2 Transfer-matrix simulation

The transfer-matrix algorithm is a tool for simulating the optical properties of multilayer stacks. It can be used for simulating both reflectivity and transmission spectra as well as the emitted light from within the stack. Here, a script written in Python and MATLAB was utilized. The algorithm calculates the propagation of planar waves across interfaces and the propagation through each material considering multiple reflections. The input for the program are the layer thicknesses, their complex refractive index and emitter characteristics for simulation of emission patterns.

3.4.3 Analysis of data from Fourier imaging

Acquisitions of angle-resolved spectra by Fourier imaging yields images that are rich with information. For fast and unbiased analysis of these data, an automated MATLAB script for conversion and fitting of key parameters was written.

First, the detected angle range was assigned. For this purpose, a reference cavity with PFO-BPy of known refractive index was measured by Fourier imaging and compared to transfer-matrix simulations. The measured dispersion was then compared to the simulation allowing to fit the cavity thickness and the range of viewing angles. This result was in agreement with the NA of the objective. To identify any present modes, each spectra was fitted by one or two Lorentzian peaks. The energetic peak position for all angles was then used for further analysis, for example, the coupled oscillator model or cavity dispersion.

CHAPTER 4

SELECTIVE DISPERSION OF SWCNTS BY SHEAR-FORCE MIXING

The following chapter reports on selective polymer-wrapping of monochiral (6,5) SWCNTs by high-speed shear-force mixing. In contrast to previously used techniques, involving harsh sonication, shear-force mixing is identified to be a highly efficient, scalable and at the same time gentle dispersion method.

Part of this chapter was published in Graf *et al.*, Carbon 105, 593 (2017) under the creative common license (CC BY-NC-ND 4.0).[1] Modified reprints are presented with permission of Elsevier Ltd.

4.1 Introduction

Arising from their one-dimensional structure, SWCNTs offer highly desirable properties for advanced optoelectronic devices (*cf.* Chapter 2.1). Among these desired characteristics are narrow emission linewidths and diameter-dependent bandgaps that enable spectral tunability across the entire nIR (900–2000 nm). Applications in the field of bio-imaging[149] or optical communication[150, 151] require large amounts of electronically pure SWCNTs. Here, the particular focus is on semiconducting nanotubes as needed in the active components of optoelectronic devices, such as LEFETs or OLEDs. The growth of SWCNTs on an industrial scale, however, results in a mixture of semiconducting and metallic nanotubes.[152] Therefore, post-growth sorting is applied to select one particular electronic type[55] or even specific chiralities[61] (*cf.* Chapter 2.1.5).

Among the various selection methods, selective polymer wrapping is particularly promising due to its exceptional selectivity towards semiconducting SWCNTs.[42, 65, 153] As an example, selective polymer-wrapping can achieve almost monochiral (6,5) SWCNT dispersions by utilizing the polyfluorene derivative PFO-BPy (*cf.* Figure 4.1a for molecular structure).[47, 65] For this

thesis, the sorting of (6,5) SWCNTs with the aid of PFO-BPy was chosen because previous studies revealed multiple advantages compared to other sorting techniques.[64, 68] First, the low metallic content in the obtained SWCNTs enables their used in electronic devices without shorts. Second, monochiral samples simplify any interpretation of optical as well as electronic properties in the bulk. Last, the reduced inter-tube interactions of polymer-wrapped nanotubes also lead to relatively high PLQYs in ensembles.

Polymer-wrapping, as well as other selection methods, require an initial separation of the unsorted and bundled nanotube material. The SWCNT-bundles are usually separated by harsh sonication methods.[154, 155] While ultrasonic treatment is a well-established dispersion technique, various fundamental limitations and drawbacks are coming along with using it during SWCNT selection. On the one hand, the cavitation effects during sonication were found to not only separate the nanotubes but harm the carbon lattice and cause scission of the SWCNTs.[37, 156] Damaging and shortening the SWCNTs, in turn, detrimentally affect the optical and electronic properties. For example, length-dependent studies of the optical properties of SWCNT dispersions showed a substantial reduction in PL brightness for shorter tubes.[157] Experiments on individual nanotubes revealed that this effect is related to exciton quenching at the open ends and defects along the imperfect SWCNT.[37] With regard to electronic properties, the charge carrier mobility across SWCNT-networks increases with the length of the individual tubes because of a reduction in intertube barriers.[158] From a practical standpoint, sonication lacks reproducibility as its effectiveness critically depends on the exact experimental conditions. For instance, the position of the dispersion to the source of ultrasound, the filling level and the material of the vial strongly affect experimental results. Finally, dispersion by ultrasound is accompanied by significant challenges for up-scaling to industrially relevant quantities and is therefore typically employed for volumes well below 100 mL.

Alternative dispersion methods, including ball milling and high shear batch disperser, have been used for exfoliation of SWCNT for advanced composites.[159] For selective dispersions of SWCNTs, the methods are limited to the use of micro-fluidizers in aqueous dispersions.[156] In the related field of dispersing two-dimensional nanomaterials, direct shearing was identified to enable exfoliation of large amounts of monolayers with low defect densities.[160, 161] For graphene, shear-force mixing (SFM) was shown to be efficient even at large volumes of up to several liters.[160]

In the remainder of this chapter, the experimental results of high-speed SFM for selective dispersion of carbon nanotubes by polymer-wrapping are studied. Interestingly, SFM enables the selection of high-quality (6,5) SWCNTs in large volumes and with high yield. The excellent quality of the SWCNTs, dispersed by shearing, manifests in exceptionally long nanotubes with considerably brighter PL than previously reported. A direct comparison to SWCNTs dispersed by sonication confirms the superior properties of shear-force mixed SWCNT dispersions.

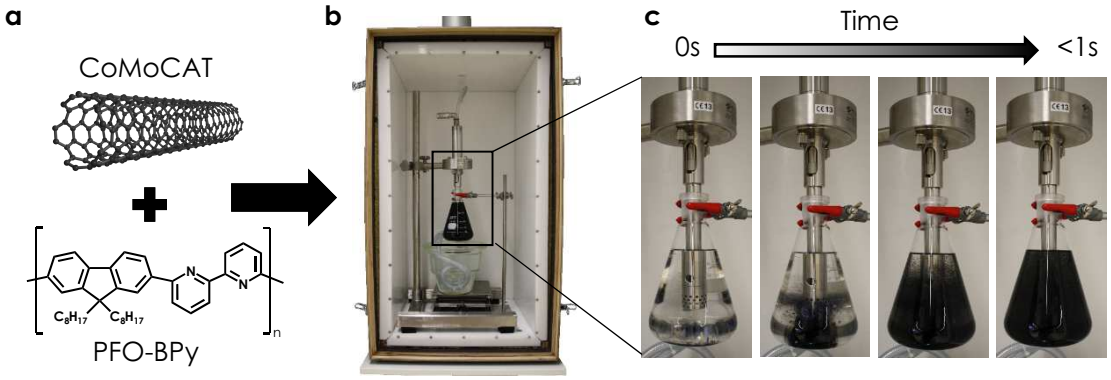

FIGURE 4.1. SFM for selective polymer-wrapping of (6,5) SWCNTs.
a, Molecular structure of (6,5) SWCNTs and the copolymer PFO-BPy. b, High-speed shear-force mixer used for dispersing SWCNTs. c, Evolution of the dispersion during the first second after starting the mixer. The black color arises from the unsorted SWCNT source (CoMoCAT®) while the dissolved polymer PFO-BPy is colorless at these concentrations.

4.2 Dispersion by SFM

For the dispersion of SWCNTs, a commercially available, high-speed shear force mixer (Silverson L5M-A) was employed (Figure 4.1b). The mixer comprises a stator with perforations enclosing a rotor that spins at up to 10,230 rpm. Based on previous work,[47] (6,5) SWCNTs can be selected from CoMoCAT® starting material by adding PFO-BPy dissolved in toluene. Both, the nanotubes and the polymer, were added to 140 mL of toluene at concentrations of 0.38 and 0.5 g L^{-1}, respectively. The relative ratio of SWCNTs to polymer was adopted from previous work on selective polymer-wrapping.[162] The absolute concentration was adjusted to increase the circulation during SFM resulting in more homogeneous mixing. While the dissolved polymer at these concentrations resulted in a colorless mixture, the solution quickly (within one second) turned black after starting the mixer (Figure 4.1c). The quick distribution of the black carbon nanotube powder in the flask indicated active SFM across the sample. During mixing, the dispersion is pulled into the stator by the movement of the rotor. At the same time, the dispersion within the stator is milled between the gap of the rotor and stator, before being spun out of the perforation in the stator. By carefully positioning the mixer, the circulation of the dispersion is maintained. Also, the temperature of the dispersion was constantly kept at 20°C because the continuous shearing produced heat and elevated temperatures are known to reduce the wrapping efficiency.[163]

4.3 Optical characterization of (6,5) SWCNTs from SFM

After 96 hours (4 days) of mixing, the black dispersion was subsequently centrifuged to separate the unwrapped material (sediment) and the wrapped SWCNTs (supernatant). Figure 4.2a shows the absorption (black line) of the collected supernatant. The spectrum primarily shows features associated with (6,5) SWCNTs, such as the S_{11} and S_{22} transitions, which are observed at 996 and 575 nm, and their phonon sidebands. (For a detailed analysis of the sample purity, the reader is referred to the end of the section.) Using the molar peak extinction coefficient of 6,700 $M^{-1}\,cm^{-1}$, allows to estimate the concentration of (6,5) SWCNTs in this dispersion.[164] The absolute concentration in the supernatant (more than 100 mL) was ~2.3 $mg\,mL^{-1}$. As both, the concentration and volume, exceed by far the results achieved for sonication-based methods, they are an indication of the effectiveness of the shear forces in separating SWCNTs.

Interestingly, reusing the sediment remaining after the initial process in another SFM cycle drastically increased the yield of (6,5) SWCNTs. In this recycling process, the sediment was added to a fresh polymer solution instead of new CoMoCAT® material. After the first recycling, the dispersion showed a purple color (Figure 4.2b), originating from strongly enriched (6,5) SWCNTs with an absorption band of the S_{22} transitions in the green-to-yellow part of the spectrum. The concentration of (6,5) SWCNTs in the recycled sample was found to be almost three times larger than in the initial dispersion (Figure 4.2a). In this case, the absorbance at the S_{11}-transition was more than 3 cm^{-1}. Further repetition of recycling gave even more (6,5) SWCNTs with a concentration remaining as high as in the initial round for up to three recycling steps. Overall, 1.8 mg of (6,5) SWCNTs were extracted during these experiments. Considering that the starting material contained around 35 wt% of (6,5) SWCNTs, more than 10% of these nanotubes were separated from the rest of the material. These results on recycling of the undispersed nanotubes are in agreement with previous experiments with large-diameter SWCNTs.[165] While recycling generally increases the SWCNT yield, the quality of the dispersion must be carefully evaluated because the longer processing time might have an impact. For SFM, possible effects are discussed in the following section.

As mentioned above, SFM was applied for 96 h in these experiments. In order to investigate whether shorter mixing times (t) might be sufficient, the (6,5) SWCNT concentration (c) was measured (Figure 4.2c). While the initial rise in selected (6,5) SWCNTs is steep, saturation is observed for longer mixing times. The time evolution can be approximated by a saturation model

$$c(t) = c_{\max}\,\frac{t}{t_{1/2}+t} \tag{4.1}$$

where $c_{\max}$ is the saturation concentration and $t_{1/2}$ the time after which 0.5 $c_{\max}$ is reached. The fit of the data reveals a maximum (6,5) SWCNT concentration of 3.3 $mg\,mL^{-1}$ (i.e., absorbance of 1.9 cm^{-1}) with half of it reached after 38 h. Consequently, a mixing time of three to four days

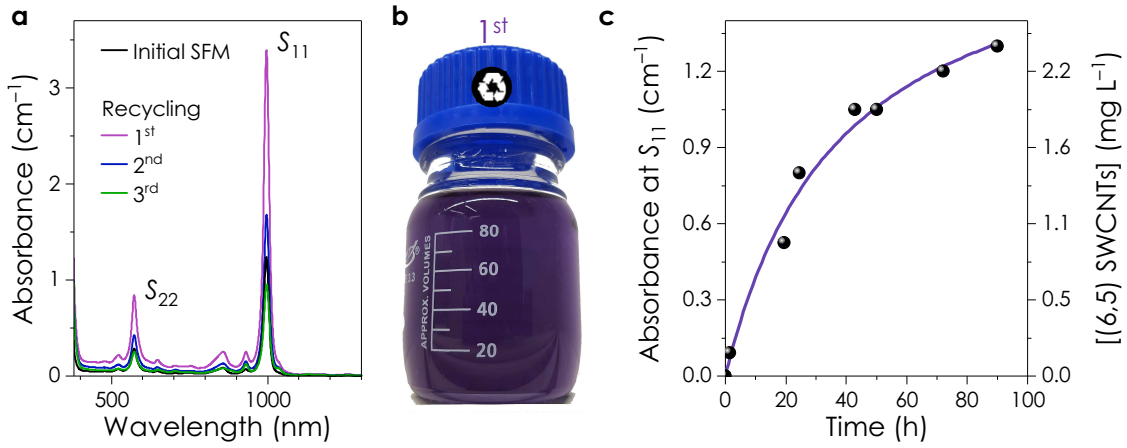

FIGURE 4.2. Yield of (6,5) SWCNTs in shear-force mixed dispersions.
a, Absorption spectra of the supernatant collected after initial SFM and recycling of the sediment. In the spectra, characteristic absorption peaks of the excitonic transitions in (6,5) SWCNTs are identified. b, Photograph of the supernatant collected after one round of recycling. The purple color is associated with a high concentration of pure (6,5) SWCNTs with narrow absorption in the green-to-yellow part of the spectrum. c, (6,5)-SWCNT concentration during four days of SFM.

presents a good trade-off between maximum concentration and minimal mixing time. In practice, this allows around two dispersion to be processed per week and mixer.

The most important criteria for using the selected nanotubes as an active material in opto-electronic applications is the purity of the SWCNTs. Concerning the electronic grade, no metallic SWCNTs were observed in the absorption spectrum. The metallic content was thus (at least) below the resolution limit of the absorption spectroscopy and hence estimated to be below <0.1%. At the same time, absorption peaks that are not related to (6,5) SWCNTs could be identified in the absorption spectrum (Figure 4.2c). More insight into the specific chirality of these SWCNTs was gained by recording a PL-excitation (PLE) map of the dispersion (Figure 4.3a). The correlation of excitation and emission energy enhances the visibility of SWCNTs besides the abundant (6,5) SWCNTs. The (6,5) SWCNTs dominate the PL signal of the SFM sample across all excitation wavelengths. To further improve the visibility of other emitters, the normalized (6,5) SWCNT spectrum (recorded under resonant excitation, i.e., at 575 nm) was subtracted for each excitation wavelength (Figure 4.3b). This representation of the PLE map reveals several other SWCNT chiralities, for example, (7,5) and (8,3) as marked in the figure. Quantitatively analyzing these data is not representative due to different PL efficiency between chiralities and energy transfer toward low-bandgap tubes, which might unequally alter the emitted intensities. However, knowing which chiralities are present allows us to precisely fit the absorption spectrum (Figure 4.3c). In this multi-peak fit a Lorentzian line-shape for each S_{11}-exciton and Gaussian line-shape for the phonon sideband of the (6,5) SWCNT S_{11}-exciton was assumed. The computed

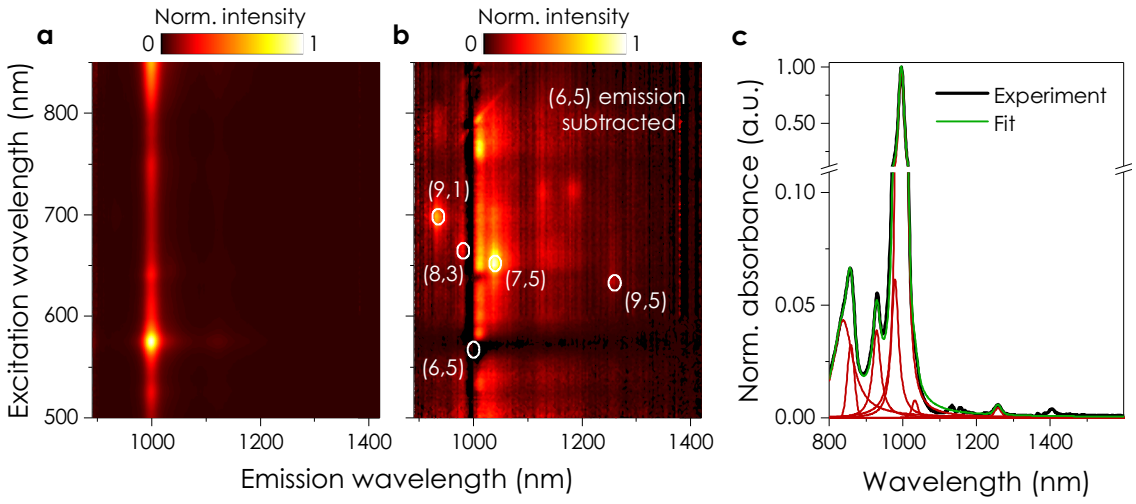

FIGURE 4.3. Purity of (6,5) SWCNT dispersions by SFM.
a, PLE map of the SWCNT-enriched supernatant obtained by SFM and subsequent centrifugation. The map is dominated by PL from (6,5) SWCNTs at resonant (excitation at 575 nm) and off-resonant excitation. b, The same PLE map with (6,5) SWCNT emission being subtracted, enhancing the contribution of other semiconducting nanotubes in the sample. For this purpose, the normalized (6,5) SWCNT spectrum at resonant excitation was subtracted for all excitation wavelengths. In this plot, (9,1), (8,3), (7,5) and (9,5) SWCNTs are identified. c, NIR-absorption spectrum of SFM dispersion (black line) superimposed with the multi-peak fit (green line). For fitting, the species found in the PLE map were used.

best fit reveals an abundance of (6,5) SWCNTs of 84%. The remaining 16% are distributed among other semiconducting nanotubes. As will be shown in the next section, these impurities are in agreement with sonication-based dispersion methods but the SWCNTs selected by SFM exhibit superior structural and optical properties.

4.4 Quality measures of selected SWCNTs

As shown in the previous section, SFM enables the selection of almost monochiral (6,5) SWCNTs in large volumes. In order to reach the highest concentrations, the polymer-nanotube mixture was processed for up to 4 days in the SFM. In experiments with sonication-based dispersion methods, significant scission was observed after only a few minutes of processing.[166] The impact of SFM on the nanotubes was first investigated by the length of the dispersed SWCNTs. Therefore, the obtained SWCNTs were sparsely distributed on a Si wafer, and the length was then determined for a large number of SWCNTs from an AFM topography scan. Figure 4.4a plots the length distribution of 340 individual SWCNTs. On average the SWCNTs were 1.82 µm long (standard deviation of 1.12 µm and median length of 1.55 µm) with more than 40% being longer than 2 µm. In comparison to SWCNT lengths obtained with sonication-based methods in the

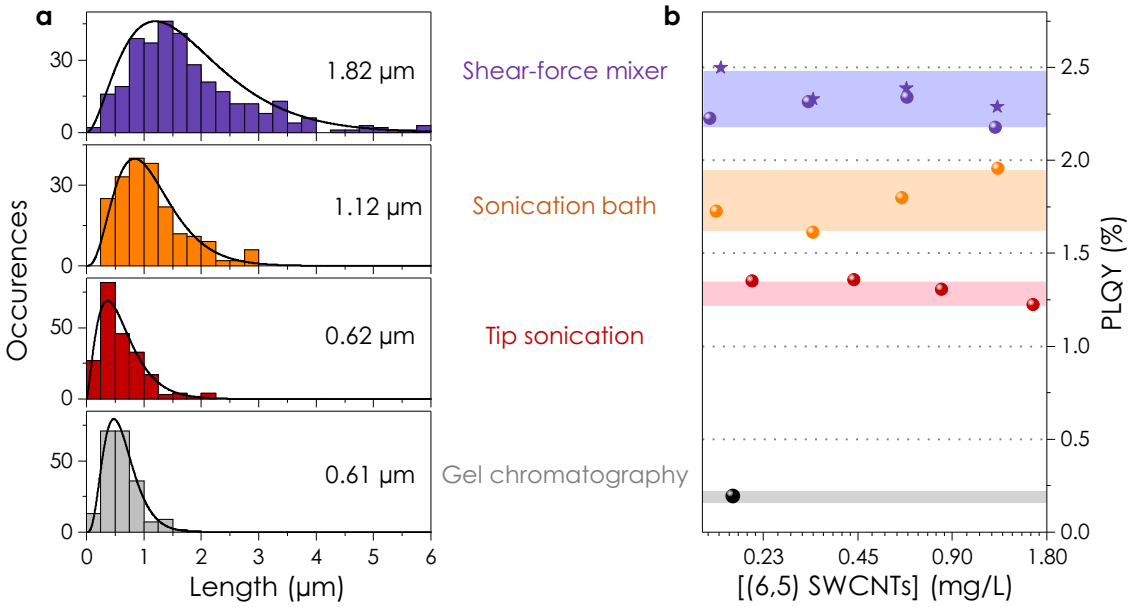

FIGURE 4.4. Impact of dispersion method on SWCNT length and PLQY.
a, Length distribution of (6,5) SWCNT selected by different methods. The average length is provided for each plot. b, PLQY versus concentration for the dispersion investigated in (a).

literature,[68, 154, 156] the shear-mixed SWCNTs are substantially longer. The observation of relatively long SWCNTs suggests that SFM is a mild dispersion method minimizing scission and possible damage to the SWCNTs.

To benchmark the SWCNTs obtained from SFM, the properties of the nanotubes were compared to sonication-based polymer dispersions. For this purpose the same raw material of CoMoCAT® SWCNTs was dispersed in 2 mg mL^{-1} PFO-BPy dissolved in toluene using a sonication bath (tip) for 6 h (5.5 h). In addition, (6,5) SWCNTs were sorted by gel chromatography and DGU in water for which initial sonication of the raw material was applied. The lengths of more than 200 individual nanotubes per method were measured to compare the impact of each selection process on the SWCNT-quality (Figure 4.4a). In contrast to SFM (1.82 µm average length), the selection processes that involved sonication led to substantially shortened SWCNTs. On average, SWCNTs selected by polymer-wrapping using a sonication bath (tip) were found to be 1.12 µm (0.62 µm) long. Moreover, an aqueous dispersion in water sorted by gel chromatography showed a SWCNT-length of 0.61 µm.[1] Note, the generally larger length of nanotubes selected after four days of SFM might be further increased by shorter mixing times, as observed for the size of graphene flakes.[160]

As mentioned above, long and pristine SWCNTs are highly desirable due to their superior electrical and optical properties. These manifest in an increased network-mobility[158, 167] and

[1] Surfactant-suspended SWCNT dispersions were prepared by Benjamin Flavel (Karlsruhe Institute of Technology)

the observation of higher PLQYs[39]. The latter one can be explained by the diffusive character of excitons in SWCNTs.[168] In this picture, non-radiative quenching along the carbon lattice strongly reduce the efficiency of radiative decay. Quenching sites can be of variable nature, such as, defects in the lattice, open ends of the nanotube, and local environmental interaction. In ensemble measurements, all effects are measured simultaneously. Hence, the PLQY is a good measure of the SWCNT-quality as long as environmental conditions are the same, for example, solvent and inter-tube interactions.

In literature, the PLQY of SWCNTs was measured by relative comparison to the nIR dye Styryl 13.[29, 39, 62, 169] The results of this experimental technique directly links the PLQY of SWCNT to that of the dye. This approach is well accepted in the community for well-studied reference molecules. The PLQY of the dye used for SWCNTs, however, was in some studies assumed to be >11% (Ref. [29, 62]) while other, more careful studies, measured a PLQY of 2–3.5% for Styryl 13 (Ref. [39, 169]). As a result, the published results can vary strongly depending on the valued that was taken for the calculation. In fact, the author himself found a strong variation for the emitter depending on solvent, age of solution, concentration and dispersion condition.

To shed more light on the actual PLQY, a direct measurement of the PL efficiency within an integration sphere was established for SWCNTs.[147] Briefly, the number of absorbed and emitted photons was recorded simultaneously by detecting the whole excitation and emission signal across the entire spectrum. Hence, no reference emitter material was used for determining the PLQY. The adaption of this method for SWCNTs required careful experimental settings as the emission in the nIR (>1000 nm) and the excitation in the visible (575 nm) must be simultaneously recorded. The setup was checked by measuring the PLQY of a fresh dispersion of Styryl 13 in methanol exhibiting a PLQY of (3.5 ± 0.2)%, which was in agreement with the literature.[39, 169]

The PLQY of (6,5) SWCNTs, measured by the described method, is plotted in Figure 4.4b. For each dispersion technique, the PLQY was analyzed for various concentrations. As the PLQY was found to be almost constant across these concentrations range, any influence from concentration-dependent quenching due to bundling can be excluded. These results identify SFM as the dispersion technique yielding the SWCNTs with the highest PLQY for all concentrations. The average PLQY for SFM was found to be 2.4% for 43 h and 2.3% for 92 h of mixing. Since there is no significant reduction during 49 h of additional mixing, the SFM can be described as gentle dispersion method. Additionally, the roll-off at high concentrations for these SWCNT was not significant confirming the low metallic content and good individualization of polymer-wrapped SWCNTs. Otherwise, in the presence of metallic nanotubes or inter-tube interactions, a strong roll-off would be expected due to increased exciton-quenching.

Unlike SFM, polymer-wrapped SWCNT that were dispersed by sonication exhibited generally lower PLQY. The reduction is attributed to the reduced length as well as damage of the carbon lattice introduced by cavitation during sonication. While bath sonication still resulted in a PLQY of 1.8%, the more harshly tip sonicated SWCNT gave a reduced PLQY of 1.3%. These findings

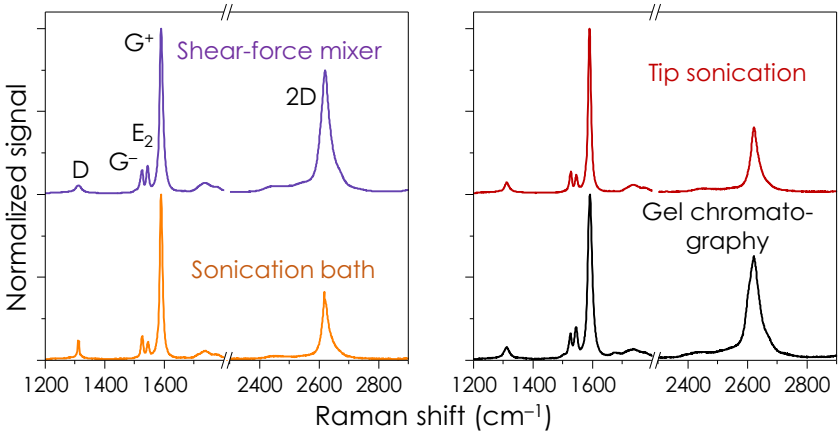

FIGURE 4.5. Raman spectra for different dispersion and selection methods. Raman signal of (6,5) SWCNTs dispersed by different techniques. Typical features are labeled for the SFM sample.

are in accordance with shorter SWCNTs after dispersion by tip sonication. SWCNTs dispersed in aqueous SDS solution exhibited a PLQY of 0.2%. In this case, several factors may limit the PLQY. First, strong tip sonication was used for initial dispersion that was likely to damage the nanotubes as discussed above. In addition, the remaining metallic nanotubes and bundling were typically higher for these samples.[62] While repetitive DGU can improve these limitations, ensemble PLQYs remain well below 1% (Ref. [62]).

4.5 Further characterization

Recently, the 2D-to-G+ ratio of the Raman signal was identified as a measure of sample quality as an alternative to the D-band intensity.[170] The G+-band is proportional to the number of sp2-carbon bonds and thus nanotubes under investigation. The 2D-peak, however, depends on the extent of the pristine graphene lattice. The Raman signal of all (6,5) nanotube samples, normalized to the G+-band, is shown in Figure 4.5. The SWCNTs dispersed by SFM exhibit the highest 2D peak relative to the G+-band. For the investigated polymer-wrapped SWCNTs, the highest 2D/G-ratio for SFM confirms the high quality observed in previous characterizations. A quantitative comparison to gel chromatography is less trivial since the surfactant (SDS), and thus the structural coverage, is very different. A more detailed discussion of the ratios is limited by the influence of the environment on the observed Raman signal and possible damage during the high-intensity laser irradiation.

Interestingly, careful analysis of the absorption and PL spectra, shown in Figure 4.6, revealed significant differences among the samples. The peak position of the S_{11} exciton exhibited a red-shift with decreasing SWCNT-quality in both, absorption and PL spectra (Table 4 1). The

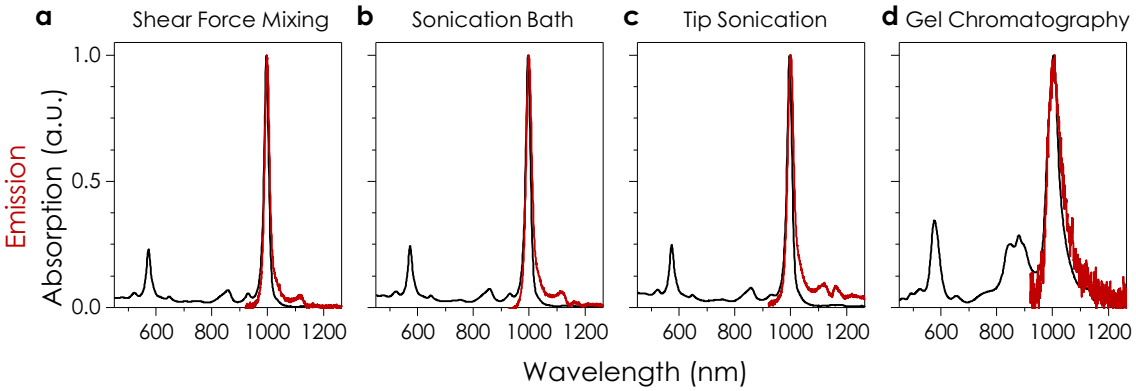

FIGURE 4.6. Influence of SWCNT-quality on basic optical properties.
Absorption and PL spectrum of (6,5) SWCNT selected by polymer-wrapping using a, shear-force mixing, b, sonication bath and c, tip sonication. d, (6,5) SWCNTs in aqueous dispersion and sorted by gel chromatography.

effect, however, is more pronounced in PL measurement resulting in an overall increase of the Stokes shift for shorter and damaged SWCNTs. This observation is most likely a consequence of defect states that can form near disordered sites in the carbon lattice forming shallow trap states. For these states, the exciton-energy landscape is locally reduced. In absorption, their influence on the overall spectrum is limited because those are only local site. However, due to the high exciton-mobility of excitons in SWCNTs, the impact of these trap states is more pronounced for PL as the diffusion length is sufficiently long to reach the defect states. Since absorption and PL spectroscopy are part of the standard characterization of each dispersion, the Stokes shift provides a handy tool for quick quality assessment. Note, for this metric to be applicable, the SWCNT dispersions must be measured immediately after the selection process. Otherwise, bundling and aggregation of the nanotube alters the measured spectra. Again, a quantitative comparison to gel chromatography is less meaningful since the surfactant coverage and refractive index of the environment (surfactant and solvent) shift and broaden these spectra significantly.

Finally, the overall yields of (6,5) SWCNTs among the techniques used for polymer-wrapping is compared (Table 4.1). During the first SFM cycle 1.67% of the (6,5) SWCNTs were extracted. In comparison to the sonication-based methods, SFM does not only lead to high-quality SWCNTs but is also a more efficient dispersion method. Particularly, the yield in comparison to the widely used bath sonication is more than 20 times higher. Thus, SFM is an efficient way to disperse SWCNTs enabling polymer-wrapping of (6,5) SWCNTs.

TABLE 4.1. Summary and comparison of SWCNT properties obtained with SFM and sonication-based dispersion techniques.

	SFM (92 h)	Bath sonication (6 h)	Tip sonicator (5.5 h)	SDS (DGU)
PLQY (%)	2.3	1.8	1.3	0.2
Mean length (µm)	1.82	1.12	0.61	0.62
S_{11}-λ_{abs} (nm)	996.1	996.3	996.3	1001.6
S_{11}-λ_{em} (nm)	997.7	998.2	999.6	1006.7
Stokes shift (meV)	2.2	2.5	3.2	5.2
S_{22}-FWHM$_{abs}$ (meV)	54.3	55.2	55.6	102.1
S_{11}-FWHM$_{abs}$ (meV)	20.1	21.1	22.4	49.4
S_{11}-FWHM$_{em}$ (meV)	23.1	24.6	27.7	51.1
(6,5)-yield (%)	1.67	0.07	0.82	-

4.6 Summary & conclusions

Overall, SFM presents a scalable and efficient method to select high-quality (6,5) SWCNTs with the aid of polymer-wrapping. The resulting dispersions were found to contain negligible amounts of metallic nanotubes and a majority of 84% (6,5) SWCNTs among the semiconducting species. Even after four days of mixing, long SWCNTs (1.82 µm) with a high PLQY (2.3%) were obtained. In direct comparison to sonication-based dispersion, SWCNTs selected by SFM exhibit superior structural (longer and less damaged) and optical properties (higher PLQY). Interestingly, the overall yield of (6,5) SWCNTs is strongly increased by using SFM compared to the widely used bath sonication. Moreover, by using repetitive recycling more than 10% of the (6,5) SWCNTs were extracted from the unsorted starting material. In additional experiments, the selection method using SFM was scaled up to volumes of more than 500 mL. In conclusion, SFM is a cost-effective dispersion method that overcomes many limitations of sonication-based selection. This technique might be extended to other polymer-wrapped SWCNTs or used for initial dispersion of aqueous selection processes. The availability of large amounts of high-quality (6,5) SWCNTs, as depicted in Figure 4.7, is essential for applying SWCNT in novel optoelectronic devices, for example as emitters in LEDs (Chapter 5), for strong light-matter coupling (Chapter 6) and for electrically pumping of exciton-polaritons (Chapter 7).

FIGURE 4.7. Photograph of highly-concentrated (6,5) SWNCT dispersions.
Photograph of a total of ~1 L of (6,5) SWCNT dispersions produced during the course of this work.

CHAPTER 5

ORGANIC LIGHT-EMITTING DIODES BASED ON EMISSIVE SWCNTS

This chapter reports on the first infrared OLED with SWCNT emitters. Narrow-band electroluminescence is generated in the nIR by excitons and trions in (6,5) SWCNTs. The in-plane orientation of the nanotubes enables efficient outcoupling of the electrically generated light from the multilayer device.

Part of this chapter was published in Graf *et al.*, Advanced Materials 30, 1706711 (2018).[2] Modified reprints are presented with permission of WILEY-VCH Verlag GmbH & Co. KGaA.

5.1 Introduction

Since their first discovery in 1965 (Ref. [69]), organic light-emitting diodes (OLEDs) have gone through a tremendous development leading to the commercialization of, for example, curved OLED-displays (Ref. [171]). This progress mainly focused on OLEDs generating light in the visible part of the spectrum. Therefore, research and development on materials and devices led to the discovery of efficient emitters covering the full spectrum from blue to red.[89, 172] In contrast, only few organic materials exist which exhibit stable and efficient emission at wavelengths beyond 800 nm in the nIR.[173] There are, however, manifold applications for such devices ranging from nIR light sources for telecommunication and night-vision displays to bio-imaging and skin treatment. So far, research on OLEDs in the nIR employed either small molecules,[174–177] polymers,[178] polymer nanocrystals[179] or solution-processed quantum dots[180]. Despite the successful demonstration of nIR electroluminescence from these materials, these OLEDs either show residual emission in the visible, contain heavy metals or lack mechanical flexibility.

As introduced in Section 2.1.4, emission of semiconducting SWCNTs can cover the entire nIR. In particular, their narrow excitonic emission can be tuned by selecting particular chiralities. At the same time, SWCNTs provide excellent photo and thermal stability. However, it has been

difficult to provide sufficient amounts of purely semiconducting SWCNTs, ideally monochiral samples, as needed for application in OLEDs. As shown in the previous chapter, SFM enables the processing and selection of high-purity (6,5) SWCNTs on a large scale. This advancement paves the way towards novel optoelectronic applications of SWCNTs, such as, in OLEDs.

In this chapter, the optical simulation and experimental realization of a multilayer OLED containing (6,5) SWCNTs as the emissive material is presented. The SWCNTs obtained by SFM were processed to form a dense layer that was electrically pumped through a pin device architecture. Optimized OLEDs produced pure nIR emission (>1000 nm) with narrow linewidth. SWCNTs were found to exhibit advantageous in-plane orientation leading to an increased outcoupling efficiency of the electrically generated light.

5.2 SWCNTs in solid films & OLED-design

Polymer-wrapped SWCNTs, as produced by SFM, can be solution-processed to form smooth and continuous films. Unlike dilute dispersions, strong intertube and substrate-tube interaction in thin films can alter the optical properties and lead to quenching of the PL.[181] In a preliminary experiment, enriched (6,5) SWCNT dispersion were spin-coated onto a glass substrate forming a dense nanotube network. Absorption and PL spectra of the layer are plotted in Figure 5.1a. As compared to the dispersions in toluene (*cf.* Figure 4.6), the main excitonic features were preserved in this layer: Excitonic absorption and emission peaks in the nIR (~1000 nm) with small Stokes shift. Importantly, a narrow emission peak at 1010 nm was observed upon optical excitation. This peak was slightly broadened and red-shifted with respect to the S_{11} exciton of (6,5) SWCNTs in toluene. The broadening and general shift are attributed to the stronger environmental fluctuations in the dense film and the environmental refractive index.[182] The SWCNTs in this layer exhibited a PLQY of 0.11%. This reduction, compared to 2.3% in dispersion, is ascribed to enhanced quenching due to, for instance, stronger dielectric screening,[41, 183] wrapping inhomogeneities[184], and quenching at tube-tube junctions and kinks in the network. Next, OLEDs compatible with SWCNT processing and properties were developed in two steps: First, the appropriate materials for electron/hole injection, transport and blocking were chosen to form a multilayer stack (Figure 5.1b). Second, the thickness of the ETL was optimized by maximizing the outcoupling efficiency using transfer-matrix calculations.[185]

In terms of material choice, a 50 nm thick hole injection and transport layer (PEDOT:PSS) was spin-coated onto a pre-patterned anode (ITO, 90 nm) on a transparent glass substrate (1.1 mm). The LUMO of PEDOT:PSS (–5.1 eV) is only slightly below that of (6,5) SWCNTs (–5.08 eV) and enables efficient hole transport towards the emissive layer (Figure 5.1c). PEDOT:PSS can be easily annealed to remove any water and become insoluble in other organic solvents, such that SWCNTs can be spin-coated from toluene on top. For electron injection and transport, a layer of Cs-doped 4,7-diphenyl-1,10-phenanthroline (BPhen) and an aluminum cathode was

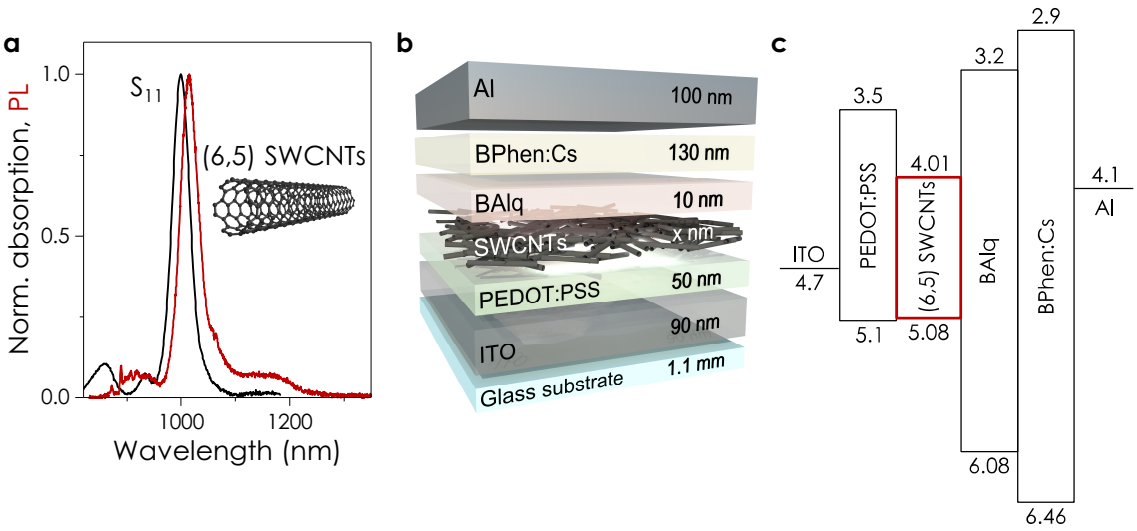

FIGURE 5.1. Optical properties of SWCNT-films and their use in multilayer OLEDs. a, Absorption and PL spectrum of a thin film consisting of (6,5) SWCNTs embedded in residual PFO-BPy host. b, Illustration of OLED based on SWCNTs. The pin-device architecture enables efficient electron and hole injection and transport towards the SWCNT layer. c, Energy level diagram of the OLED stack comprising all materials.

chosen. An additional hole-blocking layer (bis(2-methyl-8-quinolinolate)-4(phenylphenolato)-aluminium(III) (BAlq), 10 nm) was deposited between the SWCNTs and the BPhen:Cs layer. A 100 nm thick aluminum cathode ensures efficient reflection of the generated light resulting in a bottom-emitting OLED structure.[1]

Finally, a transfer-matrix simulation was used to predict the optimum ETL thickness. The algorithm requires the complex refractive indices and the thicknesses of all layers and calculates, among other parameters, the outcoupling efficiency of the multilayer stack. These predictions revealed an optimum ETL thickness of 130 nm for most efficient light outcoupling. In these simulations, a horizontally oriented (in-plane) emissive dipole moment was used emitting the PL spectrum measured for the (6,5) SWCNT film.

During processing of the OLEDs, the SWCNT dispersions were spin-coated onto the HTL layer and then annealed in dry nitrogen atmosphere before the other layers were thermally evaporated on top. To check the influence of this processing on the SWCNTs properties and possible cross-excitations from adjacent layers, a PLE map of the SWCNTs within the completed OLED was measured (Figure 5.2a). The PLE map does not show any significant contribution from a chirality other than (6,5) SWCNTs nor any cross-excitations. In addition, the SWCNT homogeneity and surface roughness across the pixel are important for the final device performance. An AFM topography scan of the used SWCNT layer is shown in Figure 5.2b. The image reveals a dense

[1]Thermally evaporated layers in the OLEDs were processed by Caroline Murawski (St Andrews University)

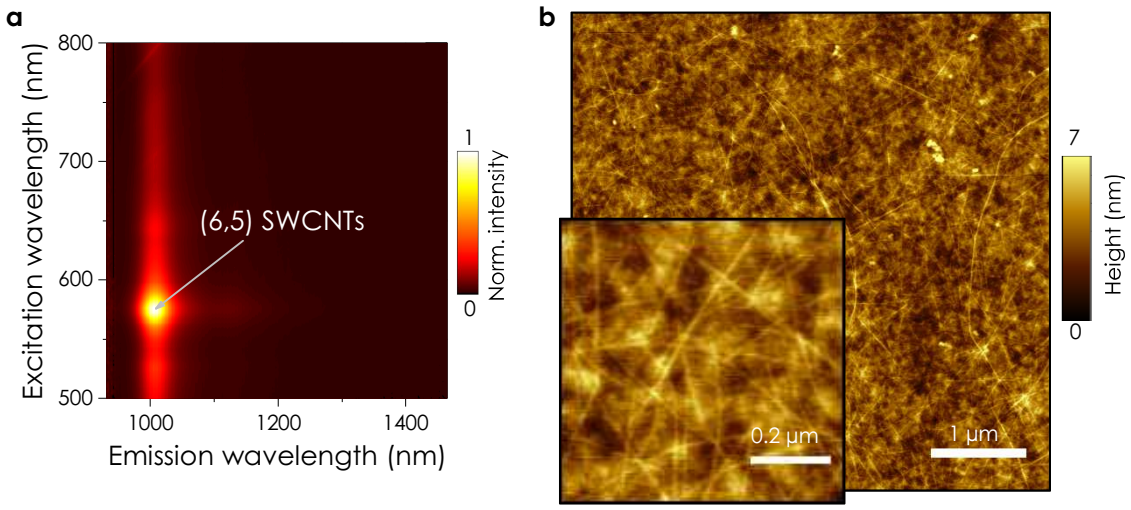

FIGURE 5.2. SWCNT-properties within OLEDs.
a, PLE map of the (6,5) SWCNT-layer within the completed OLED. No effect of processing and interaction with adjacent layers was observed and spectral features of the (6,5) SWCNTs were maintained. b, Topography scan of a thin (6,5) SWCNT-layer. The layer had a RMS sur-face roughness of 0.97 nm.

and continuous network of nanotubes with strong planar orientation. While the overall surface roughness was found to be similar to the nanotube diameter (0.97 nm), small aggregates and SWCNT-bundles were found across the layer.

5.3 Characterization of SWCNT-based OLEDs

Three OLEDs with increasing SWCNT-layer thickness of 5, 16 and 39 nm are compared in the following. The J-V-characteristics of all devices showed a clear diode-like behavior reaching a current density of 180-320 mA cm^{-2} at 5 V (Figure 5.3a). These high currents are a result of the use of doped charge transport layers enabling and supporting the injection and transport of these currents. At applied biases larger than 2.5 V, all OLEDs showed emission in the nIR (Figure 5.3b). For higher voltages, the generated nIR-irradiance varied significantly among the devices. Overall, the thickest SWCNT layer (39 nm, red) gave the highest irradiance. In this device, the aerial output power exceeded 900 µW cm^{-2} at 300 mA cm^{-2}. Accordingly, the same OLED exhibited the highest EQE as shown in Figure 5.3c. At low current density, a maximum EQE of 0.014% was reached in the OLED with the 39 nm thick SWCNT-layer. The EQE for thinner SWCNT-layers (5 nm thick film, green) decreased at these current densities to 0.006%. For all SWCNT-based OLEDs, the EQE showed a moderate roll-off at high current densities. The reduced EQE at high currents can be explained by exciton-exciton annihilation.[168] In general, the EQE of all SWCNT-based OLEDs was limited by the PLQY (0.11%). A detailed discussion of additional loss

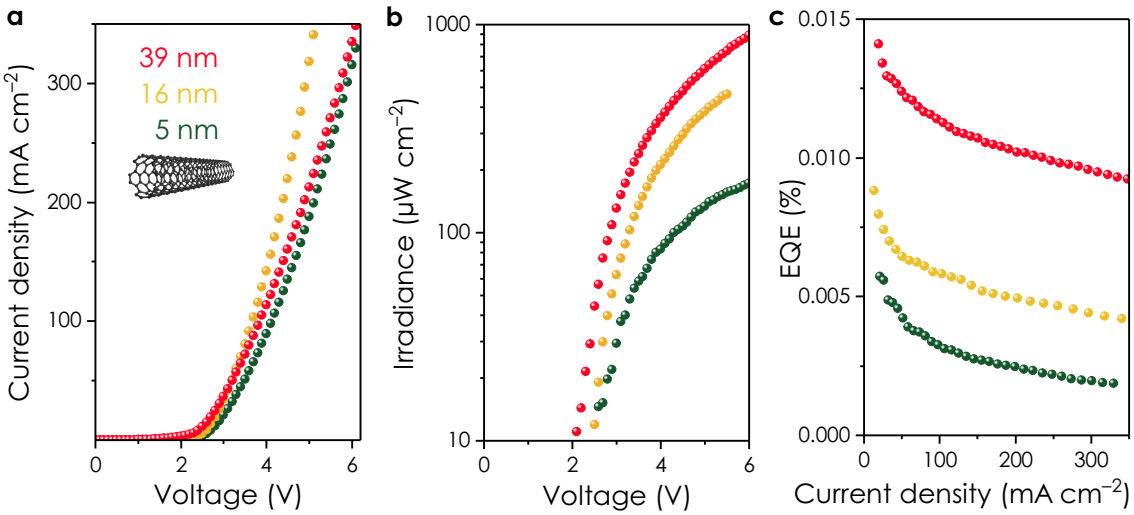

FIGURE 5.3. OLED characterization with nIR emission.
a, J-V-characteristics of SWCNT-based OLEDs fabricated with three different EML thicknesses. Diode-like behavior is observed with a threshold-voltage of ~2.5 V. b, Outcoupled nIR-irradiance of the OLEDs generated during operation in forward direction. c, EQE versus cur-rent density of the OLEDs.

channels is presented and discussed in section 5.5.

The EL spectra of all OLEDs emitted at 62 mA cm^{-2} and in forward direction, i.e. at 0° with respect to the normal of the substrate, are plotted in Figure 5.4. The emission was recorded with an InGaAs detector (900-1300 nm) and a Si detector (400-900 nm) covering the entire visible and nIR spectrum. OLEDs with as thick SWCNT-layer emitted purely in the nIR (>1000 nm). In addition to the exciton peak at 1010 nm with a FWHM of 41 nm (*cf.* PL spectrum, Figure 5.1a), a second intense peak was observed at 1177 nm with a FWHM of 58 nm. This peak is associated with a charged exciton, called trion, that was observed in literature for (6,5) SWCNTs in LEFETs and for electrochemical doping.[153, 186, 187] In case of thinner EMLs, the relative intensity of the trion emission with respect to excitonic signal increased. The origin of the emission spectra is more closely evaluated in the next section. Additionally, substantial EL in the visible was detected for these devices with peaks at 430 nm and 570 nm. This emission is attributed to exciplex formation at the interfaces to the adjacent layers as well as charge recombination within these layers. Since BAlq has by far the lowest charge carrier mobility within the stack, this effect is expected to take place predominantly at the electron EML-HBL interface and within the HBL. From these observations, a SWCNT film thickness of 39 nm is recommended to electrically generate pure nIR light.

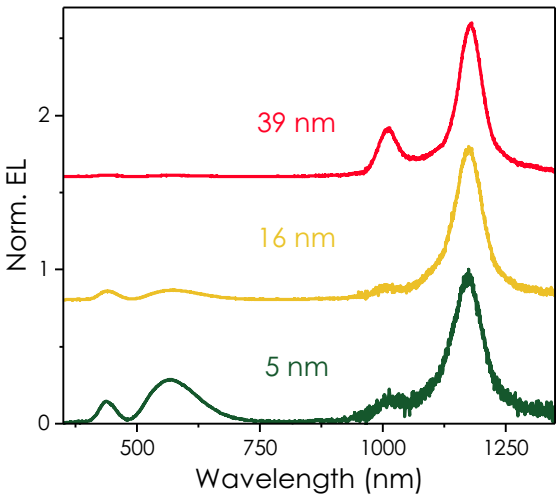

FIGURE 5.4. EL spectra generated by SWCNT-based OLEDs.
Normalized EL spectra of three OLEDs with different SWCNT-layer thickness. In the nIR the (6,5) exciton (1010 nm) and trion (1177 nm) emission is observed. Spectra were acquired at 0° with respect to the normal of the substrate. All spectra were measured at continuous operation at 62 mA cm^{-2} and normalized to the trion peak.

5.4 Trion emission

This section aims to corroborate the hypothesis of the previous section: the EL generated by SWCNT-OLEDs shows the radiative decay of trions in (6,5) nanotubes. The binding energy of these charged excitons was found to be ~100 meV for small diameter nanotubes.[188] Thus, trions in (6,5) SWCNTs are stable at room-temperature. Trions form in the presence of excess charges, which in turn bind to the minority charges in a ratio of 2 to 1. The probability of their formation, hence, should increase with current densities as the number of excess charges increases.

In order to shed more light on the origin of the spectra emitted by the OLEDs, current-dependent EL spectra were recorded. The normalized spectra for the OLED containing the thickest SWCNT layer (39 nm, red) are shown in Figure 5.5a. Being normalized to the exciton, these spectra visualize the relative increase of the peak at 1177 nm with increasing current density supporting the assignment of the peak to trions. Furthermore, this trend eliminates the possibility of electrical excitation of excitons in residual smaller band-gap SWCNT species. In that case, the minority SWCNTs would become saturated at high currents and emission would decrease with respect to the excitons in (6,5) SWCNT.

In LEFETs,[153] trions were electrically generated at a current density of up to tens of A cm^{-2} whereas in these OLEDs only current densities on the order of mA cm^{-2} are present. In case of a homogeneous current distribution, these charge carrier densities are thus not expected to lead to

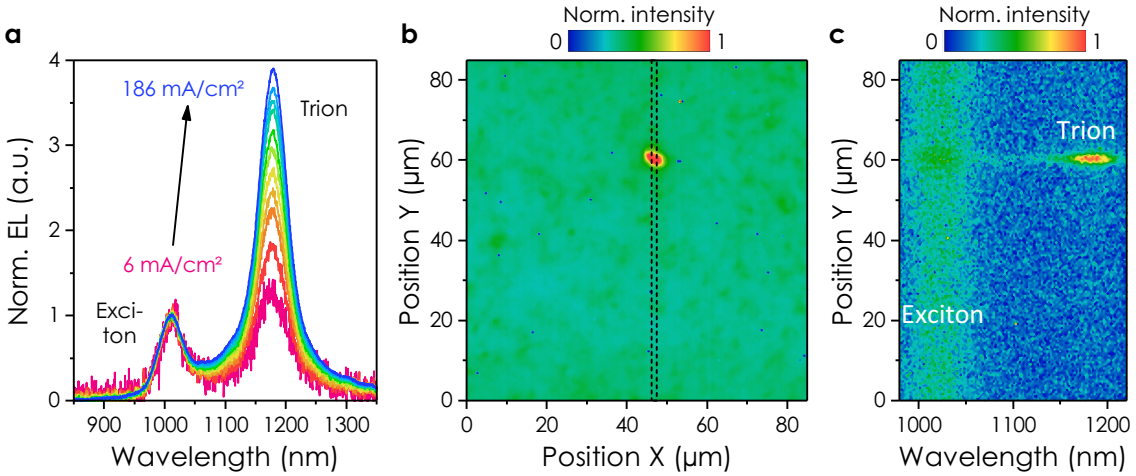

FIGURE 5.5. Trion emission from SWCNT-based OLEDs.
a, EL spectra of OLEDs based on SWCNTs for increasing current-densities. All spectra were recorded at 0° with respect to the normal of the substrate. b, Real-space image of the nIR emission from the OLED. c, Hyper-spectral image of the area marked in (b).

the formation of trions. This discrepancy is explained by the inhomogeneous spatial distribution of the current flow resulting in a locally increased current density. As an example, Figure 5.5b shows a microscope image of the nIR emission of a part of the OLED pixel. While there is a relatively constant background EL, intense emission is obtained from a hot spot. Hyperspectral imaging of the area marked in Figure 5.5b reveals that trion emission is predominantly generated from this hot spot (Figure 5.5c). At the same time, the data shows that the background signal is dominated by pure excitonic EL. The intense EL within the hot spot is assigned to a strongly increased current flowing at this position. These current densities are sufficiently large to cause the formation of trions.

An IR image of an entire pixel (4x4 mm2) reveals the intense emission from multiple hot spots (Figure 5.6a). Again, an aerial background emission is observed across the pixel. Hence, the average current density, measured across the entire pixel, is significantly higher at these points leading to the mixed contribution of exciton and trion emission. A homogeneously excited PL image of the same pixel (red box in Figure 5.6b) reveals bright spots at the same positions as observed for EL. This result suggests the presence of larger SWCNT agglomerates within the EML that form the basis for the hot spots observed in EL experiments. In summary, these investigations reveal that aggregates of SWCNT in the EML lead to increased current flowing through some hot-spots which in turn lead to trion emission.

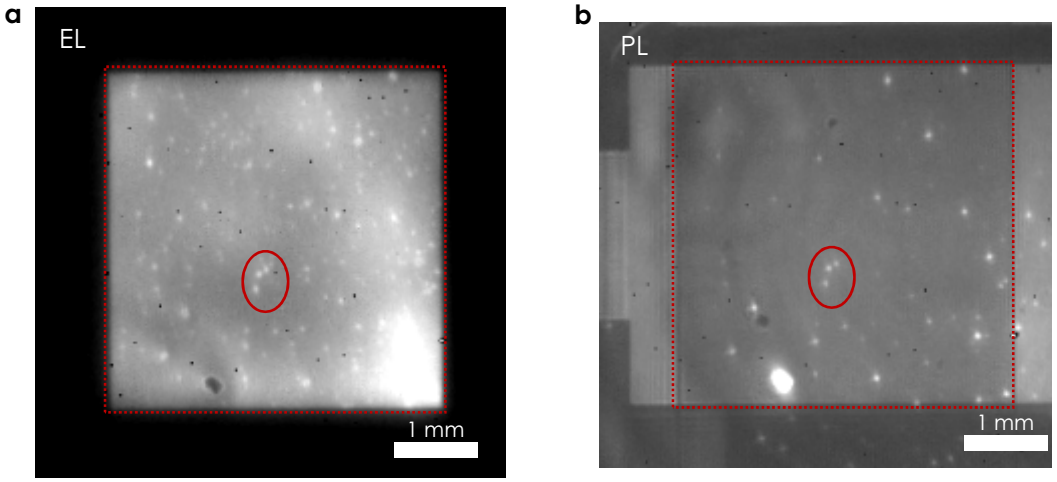

FIGURE 5.6. OLED pixel characteristics.
a, EL emitted by an OLED pixel at 62 mA cm^{-2}. Brighter spots are associated with increased emission from trions whereas the background emission is assigned to excitons. b, PL recorded under homogeneous excitation of the SWCNTs in the same pixel. Brighter spots correspond to an increased density or amount of (6,5) SWCNTs.

5.5 Emitter orientation & efficiency calculations

Due to their one-dimensional structure, SWCNTs are inherently anisotropic. When spin-coated onto a flat substrate, the nanotubes typically show strong planar orientation (*cf.* Figure 5.2b). Because the transition dipole is parallel to the nanotube axis for both excitons and trions,[153] these dipoles are expected to show preferentially horizontal orientation, which are advantageous for outcoupling of the generated light within the OLED stack.[189] In order to investigate the orientation of the transition dipoles in SWCNT-based OLEDs, the angle-resolved EL spectra were recorded (Figure 5.7a). The TE-polarized light was blocked by a linear polarizer, as it does not carry information from vertically oriented dipoles.[79] During the whole measurement, no significant degradation was observed during the measurement. Comparison of the experimental data to a transfer matrix simulation of the same stack allowed fitting of the emissive dipole orientation. For this purpose, the transition dipole anisotropy a was introduced a fitting parameter. The anisotropy factor measures the ratio of vertically oriented dipoles to the total number of dipoles.[79, 190] Isotropic (horizontal) orientation is represented by an anisotropy factor of 1/3 (0). In case of SWCNT-based OLEDs, a least square fitting algorithm gave the best fit for an anisotropy factor of 0.05, i.e. strong horizontal orientation (Figure 5.7b). The EL spectrum emitted in forward direction was used in the simulation. In sharp contrast to that, the simulated emission for isotropic orientation deviates significantly from the experimental results (Figure 5.7c). The differences are most prominent at large angles at which light from vertically oriented dipoles is

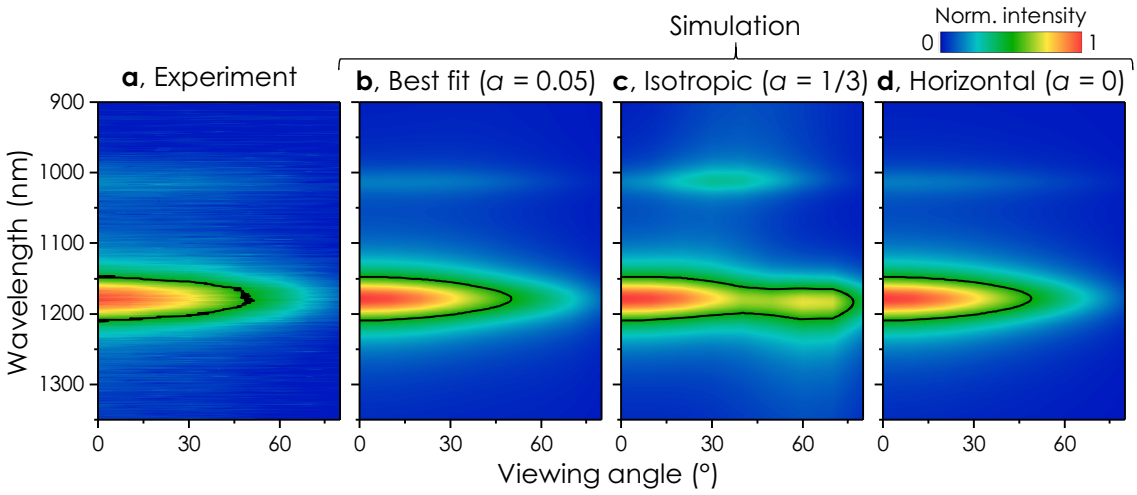

FIGURE 5.7. Angle-resolved EL spectra to determine the emitter orientation. a, Experimentally recorded angular EL spectra for a SWCNT-based OLED at 62 mA cm^{-2}. b, Simulated angular EL spectra using an anisotropy factor of 0.05. The inclination angle of 12.9° fits the experimental results best. c, Simulated angle-resolved EL spectra for isotropic and d, horizontal orientation of the transition dipole moments.

outcoupled. The simulation for perfect horizontal orientation of the transition dipole moments, on the other hand, only slightly deviates from the experiment (Figure 5.7d). The fitted anisotropy factor of 0.05 corresponds to an average inclination angle of ~12.9°, which is in agreement with the flat orientation of the nanotubes in the EML.

The preferential horizontal orientation of the emissive dipoles enhances the outcoupling efficiency of the generated light. Using transfer-matrix simulations, an outcoupling efficiency of 49% can be calculated for an anisotropy factor of 0.05. SWCNTs are thus enhancing the outcoupling by more than 60% compared to isotropic emitters. Besides outcoupled power, light couples to substrate modes, wave-guided modes in the organic materials or excitation of lossy surface-plasmons in the aluminum cathode. These components are associated with loss channels as this energy dissipates within the device. In addition to outcoupling losses, the internal efficiency reduces the maximum EQE that can be achieved theoretically. Electrically excited excitons are formed with random spin and thus 75% of these excitons are triplets. Since triplets in SWCNTs cannot decay radiatively, the maximum EQE is reduced by a factor of 0.25. The singlet emission efficiency is further given by the PLQY (0.11%). Assuming balanced charge-carrier injection, the maximum EQE that can be achieved in these OLEDs is 0.014%. At low current density, the best SWCNT-OLED reached this theoretical limit (*cf.* Figure 5.3c). Here, the presence of trions in these OLEDs might enable brightening of triplets or other dark excitons.[191] At higher current densities, all OLEDs showed a significant roll-off. Typically, annihilation processes, for example, exciton-polaron or exciton-exciton quenching are the origin for the reduced efficiency in

OLEDs.[192] In case of SWCNT, Auger quenching might further reduce the EQE at high current densities.[153] Overall, SWCNT-OLEDs showed good exciton generation and efficient outcoupling of the generated light.

5.6 Summary & conclusions

In this chapter, the first OLEDs based on SWCNTs as the emissive material were shown to generate nIR light. By engineering the SWCNT layer, pure nIR emission was achieved with maximum EQE of 0.014%. In addition to exciton emission, the formation of trions was observed within the EL spectrum. Current-dependent spectroscopy and hyper-spectral imaging revealed that these originated in locally increased current densities. These hot spots were caused by local inhomogeneities of the SWCNT-layer. The strong horizontal orientation of SWCNTs in the EML was found to lead to significantly enhanced outcoupling of the generated light.

In conclusion, solution-processed SWCNTs are well-suited for nIR light sources, such as, OLEDs. These OLEDs do not contain any heavy metal, show pure nIR emission and can be fabricated on flexible substrates. The employed dispersion are compatible with state-of-the-art deposition methods, such as, aerosol jet printing.[46] Moreover, advanced processing techniques promise to result in more homogeneous SWCNT films, which could reduce trion emission in these OLEDs.

In the presented devices, the achieved EQE (0.014%) was shown to be close to the theoretical limit. Further improvements of the overall EQE should mainly focus on increasing the PLQY (0.11%) of the SWCNTs. Recent work on chemically functionalized SWCNTs reported significantly increased PLQYs that might hold the key for efficient nIR OLEDs based on SWCNTs.[29, 193, 194]

Overall, this first demonstration of SWCNT-based OLEDs provides a basis for future nIR light sources. As more semiconducting SWCNTs can be efficiently separated, the device architecture could be easily adopted to fabricate OLEDs with SWCNT as emitters that cover the entire nIR.

CHAPTER 6

STRONG LIGHT-MATTER COUPLING IN SWCNTS

This chapter reports on strong light-matter coupling in SWCNT-filled microcavities at room temperature. In this regime, near-infrared exciton-polaritons are observed by angle-resolved reflectivity and PL spectroscopy. Upon optical excitation, the radiative decay of polaritons provides direct insights in the relaxation dynamics governed by mixed light-matter properties.

Part of this chapter was published in Graf *et al.*, Nature Communications 7, 13078 (2016).[3]

6.1 Introduction

As discussed in the previous chapter, the environment surrounding an emissive dipole can alter the characteristics of the emitted light. In case of OLEDs, this influence can be described by the Purcell effect and is utilized to maximize the emitted power.[185] By increasing the optical DOS at the cavity resonance, the emission at those energies is favored. Further increasing the interaction strength between the cavity and the emitter leads to strong light-matter coupling. This regime manifests in the emergence two hybrid light-matter states, the UP and LP.[120] In this case, the interaction between the excitons and photons is faster than the decay of each.

Strongly coupling of an excitonic transition to a surrounding microcavity offers a unique way of combing excitonic (e.g., strong interactions) with photonic properties (e.g., light mass). The created hybrid light-matter quasiparticles, so-called exciton-polaritons, can facilitate intriguing phenomena including superconductivity[127] and the formation of macroscopic polariton condensates[125] (*cf.* Chapter 2.3). Organic materials enable the observation of these exciting phenomena at room temperature because of the high binding energy of Frenkel excitons. At the same time, the high oscillator strength of these materials supports Rabi splitting as large as

the exciton energy.[103] Despite these advantages, the organic materials investigated so far are limited to the visible part of the spectrum and typically exhibit poor electrical conductivity. These properties are, however, required for practical polaritonic devices.[135]

The unique optoelectronic properties of SWCNTs present a novel material class for the exploration of light-matter coupling. On the one hand, similar to organic materials, SWCNTs exhibit a high oscillator strength, support excitons stable at room temperature and can be processed from solution. On the other hand, as typically observed in inorganic materials, SWCNTs have a high ambipolar charge-carrier mobility and show extreme thermal and photo-stability. Furthermore, strong interactions with acoustic phonons, absent in most organic materials, might provide an efficient relaxation channel for exciton-polaritons.[135] Previous work on SWCNTs in photonic cavities focused on PL efficiency enhancement,[195] integrating with and coupling to photonic crystals,[99] and single photon emission.[196] These experiments were conducted with single nanotubes or sparse nanotube networks within the cavity mode. Due to the small number of nanotubes per mode volume, these SWCNT-filled microcavities operated in the weak light-matter coupling regime.

In this chapter, strong light-matter coupling in metal-clad microcavities filled with dense networks of (6,5) SWCNTs is demonstrated at room-temperature. The high oscillator strength of SWCNTs enabled a Rabi splitting of >110 meV. Exciton-polariton emission was observed upon optical excitation providing insight into the polariton dynamics of the hybrid quantum system. These properties were studied by tuning the light-matter coupling inside the cavities. Further, the narrow (<15 meV) and directed emission was shown to be tunable across a wide range of the nIR (1,030–1,300 nm).

6.2 Strong light-matter coupling

Strong light matter coupling requires a sufficiently high coupling strength between a cavity and the emitter. The coupling potential itself scales with the square root of the overall excitonic oscillator strength per volume of the cavity mode.[120] Hence, for strong light-matter coupling to a planar microcavity, a highly absorptive layer is sandwiched between two mirrors.[104] To obtain a dense film of (6,5) SWCNTs, polymer-wrapped nanotubes were selected by SFM and strongly enriched by ultracentrifugation resulting in absorbances of more than 200 cm^{-1} at the S_{11}-transition. A first-order cavity in resonance with the exciton of (6,5) SWCNTs requires a mirror spacing of ~250 nm (assuming the refractive index to be ~2). Obtaining such thicknesses required a host material supporting the nanotubes. For this purpose, the SWCNTs were added to PFO-BPy dissolved in toluene (20 g L–1) before spin-casting the dispersions at different speeds (1,000–2,000 rpm). By utilizing different amounts of nanomaterial, three different concentrations of (6,5) SWCNTs in the polymer host were obtained (0.20, 0.46 and 1.71 wt%). A representative absorption and PL spectrum of such a film (1.71 wt%) is shown in Figure 6.1a. In analogy to mea-

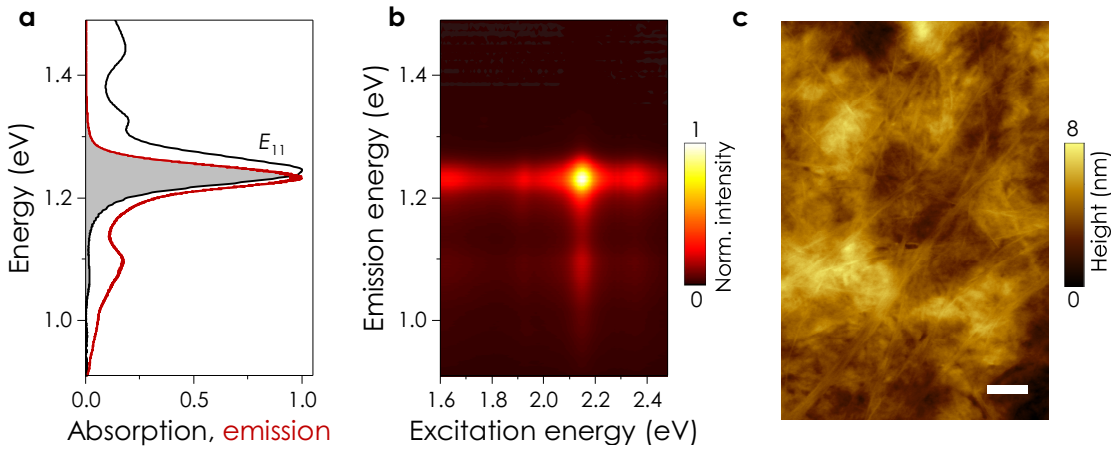

FIGURE 6.1. High-density (6,5) SWCNT film characterization.
a, Absorption and PL spectrum of a high-density film of (6,5) SWCNTs embedded in a polymer PFO-BPy host. b, PLE map of the same film showing the high purity of (6,5) SWCNTs. c, Topography scan of the layer.

surements in dispersion, the main spectroscopic features of the polymer-embedded (6,5) SWCNTs can be identified. In particular, the S_{11} absorption peak was detected at 1.243 eV (997.5 nm) which will be referred to as exciton (X) in the following. The absorption and PL peak of the exciton had a Lorentzian shape with a FWHM of 41.0 and 43.8 meV, respectively. Both linewidths and Stokes shift (8.7 meV) are considerably smaller than in most organic materials.[135] These properties are known to be desirable for an unambiguous observation of strong light-matter coupling.[197]

As can be seen in the PL-excitation map of the film (Figure 6.1b), the absence of cross-excitations and energy transfer confirms the quality and isolation of the polymer-wrapped nanotubes. Both, the wrapping-polymer and additional polymer host surrounding the nanotubes prevent substantial inter-tube interactions. In addition to the S_{11}-transition, the S_{22}-transition–observed at 2.149 eV (577 nm) – was assigned to (6,5) SWCNTs.[47] In this map, neither significant energy transfer towards smaller bandgap SWCNTs nor substantial spectral changes under off-resonant excitation were observed. Apart from the spectroscopic properties, the material inside an optical cavity must meet certain morphological properties to support a build-up of the cavity mode. Besides the desired thickness, a flat and homogeneous layer is desirable. SWCNT-embedded in PFO-BPy polymer host (~250 nm thick) resulted in a root-mean-square surface roughness of ~3 nm (Figure 6.1c). The surface roughness was well below the intended wavelength of cavity resonances (>1,000 nm). Additionally, the topography scan corroborated the homogeneous blend of nanotubes and polymer. In the next step, these films were integrated into a microcavity.

As mentioned above, strong light-matter coupling is enhanced by reducing the mode volume of the cavity resonance. In this regard, metal mirrors offer a strong confinement even though

their absolute reflectivity is limited. Thus, the SWCNT-polymer blend was spin-coated onto a thick bottom mirror (gold, 60 nm) and finalized with a semi-transparent top mirror (gold, 30 nm). The semi-transparency simplified spectroscopic investigation while maintaining the required cavity effect. Spin coating, on the other hand, resulted in a wedge-like layer thickness across the sample. Hence, the cavity resonance could be easily tuned by investigating different positions across the sample.

All cavities were characterized by angle-resolved spectroscopy through the semi-transparent top mirror. The home-build Fourier-imaging setup resulted in a 2 µm spot being investigated. In a preliminary experiment, a reference cavity was characterized containing solely the polymer host material (PFO-BPy). Figure 6.2a shows the angular reflectivity spectra for TE-polarized light displaying a cavity resonance of reduced reflectivity. The dispersion of the cavity mode (CM) was fitted to the parabolic dispersion derived in Chapter 2.3.1 (Equation 2.24). The fitting routine yielded an effective refractive index of $n_{\mathrm{eff,TE}} = 1.67$ and a cavity resonance at $E_0 = 1.1850$ eV. The reflectivity spectrum at $k = 0$ shows a FWHM of 52 meV resulting in a quality factor of 23 for this cavity. The width of the cavity mode equals the photon-damping rate $\hbar\Gamma_{\mathrm{C}}$ and is inversely proportional to the lifetime of the photons between the mirrors. Using transfer-matrix simulations, the angular reflectivity spectra were calculated taking the anisotropic refractive index of the polymer into account.[1] Excellent agreement with the experimental results was achieved for a cavity thickness of 251 nm (Figure 6.2a).

The observed dispersion drastically changed by integrating highly concentrated (6,5) SWCNTs (1.71 wt%) in the cavity. Figure 6.2b displays the angular reflectivity spectra of the nanotube-filled cavity. In contrast to the previous experiment, two modes appeared above and below the exciton: associated with the UP and LP. Further, the dispersion of these modes clearly deviates from that of a pure cavity mode. Instead, an avoided crossing, at angles for which exciton and cavity photons are resonant, is observed. This behavior is evidence of strong light-matter coupling of (6,5) SWCNTs excitons to the surrounding cavity photons. From the recorded dispersions a Rabi splitting, i.e. the minimum energy separation of the LP and UP, of 113 meV was extracted (Figure 6.2c). Due to the small negative detuning of the cavity, the Rabi splitting was found at ±11°. At these angles, the cavity and the exciton are in resonance. Using the complex refractive index of the SWCNT-polymer composite, transfer-matrix simulations were performed. These calculations gave an excellent agreement with the experimental results (Figure 6.2b). In the simulations, the SWCNT concentration as well as the cavity thickness (248 nm) were fitted. The overall similarity of the simulation and experiment corroborate the high quality of the SWCNT layer and suitability of the experimental setup.

[1] Complex refractive indices were determined by Laura Tropf (St Andrews University)

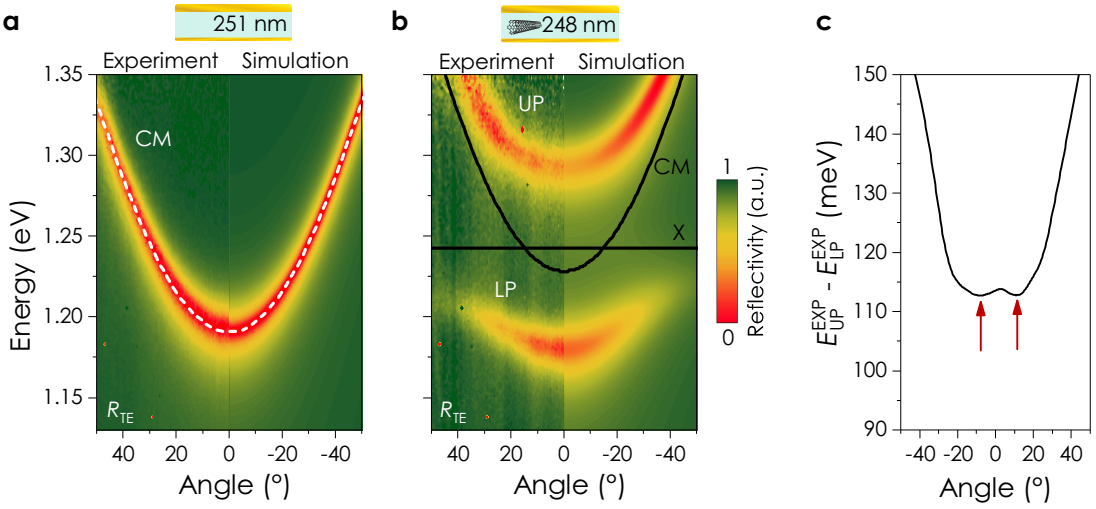

FIGURE 6.2. Strong light-matter coupling in SWCNT-based microcavities.
a, Angle-resolved reflectivity spectra measured in a reference cavity (left) and simulated by transfer matrix simulation (right). b, Angular reflectivity spectra for a SWCNT-filled micro-cavity measured (left) and simulated by transfer matrix simulation (right). c, Energy separation of UP and LP showing two minima at ±11°.

6.3 Coupled oscillator model & polariton emission

The new eigenstates of the hybrid light-matter system can be fully described with the coupled oscillator model (*cf.* Chapter 2.3.2) by independently adjusting the coupling strength and the cavity detuning (Figure 6.3a). For this particular cavity, the fit yielded a Rabi splitting $\hbar\Omega$ of 116 meV and a cavity detuning Δ of –17 meV. These findings are in agreement with the results obtained in the previous section.

Both excitons and cavity photons have a finite lifetime in this system. Hence, light-matter hybridization requires an energy exchange between the exciton and photon that is faster than decoherence of the individual constituents. This condition translates into a minimum Rabi splitting $\hbar\Omega_{min} = 0.5(\hbar\Gamma_X + \hbar\Gamma_C)$ required for strong light-matter coupling. For the uncoupled cavity, a damping constant of 52 meV was determined (*cf.* previous section). The decoherence of the exciton is given by its homogeneous linewidth. Experimentally, this linewidth is found by measuring the fluorescence lifetime τ_{fl} of the excited state which relates to the damping rate by $\hbar\Gamma_X = \hbar{\tau_{fl}}^{-1}$. The fluorescence lifetime, in turn, is the product of the PLQY (~0.1%) and the radiative lifetime (~5 ns, Ref. [36]). Hence, the homogeneous exciton linewidth of the polymer-embedded SWCNTs is approximately 0.1 meV. The minimum Rabi splitting $\hbar\Omega_{min}$ is thus ~27 meV. As the experiments with (6,5) SWCNTs revealed a Rabi splitting of 116 meV, these cavities support sufficiently fast energy exchange and are clearly in the strong coupling regime. Note, depending on its origin, inhomogeneous broadening can lead to a decrease of the exciton

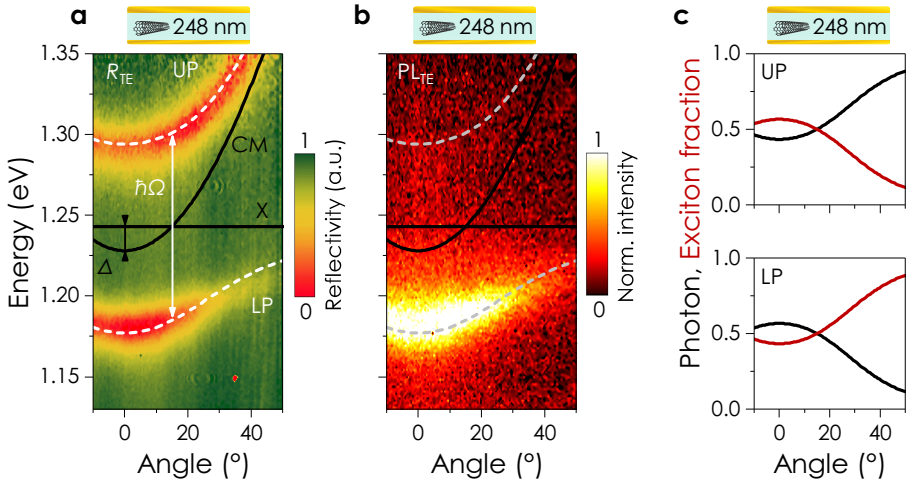

FIGURE 6.3. Exciton-polariton emission and coupled oscillator model.
a, Angular reflectivity of a cavity containing 1.71 wt% of (6,5) SWCNTs with a cavity mode (CM) crossing the exciton (X) shown in black solid lines. The coupled oscillator model was used to fit the dispersion of the UP and LP (white dashed lines). b, Angle-resolved PL spectra of the same cavity with emission from the LP. c, Photonic and excitonic fraction of the upper and lower polariton branch calculated from the coupled oscillator model.

decoherence time.[198] This effect manifests in additional broadening of the polariton modes as observed in the reflectivity spectra. From a practical standpoint, using the average decoherence of the polaritons, $\hbar\Gamma_{LP}$ and $\hbar\Gamma_{UP}$, is thus the necessary condition for strong light matter coupling. In that case, the Rabi splitting must be larger than $0.5(\hbar\Gamma_{LP}+\hbar\Gamma_{UP}) = 38$ meV. This consideration again confirms that the presented cavities were well in the strong light-matter coupling regime.

PL experiments are a versatile tool to study polariton dynamics and investigate their occupation behavior. Any emission that is observed from the polariton branches carries the properties (energy, momentum, phase etc.) of the exciton-polariton. Here, exciton-polaritons were generated by non-resonant optical excitation at 1.937 eV (640 nm). The angle- and spectrally resolved PL that was emitted from the cavity is plotted in Figure 6.3b. The PL signal originates predominantly from the LP and follows its dispersion. Additionally, the significant offset of the emission as compared to the pure exciton and the cavity mode verifies the origin of the emission to be leaking polaritons. The polaritons that are generated upon excitation decay radiatively via their photonic component and are detected by the camera. As no emission from the UP was observed, scattering from the exciton-reservoir into the LP and potentially from the UP into the LP is expected to be efficient. For these cavities, the highest intensity, proportional to the polariton occupation, was detected at the ground state of the LP indicating efficient polariton relaxation.

Within the LP, relaxation of the polaritons towards $k = 0$ occurs by their excitonic component.[121, 122] Further insight into the polariton physics is thus gained by calculat-

ing the photon and exciton fraction of the mixed polariton branches. The fraction of the uncoupled constituents, are derived from the Hopfield coefficients within the coupled oscillator model. These fractions are plotted in Figure 6.4c for the UP and LP. While at large angles the LP is of excitonic character, its photonic fraction increases towards $k = 0$. At the angle of resonance, i.e. $E_X = E_C$, both polariton branches contain 50% exciton and photon fraction. The way the exciton and photon fraction are distributed along the polariton branches directly influences the polariton dynamics as demonstrated in the next section.

6.4 Tuning exciton-polariton properties

To gain further insight into the characteristics of SWCNT-based exciton-polaritons, a set of nanotube-filled microcavities was studied. The light-matter interaction in these cavities varied in terms of coupling strength (related to SWCNT concentration) and cavity detuning (related to the cavity thickness). Both, the strong coupling behavior and the polariton emission were investigated.

For this study, three different concentrations (0.2, 0.46 and 1.71 wt%) of (6,5) SWCNTs were employed. In addition, for each concentration, different cavity thicknesses (240, 245 and 255 nm) were studied. The angular reflectivity and PL spectra for these cavities are plotted in Figure 6.4. While all cavities showed an avoided crossing, the magnitude of the Rabi splitting increased, as expected, for increasing concentration. The exact Rabi splitting and cavity detuning was determined by applying the coupled oscillator model to the measured reflectivity spectra. The model confirms the experimentally measured Rabi splittings of 35, 61 and 112 meV for (6,5) SWCNT concentrations of 0.2, 0.46 and 1.71 wt%, respectively. As the theoretical threshold for strong coupling was found to be 27 meV, all of the investigated cavities were in the strong coupling regime. The smaller concentration of SWCNTs and thus reduced effective oscillator strength resulted in a lower light-matter coupling potential. With regard to the cavity thickness, a red shift of the LP was observed for thicker layers as the cavity mode shifted to longer wavelengths.

Upon optical, non-resonant excitation, all cavities showed exciton-polariton emission. For the highest concentration (1.71 wt%) the PL followed the dispersion of the LP at all cavity thicknesses. Moreover, the highest intensity was observed at $k = 0$ indicating efficient relaxation of the polaritons. In contrast, the emission, observed from cavities with smaller coupling strength, significantly deviated from the LP detected in reflectivity. For large negative detuning and low concentrations, polaritons emitted brightest at angles >20° – a phenomena called polariton relaxation bottleneck. Depending on the excitonic material and the relaxation mechanism, polariton bottlenecks were found to be caused by, for example, inefficient polariton scattering along the LP and energy-dependent radiative pumping of the LP.[121, 122] The origin of polariton bottleneck in these cavities is discussed below.

In general, the appearance of a relaxation bottleneck indicates the absence of an efficient

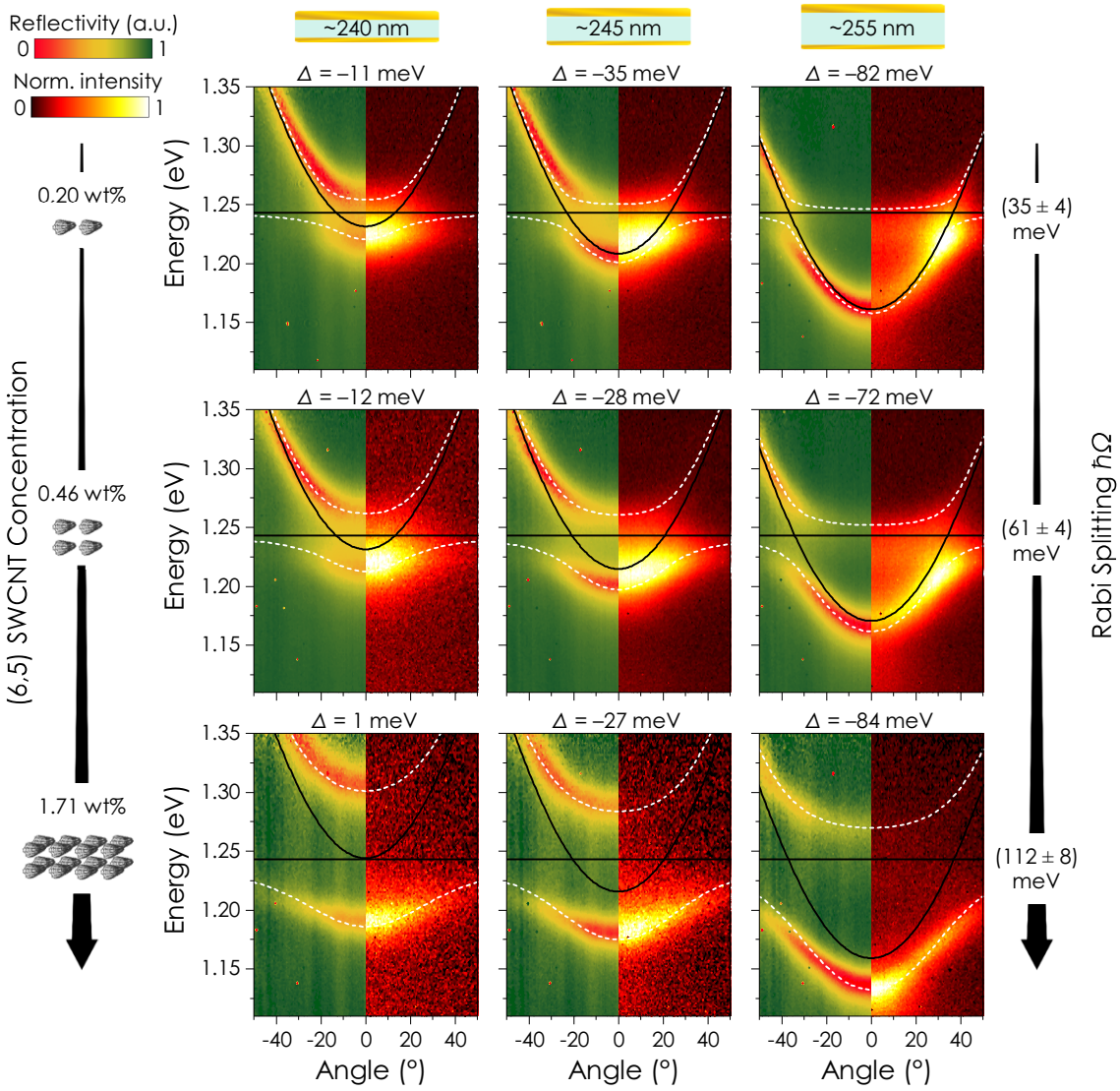

FIGURE 6.4. Concentration- and detuning-dependent polariton properties. Angle- and spectrally resolved reflectivity (red-green color scale) and PL (black-red color scale) for increasing cavity thickness (left to right) and (6,5) SWCNT concentration (top to bottom).

relaxation mechanism for the emissive polaritons. The possible relaxation mechanisms can be divided into radiative and non-radiative relaxation. Radiative relaxation describes the pumping of the LP from the exciton reservoir by radiative decay into the LP branch.[199] In this case, the bottleneck would be most pronounced at peaks of the excitonic PL spectrum. The bottleneck, however, for the cavity with 0.20 wt% SWCNT and –82 meV detuning, was found at ~35°. At this angle the emission peak is red-shifted by 24 meV compared to excitonic emission. Therefore, pure radiative decay from the exciton reservoir can be excluded as a probable cause for the observed

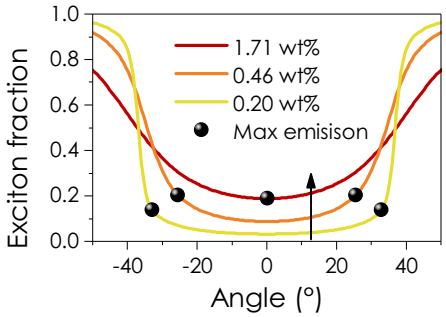

FIGURE 6.5. Impact of exciton fraction on polariton relaxation.
Exciton fraction for the LP branches observed in the right column of Figure 6.4. The black dots indicate the angle at which the maximum PL intensity was detected.

emission pattern.

Non-radiative relaxation, on the other hand, includes scattering of polaritons along the polariton branch. This process requires particle interactions, for example, exciton-exciton, exciton-polariton or polariton-polariton interaction. The efficiency of these processes rely on the excitonic fraction of the polaritons, which changes along the branches. Figure 6.5 shows the exciton fraction of the LP in the cavities with the largest detuning for each concentration (*cf.* Figure 6.4, right column). For each case, the angle at which the highest PL signal was detected is marked. While for 1.71 wt% the exciton fraction stays above 20% even at $k = 0$, this fraction is significantly lower for smaller coupling strengths. Thus, the reduced hybridization in microcavities with smaller Rabi splitting is likely to cause the relaxation bottleneck in these cases. Note, possible relaxation mechanisms and approaches to overcome the bottleneck even at small Rabi splittings are discussed in Chapter 7.5.

6.5 Further discussion

In the literature, strong coupling is sometimes demonstrated by tracking the polariton dispersion against cavity thickness at a given angle.[200, 201] Similar data representation can be obtained from the measurements presented in the previous section. Figure 6.6a plots the spectral position of the polariton branches for a viewing angle of 45° with a resolution ± 0.8°. By plotting the UP and LP versus the cavity thickness, avoided crossing and hence strong light-matter coupling is again observed for the cavity containing 1.71 wt% (6,5) SWCNTs. The data were fitted with transfer-matrix simulations (dashed lines in Figure 6.6a) resulting in a Rabi splitting of 124 meV. These results, based on 13 different cavity thicknesses, are in good agreement with the light-matter coupling found by angle-resolved reflectivity measurements (113 meV).

Fundamentally, the coupling potential and thus the Rabi splitting increases with the square-root the oscillator strength inside the cavity.[104, 138, 202] Here, SWCNT concentration is

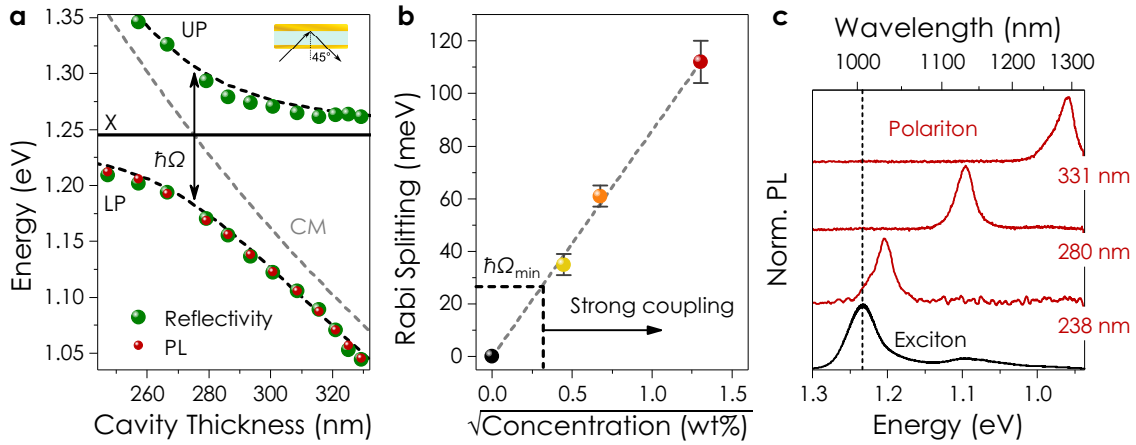

FIGURE 6.6. Summary of detuning- and concentration-dependent polariton properties. a, Polariton branch position plotted against cavity thickness. Green (red) data points are the positions taken from angular reflectivity (PL) spectra. b, Rabi splitting plotted against the square root of the (6,5) SWCNT concentration. c, PL spectra emitted in forward direction for different cavity thicknesses (red) and by the pure exciton (black).

directly linked to the effective oscillator strength in the cavity. Figure 6.6b plots the observed Rabi splitting versus the square root of the SWCNT concentration. The fundamental relation between the coupling strength and oscillator strength is confirmed by the experimental data. Using this relation, a nanotube concentration of 0.11 wt% was identified as the minimum needed to achieve strong coupling, i.e. for a Rabi splitting larger than $\hbar\Omega_{\text{min}} = 27$ meV. Note, by increasing the Q-factor of the cavity, smaller concentrations might be sufficient to maintain strong coupling. At the other extreme, the data can be used to estimate the maximum Rabi splitting achievable with polymer-wrapped SWCNTs. For 100 wt% (6,5) SWNCTs, a Rabi splitting of 850 meV is expected – equal to ~70% of the exciton energy. Further, in-plane alignment of the nanotubes and thus of the transition dipole moments would lead to an additional increase of the coupling strength for one polarization by a factor of two. SWCNTs could thus be used to for ultrastrong light-matter coupling by increasing the nanotube-to-polymer ratio.[103] In this regime, almost dispersion-less emission is expected while the narrow linewidths of microcavities are maintained. The high color-purity and angle-independent emission might offer applications of ultrastrongly coupled SWCNT-cavities for advanced nIR light sources.[145, 203]

The potential application of SWCNTs for telecommunication requires emission beyond 1,000 nm. As described before, SWCNTs could cover this wavelength range by using different chiralities. However, the sorting of the SWCNTs into monochiral samples is still very challenging. Interestingly, the PL observed from the strongly coupled microcavities at normal to the sample surface showed a wide tunability from 1,030–1,300 nm (Figure 6.6c). A narrow line width, attributed to the photon component, of less than 50 meV was maintained across this part of the

spectrum. Thus, these cavities could make tedious SWCNT-selection obsolete.

6.6 Summary & conclusions

In summary, strong-light matter coupling of excitons in (6,5) SWCNTs to planar, metal-clad microcavities was shown at room temperature and in the nIR. The exceptionally high oscillator strength of nanotubes led to a Rabi splitting of 113 meV at SWCNT-concentrations of 1.71 wt% within the cavity. PL experiments revealed efficient polariton relaxation towards the ground state based on the excitonic fraction across the LP branch. At low coupling strength, however, a relaxation bottleneck of the polaritons was observed, which was likely caused by insufficient scattering along the LP. The exciton-polaritons emission was tunable across a wide range of the nIR (1030–1300 nm).

To conclude, SWCNTs were found to be an ideal material for strong light-matter coupling in the nIR and at room temperature. With the techniques, developed over the last decades, SWCNT can be readily produced, purified and easily processed from solution. Applications, such as, polariton lasing, require the implementation of the excitonic material into a high-quality cavity. In this regard, the limitations of the presented cavities might be overcome by replacing the metal mirrors with highly reflective DBRs. For their fabrication, the already developed processes for other organic materials can be utilized.[125] These cavities would increase the exciton-polariton lifetime, which is currently limited by rapid photon decay.

The significant Rabi splitting, achieved at moderate SWCNT concentrations (1.71 wt%), opens the door to advanced application in polaritonic devices. The presented work inspired some intriguing studies on increasing the coupling strength to reach the ultrastrong coupling regime, which was recently accomplished by C. Möhl.[186] The same work demonstrates trion-polariton formation at room-temperature.[186] Moreover, polaritons in aligned SWCNT films were shown to exhibit exceptional points.[204] Finally, a thin layer of concentrated SWCNTs proved sufficient to maintain similar effective oscillator strengths in the cavity and thus supported light-matter hybridization. The next chapter describes on how SWCNTs can be employed for electrically pumped exciton-polaritons.

CHAPTER 7

ELECTRICAL PUMPING & TUNING OF POLARITONS IN SWCNTS

This chapter demonstrates electrical pumping and tuning exciton-polaritons in LEFET-cavities based on SWNCTs. The excellent charge-carrier mobilities of SWCNTs enable the generation of exciton-polaritons at high pumping rates in the strongly coupled cavities. Further, electrical tuning of the oscillator strength facilitates switching between the strong and weak coupling of the SWCNT-based devices.

Part of this chapter was published in Graf *et al.*, Nature Materials 16, 911 (2017).[4] Modified reprints are presented with permission of Springer Nature. This work was carried out in collaboration with Martin Held.

7.1 Introduction

The unique combination of light and matter properties in exciton-polaritons enable the observation of quantum effects, such as Bose-Einstein condensation, at temperatures well above those needed for atomic gases.[205] With the aid of organic materials, researcher have observed BEC,[125] polariton lasing,[108, 117, 126] and superfluidity[127] at room temperature. These results open the door to practical polaritonic devices with electrical generation of polaritons.[135] Ultimately, the reduced thresholds of polariton lasers offer a promising path for electrically driven lasing in organic materials – a long-standing goal of the entire organic electronics community.[206] With respect to practical polaritonic devices, electrical pumping and controlling polaritons in organic materials is, however, particularly challenging.[135] Reaching the required pumping rates, needed for both polariton and conventional lasing comes with demanding requirements for the device architecture and the material properties.

First, the devices must be designed to enable the injection of high current densities without degrading the optical properties of the surrounding cavity. Typically, an OLED-type architecture

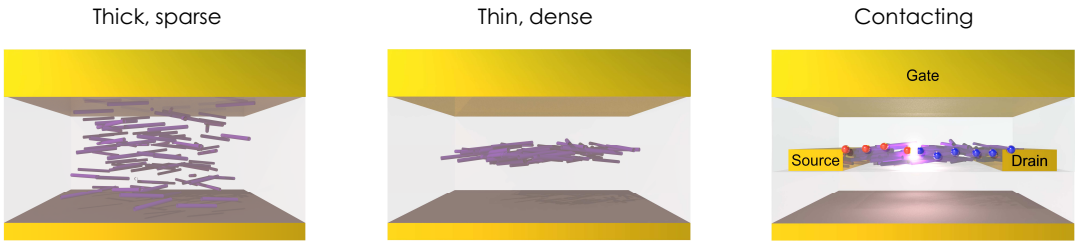

FIGURE 7.1. Device design of a LEFET-cavity.
Strong coupling was shown with polymer-embedded SWCNT microcavities (left). Increasing the nanotube density will allow using a partially filled cavity while maintaining strong coupling (center). Thus additional space inside the cavity can be filled and optimized with a multilayer structure for electrical charge injection, for example a LEFET (right).

is employed in which the electrodes simultaneously act as the cavity mirrors.[140, 144] In these devices, charge carriers are transported in the direction of the cavity mode. Consequently, optimizing the electrical performance has a strong impact on the optical feedback and vice versa. LEFETs, instead, provide a platform in which in-plane current flow is perpendicular to any optical feedback and the charge injecting electrodes and the cavity mirrors are independent from each other. Second, the generation of high current densities requires materials with high charge carrier mobilities and stability under these conditions. Most organic semiconductors, however, have a relatively low charge carrier mobility limiting the current densities that can be achieved. Additionally, the photo and thermal stability of most organic materials is significantly lower than that of inorganic materials leading to rapid degradation and device breakdown at high current densities. Interestingly, SWCNTs exhibit the desirable electronic properties, typically associated with inorganic materials, while maintaining room temperature stability of exciton-polaritons, as observed in organic materials. Semiconducting SWCNTs have an intrinsically high charge-carrier mobility for both electrons and holes even in random networks (up to $100\,\mathrm{cm^2\,V^{-1}\,s^{-1}}$).[48] The excellent ambipolar charge transport leads to high current densities in LEFETs as shown in previous reports.[153, 162]

In the following, SWCNT-based LEFET-cavities are used to electrically pump and tune exciton-polaritons at room temperature. The high charge-carrier mobilities of the employed (6,5) SWCNT networks enable the generation of polaritons at pumping rates ~10^4 times higher than in previous reports using organic semiconductors. Even under continuous pumping, strong light-matter is maintained with minimal efficiency roll-off. Electrically generated polaritons emit purely form the LP and show thermalization because of efficient relaxation towards the ground state. Upon unipolar charging of the SWCNTs, light-matter hybridization is tuned from strong to weak coupling. Finally, the potential of these polaritonic devices for polariton lasing is discussed.

7.2 Cavity-LEFETs based on SWCNT

Electrical generation of exciton-polaritons requires implementing an electronic structure for current injection and transport within an optical cavity. Here, a LEFET structure was integrated that required source, drain and gate electrodes being electrically separated by a dielectric material. Figure 7.1 illustrates how the cavities used in Chapter 6 6 were modified to integrate the necessary structures for current injection while maintaining strong light-matter coupling. Previous experiments employed a thick layer of polymer-embedded SWCNTs at a concentration of 1.71 wt% within the cavity. Similar oscillator strengths across the layer could be achieved with thinner layers for a highly concentrated SWNCT film. By doing so, part of the cavity was used to integrate optically inactive materials, for example, the dielectric materials needed for LEFETs. Additionally, in-plane structuring of interdigitated source and drain electrodes was applied without affecting the optical properties of the cavity in the channel area.

In order to obtain a thin (<50 nm) but highly absorptive film of (6,5) SWCNTs, the excess polymer in the nanotube dispersion was removed. For this purpose, the SWCNTs dispersions were pelletized by ultracentrifugation and the obtained pellets were repeatedly washed with toluene. Asides from polymer chains that were wrapped around the nanotubes, the resulting material contained only very little residual PFO-BPy. The redispersed pellets were then spin-coated onto a low-sodium glass substrate (Schott AF32 Eco). A representative absorption and PL spectra of a 33 nm thick layer are plotted in Figure 7.2a. The film contained a dense network of (6,5) SWCNTs (59 wt%) reaching a peak absorbance of 0.24 at the S_{11}-transition. Likewise, the PL spectrum exhibited excitonic features of (6,5) SWCNTs. As in the previous chapters, a phonon sideband at ~140 meV below the pure exciton emission was observed.[27] In addition to the spectral properties, the PLQY of 0.17% was comparable to those measured for lower nanotube densities in polymer-embedded layers.

Next, the SWCNT networks were incorporated into a LEFET-cavity. Figure 7.2b illustrates the device architecture. The top part of the device comprised a bottom-contact/top-gate LEFET with a thick silver gate and interdigitated gold electrodes (source and drain). Similar to previous work showing excellent electrical performance,[48] a hybrid dielectric (11 nm PMMA and 61 nm HfOx) were used. The optical cavity was completed by processing a LEFET on top of a thin (30 nm) gold mirror (bottom mirror) and an inactive oxide spacer layer.[1] In these devices, the gate electrode of the LEFET acts simultaneously as the top mirror forming an optical cavity with the bottom mirror. Hence, optical confinement was achieved between the gate (top mirror) and the semitransparent bottom mirror. The thickness of the oxide layer was used to adjust the spacing between the mirrors and thus tune the cavity resonance. The thickness of the spacing layer was calculated by a transfer matrix simulation with the aim provide a cavity resonance that overlaps with the exciton energy of the (6,5) SWCNTs. As no current is flowing through

[1] LEFETs were fabricated by Martin Held (Heidelberg University)

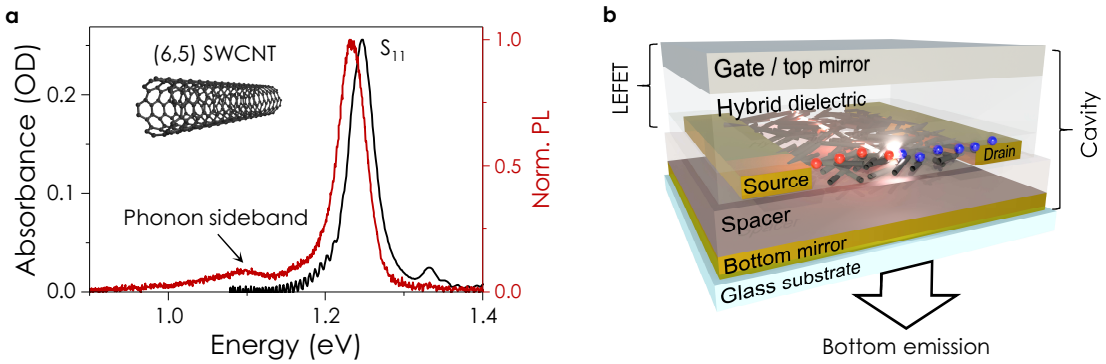

FIGURE 7.2. SWCNTs for cavity-LEFETs.
a, Absorption and PL spectrum of a high-density film of polymer-wrapped (6,5)-SWCNTs. b, Schematic illustration of a cavity-LEFET. The top part is simply a LEFET with lateral cur-rent injection. By adding an oxide spacer layer and bottom mirror, the cavity is formed be-tween the former and the gate electrode.

this layer, the optical properties of the cavity can be easily tuned with minimal impact on the electrical performance of the transistor.

The electrical characterization of such a LEFET-cavity revealed excellent ambipolar charge transport (Figure 7.3a). From this data, a linear electron and hole mobility of 4.2 and 3.5 $cm^2\,V^{-1}\,s^{-1}$, respectively, was determined.[2] The negligible off current at low source-drain bias indicates the very low metallic content in the SWCNT network and enabled on-off ratios of more than 10^6. In comparison to the highest mobilities reported for disordered organic materials, namely conjugated polymers, this relatively thick SWCNT layer exhibited superior transport properties.[207] When driven at high source-drain bias, for example at -8 V, holes and electrons could be injected simultaneously. This property resulted in a characteristic V-shaped transfer curve at these biases. Electron and hole injection and recombination within the channel is expected at gate voltages around the minimum of the curve (V_{min}). In comparison to a reference LEFET without a bottom Au-mirror, no significant difference in electrical performance was observed.

In the regime of ambipolar charge injection, electrons and holes are injected simultaneously leading to the formation of excitons within the channel. Emission from the recombination zone was observed through the semi-transparent bottom mirror. Representative images of the EL emitted from the cavity-LEFET are shown in Figure 7.3b. The recombination and hence emission zone can be shifted by changing the applied gate voltage from source to drain electrode. Note, for constant biases, the position in the channel is fixed. The width of the emission zone, averaged across the channel, was found to be ~1 µm. As introduced in Chapter 2.2.2, even at high current densities the number of accumulated charges is at its minimum in the recombination zone preventing

[2]LEFETs were characterized by Martin Held (Heidelberg University)

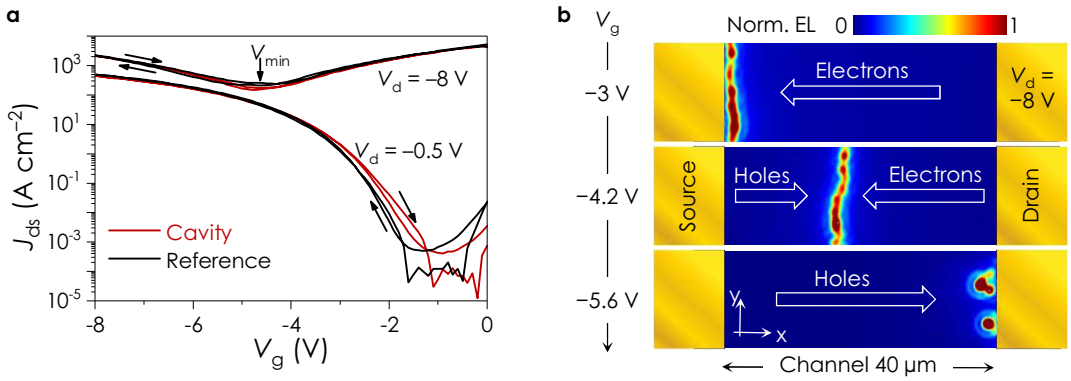

FIGURE 7.3. Electrical characteristics of and EL from cavity-LEFETs.
a, Transfer characteristics of cavity-LEFET. b, Real space images of the emission zone within the channel at constant drain voltage (V_d) and different gate voltages (V_g).

significant quenching. In the next section, the properties of the EL signal are characterized by angle-resolved spectroscopy.

7.3 Electrically pumped exciton-polaritons

As in the previous chapter, the light-matter coupling within the channel region of the cavity-LEFETs was characterized by angle-resolved reflectivity spectroscopy (Figure 7.4a). The momentum space image revealed the formation of an UP and LP above and below the exciton energy with a dispersion clearly deviating from both exciton and cavity mode. A minimum energy separation of the polariton branches, associated to the Rabi splitting, of 125 meV was observed at 34°. Fitting these modes with the coupled oscillator model yielded a Rabi splitting $\hbar\Omega$ of 127 meV, a cavity detuning Δ of –62 meV and a refractive index $n_{\mathrm{eff,TE}}$ for TE-polarized light of 1.96. These results were in agreement with the experimentally determined Rabi splitting. In addition, the effective refractive index was expected to be higher than in the cavities of the previous chapter as materials with higher refractive index were incorporated in the cavities. The homogeneous exciton decay rate $\hbar\Gamma_{\mathrm{X}}$ of 0.1 meV and the cavity mode $\hbar\Gamma_{\mathrm{C}}$ of 44 meV resulted in a minimum Rabi splitting $\hbar\Omega_{\mathrm{min}}$ of 23 meV required for strong coupling (*cf.* Chapter 2.3.2). Hence, the LEFET-cavities, exhibiting a Rabi splitting of 127 meV, were clearly in the strong coupling regime. Upon off-resonant optical excitation at 1.937 eV (640 nm), PL from the LP was observed (Figure 7.4b). In agreement with the observations in the previous chapter on negatively detuned cavities with Rabi splittings of >100 meV, no relaxation bottleneck was found for this cavity.

Next, the LEFET-cavities were electrically contacted and operated in the ambipolar regime. Applying a gate voltage of –5.1 V and a source-drain bias of –10 V, the angle and spectrally resolved EL was measured with a Fourier imaging setup (Figure 7.4c). The EL was found to

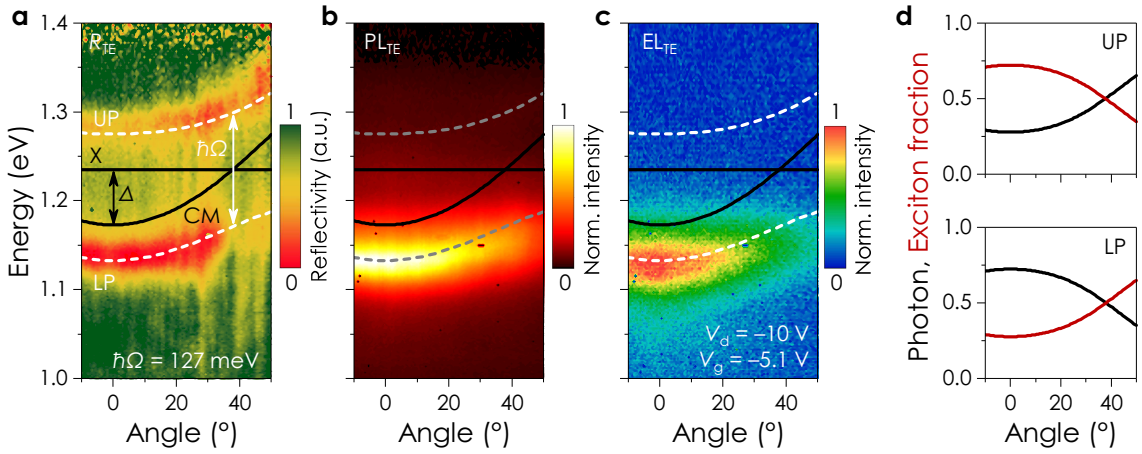

FIGURE 7.4. Exciton-polaritons in SWCNT-based cavity-LEFETs.
a, Angle-resolved reflectivity spectra for a LEFET-cavity containing a dense (6,5) SWCNT layer (59 wt%). b, Angular PL spectra from the same cavity for off-resonant excitation at 1.937 eV (640 nm). c, Angle- and spectrally resolved EL emitted from the same device under ambipolar operation. d, Photon and exciton fraction for the LP and UP branch.

originate solely form the LP following the dispersion observed in reflectivity experiments. In this experiment, electrical pumping of exciton-polaritons was achieved at a constant current density J_{ds} of 600 A cm^{-2}. The brightest emission was observed at the polariton ground state with a steep decrease of intensity towards larger angles. Overall, 50% of the outcoupled intensity was detected within a 20° cone.

The light-matter hybridization is visualized by calculating the photon and exciton fraction of the polariton modes (Figure 7.4d). Significant admixing of excitons and photons was found across all investigated angles. In particular, the exciton-fraction of the LP stayed above 25% even at $k = 0$. As observed in the previous chapter, the high exciton fraction favors efficient relaxation towards the ground state. In more detail, thermalization of the polaritons in the LP was found for the electrically pumped polaritons (more details on polariton relaxation follow in section 7.5). In comparison to PL, no linewidth broadening of EL was observed. The impact of emission from a confined area (~1 µm for EL) leading to emission into an angular range of ~9° has thus no significant effect on the measurements.

7.4 Emission efficiency & wavelength tuning

To quantify the scattering efficiency into the LP and estimate the efficiency of polariton generation, the EQE of the strongly coupled LEFET was determined. In addition to insights into the polariton physics, the EQE provides a universal measure for benchmarking. In Figure 7.5a, the external efficiency of the strongly coupled LEFET-cavity and a reference LEFET is plotted. The maximum

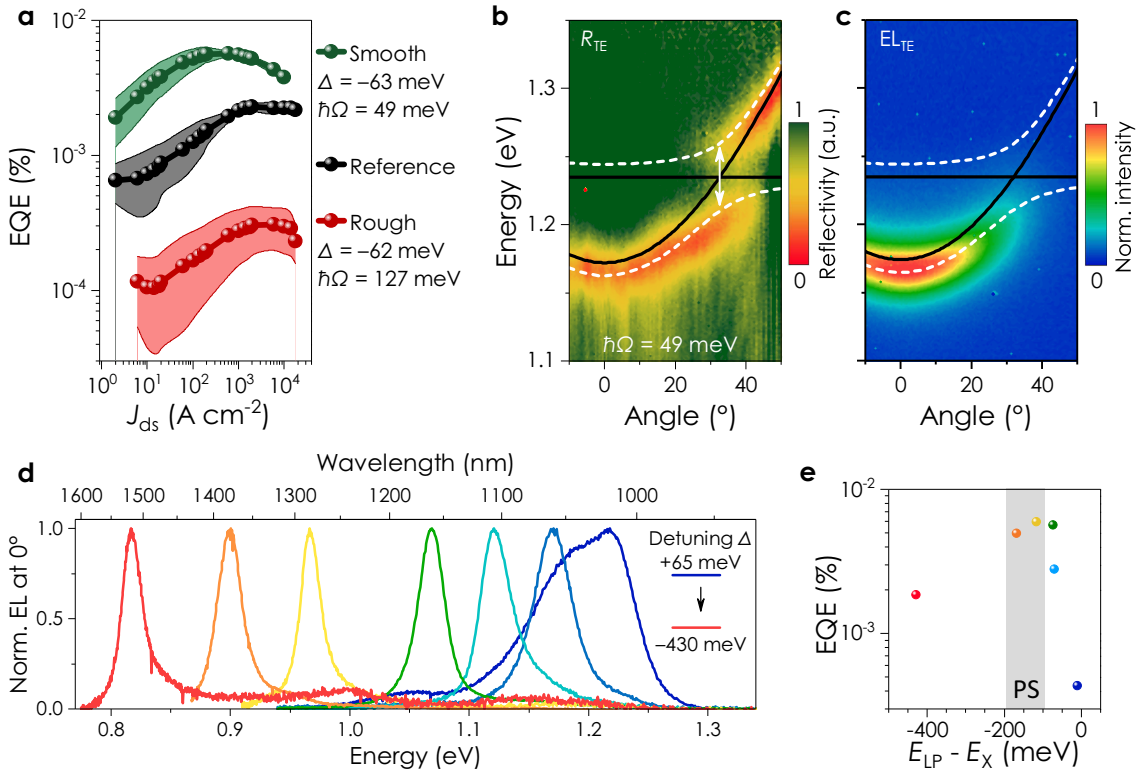

FIGURE 7.5. LEFET-cavity EQE and optimization.
a, EQE of the LEFET-cavities and a reference LEFET. b, Angular reflectivity spectra in the channel area of a cavity-LEFET with smooth SWCNT layer. c, Angle and spectrally resolved EL emitted from this device. d, EL spectra emitted at $k = 0$ for different strongly coupled LEFET-cavities of varying detunings. e, EQE versus cavity detuning.

EQE of the polariton emission is almost seven times lower than for the reference device. This reduction is attributed to the substantial surface roughness (RMS, 21.4 nm) and inhomogeneity (thickness, 33±8 nm) of the SWCNT layer in the cavity. Light scattering at the interfaces and within the SWCNT layer reduces the quality of the optical cavity and thus the polariton lifetime.

In a second generation of devices, a LEFET-cavity containing a smoother (RMS, 4.1 nm) and more homogeneous (thickness, 19±3 nm) film of (6,5)-SWCNTs was fabricated. Angular reflectivity spectra and the fit to the coupled oscillator model revealed strong light-matter coupling in these devices with the less absorptive SWCNT layer (Figure 7.5b). Both experimental data and the fit to the coupled oscillator model gave a Rabi splitting $\hbar\Omega$ of 48 meV. Additionally, the coupled oscillator model yielded a cavity detuning of Δ of –63 meV for a refractive index $n_{\mathrm{eff,TE}}$ of 1.96. The smaller Rabi splitting, in comparison to the previous device generation, originated in the thinner and less concentrated SWCNT layer (39 wt%). Electrical excitation of the polaritons led to EL from the LP with efficient relaxation towards $k = 0$ (Figure 7.5c). While the electrical

characteristics of the device were similar to those of the first generation, the optimized device exhibited an improved EQE (Figure 7.5a). Moreover, the strongly coupled cavities were even more efficient than the reference LEFET. The LP linewidth of the improved LEFET-cavities showed a smaller linewidth and thus longer lifetime of the LP, which enhances the probability of relaxation towards small angles. The improvements are thus attributed to an improved scattering into the LP from the generated exciton-reservoir.

Further insight into the involved relaxation mechanisms was gained by varying the cavity thickness in these devices and hence altering the detuning of the cavity resonance with respect to the exciton energy. Multiple devices with detunings ranging from +65 meV to –430 meV were fabricated. All LEFET-cavities showed strong light-matter coupling and ambipolar electrical performance. The EL spectrum, emitted in forward direction, is shown in Figure 7.5d. These data indicate the wide spectral tunability that is achievable for exciton-polaritons. Polariton-relaxation in the devices enabled emission to up to 1,530 nm. The device efficiency (EQE), however, strongly depends on the detuning (Figure 7.5e). The highest EQE is observed for a LEFET-cavity in which the minimum of the LP overlaps with the phonon-sideband of the S_{11}-exciton. As observed for other organic materials,[208] the dependence on the detuning suggest the presence of direct scattering from the exciton-reservoir into the LP with the aid of a D-phonon. This process appears to be efficient in SWCNT-based exciton-polaritons. Additional relaxation mechanisms are discussed and experimentally investigated in the following section.

7.5 Polariton relaxation

The formation of a polariton condensate requires the accumulation of large numbers of polaritons at $k = 0$ (*cf.* Chapter 2.3.3). In addition to higher pumping rates, a faster relaxation increases the ground state occupancy. The polariton population within the LP is a direct measure of the relaxation efficiency. As the emitted photons carry the properties of the polaritons inside the cavity, the leaked intensity is proportional to the polariton density multiplied by the photon fraction at a given wavevector.[116] The polariton population along the LP in the LEFET-cavity, for electrical pumping, is plotted in Figure 7.6 on a logarithmic scale. The polaritons show a Boltzmann-like distribution in the LP (thermalization of the polaritons in the ground state) indicating efficient relaxation towards the ground state and excluding any form of relaxation bottleneck.[117]

As shown in the previous section, the detuning-dependent EQE suggests a phonon-assisted scattering from the exciton reservoir into the LP. To gain further insights into the relaxation mechanisms of SWCNT-based polaritons within the LP, the results of LEFET-cavities are compared to those of polymer-embedded SWCNTs investigated in Chapter 6. While the LEFET-cavity employs a thin (19 nm) and dense layer of SWCNTs (59 wt%), the cavity investigate in the previous chapter consists of a thicker (250 nm) and sparse SWCNT network (0.46 wt%). The

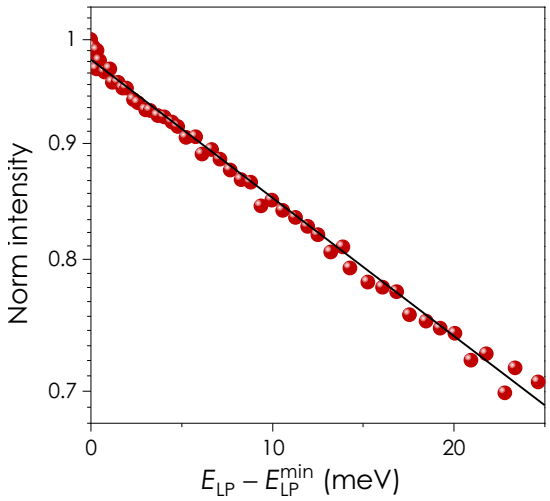

FIGURE 7.6. Polariton population of the LP in LEFET-cavities.
Normalized polariton-population along the LP upon electrical excitation. The normalized in-tensity is plotted on a logarithmic scale.

polariton dispersions of both cavities are almost identical (Figure 7.7a) due to the similar coupling strength and refractive index. Hence, the exciton and photon fraction in the polariton branches are almost identical as well. In contrast to the similarities in light-matter coupling, the angle-resolved PL spectra and thus polariton distribution reveal significant differences (Figure 7.7b). While the LEFET-cavity supports excellent relaxation towards the ground state, the cavity filled with polymer-embedded SWCNTs exhibits a relaxation bottleneck. The improved relaxation for polaritons based on a dense SWCNT-network might be attributed to increased non-radiative intertube relaxation.[162] Intertube interactions are strongly dependent on the distance between the nanotubes and are thus enhanced in these layers. These interactions might enhance intraband relaxation via the excitonic part leading to polariton interactions, such as polariton-polariton, polariton-exciton or polariton-electron interaction.[127, 209, 210] Further studies on, for example, temperature-dependent relaxation efficiency will be necessary to proof this hypothesis.

7.6 High current densities

In addition to efficient relaxation, the polariton density can be increased by higher pumping rates. The angle-resolved EL spectra recorded for low and high current densities are plotted in Figure 7.8a. For the investigated currents, the EL emitted by the strongly coupled cavities originates solely from the LP and follows its dispersion. In this device up to 18,600 A cm^{-2} were applied for continuous pumping. The high current densities are a result of the excellent charge-carrier mobilities of SWCNTs. At the same time, even at continuous operation, the SWCNTs

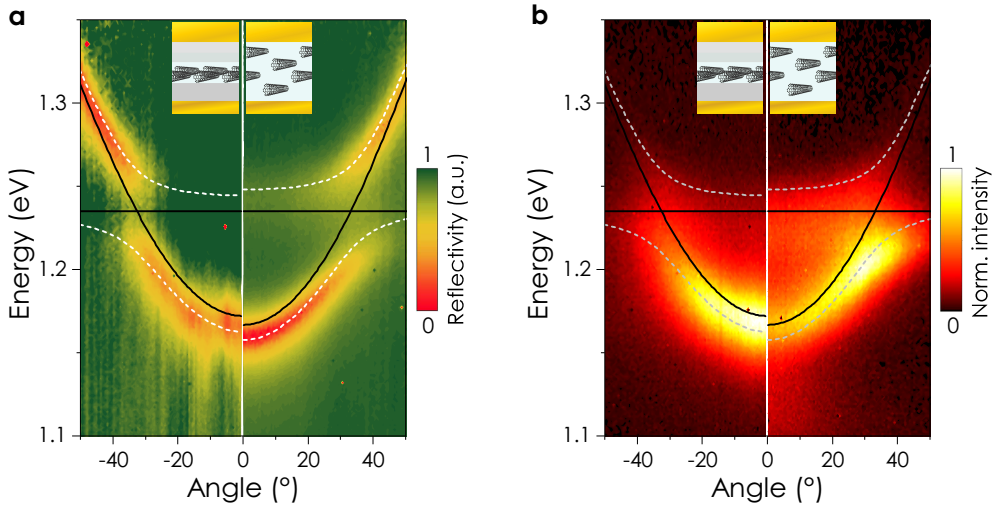

FIGURE 7.7. Polariton relaxation in SWCNT-based microcavities.
a, Comparison of angle-resolved reflectivity spectra and b, PL spectra for a high density but thin film of SWCNTs (left) and a thick but less dense film of SWCNTs in a metal-clad microcavity.

can withstand these currents owing to their excellent thermal conductivity of ~3,000 $\mathrm{W\,m^{-1}\,K^{-1}}$ reported in literature.[8]

At such high pumping rates, the strong coupling could be lost due to bleaching of the absorption by free charges accumulating in the excitonic material. While this can be used to tune the light-matter coupling (*cf.* Chapter 7.8), it is unwanted for generating high densities of polaritons. In case of the investigated device, the Rabi splitting was recorded during the measurements. The reflectivity at resonance, i.e. the angle at which $E_\mathrm{X} = E_\mathrm{C}$, is shown in Figure 7.8b. A reduction from 49 meV to 42 meV was found between low and high current densities. Hence, the strong coupling (minimum Rabi splitting 23 meV) was maintained even at these extreme current densities. Again, this is attributed to the high charge-carrier mobilities of SWNCTs minimizing the accumulated free charges at a given current density. Additionally, the carrier density is at its minimum in the recombination and emission zone thus minimizing any ground state bleaching.

In contrast to previous reports on polariton condensates,[108, 109, 211] no non-linearity in the output versus pumping rate occurred and no spectral narrowing was observed. Thus, the generated polariton density in these devices did not exceed the threshold for polariton condensation. It is important to benchmark these results to other polaritonic devices. While the current density is an appropriate quantity to compare different LEFETs, it cannot be used for comparison to other device architectures, such as LED-cavities. A generally applicable method to evaluate and compare the pumping rates in different system is to consider the volumetric exciton-pumping rate, i.e. the number of generated excitons per volume per time.

The exciton pump rate is calculated by considering the injected current (charges per second)

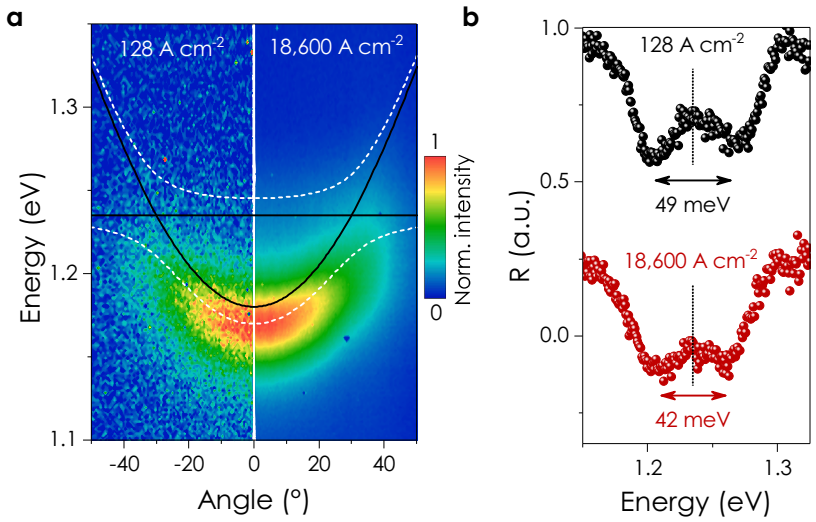

FIGURE 7.8. LEFET-cavities at high pumping rates.
a, comparison of angular EL spectra for low (left) and high current density (right). b, Reflectivity spectra at k for which exciton and cavity are resonant (29°) for low (top) and high (bot-tom) current density.

and the recombination volume in which these charges recombine. For the presented LEFET-cavities, electrically pumped exciton-polaritons were measured at a maximum source-drain current of 9.3 mA. Note, within the resolution limit, no gate leakage current was detected and thus all injected charges will eventually recombine and pump the exciton reservoir. The size of the recombination volume can be estimated from different observations. First, the emission zone width was measured to be ~1 µm (*cf.* Figure 7.3b). This result is in agreement with previous reports on light generation within LEFETs.[212] Second, the length of the emission zone, i.e. parallel to the source/drain-electrodes, is given by the 10 mm long electrodes. Lastly, the depth of the recombination zone can be estimated from the reduced Rabi splitting at high current densities. As shown in the previous section the Rabi splitting reduced from 49 meV to 42 meV. The Rabi splitting in turn has a square root dependence on the number of coupled oscillators in the layer. Thus around 5 nm of the layer were charged at high pumping rates determining the volume for initial exciton formation. These observations lead to an estimated exciton pumping rate of ~$10^27\,\mathrm{cm}^{-3}\,\mathrm{s}^{-1}$ in the presented LEFET-cavities based on (6,5) SWCNTs. In comparison to previous work on electrically pumped polaritons in OLEDs,[140, 143, 144] these pumping rates are ~10^4 times higher. In the next section, the polariton density achieved at these pumping rates is calculated. Further, the ground state occupation of the polaritons is estimated and necessary steps towards polariton lasing are analyzed.

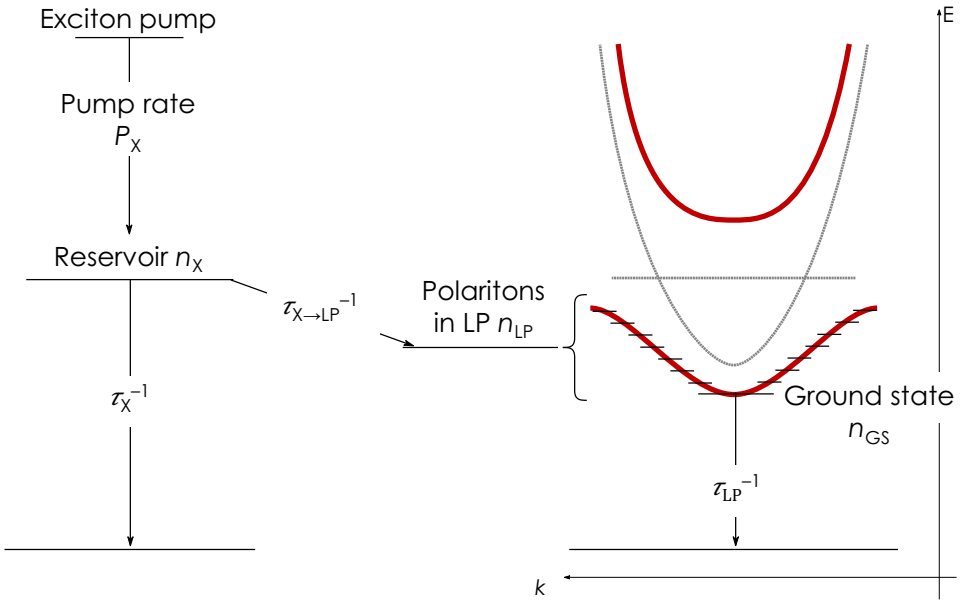

FIGURE 7.9. Illustration of polariton pumping scheme.
An external source – here electrical – pumps at rate P_X an exciton reservoir in which n_X excitons accumulate. The reservoir is depleted by either exciton decay at ${\tau_X}^{-1}$ or scatters into the LP with a rate ${\tau_{X\to LP}}^{-1}$ pumping the LP. Of all polaritons in the LP n_{LP} will be n_{GS} in the ground state at $k = 0$ which decay at ${\tau_{GS}}^{-1}$

.

7.7 Polariton density & ground state occupation

In order to evaluate how close the presented LEFET-cavities based on SWCNTs were to electrically driven polariton lasing, the polariton density and the ground state occupation is calculated. As shown in the previous section, the exciton reservoir in this system was pumped at a rate P_X of ~$10^27\,\mathrm{cm}^{-3}\,\mathrm{s}^{-1}$. The pumping resulted in a number of excitons within the reservoir n_X, which in turn was depleted by exciton decay ${\tau_X}^{-1}$ or scattering into the LP at a scattering rate ${\tau_{X\to LP}}^{-1}$ (Figure 7.9). The number of excitons in the reservoir is then described by the rate equation

$$\frac{\mathrm{d}n_X}{\mathrm{d}t} = \eta\, P_X - \frac{n_X}{\tau_{X\to LP}} - \frac{n_X}{\tau_X}. \tag{7.1}$$

Here, η accounts for the efficiency of exciton emission for electrical pumping with respect to reference sample (PLQY, 0.3%). For the LEFET-cavities, η equals 0.01 describing the ratio of EQE to PLQY at high current densities.

At the same time, the LP branch was pumped by scattering from the exciton reservoir into the LP. The number of polaritons in the LP n_{LP} is then given by

$$\frac{\mathrm{d}n_{LP}}{\mathrm{d}t} = \frac{n_X}{\tau_{X\to LP}} - \frac{n_{LP}}{\tau_{LP}}, \tag{7.2}$$

where the lifetime of the LP, τ_{LP}, is introduced. The polariton is composed of its photonic component α and excitonic fraction β. The lifetime of the polariton is then calculated as:

$$\frac{1}{\tau_{\mathrm{LP}}} = \frac{\alpha}{\tau_{\mathrm{C}}} + \frac{\beta}{\tau_{\mathrm{X}}}, \tag{7.3}$$

with τ_{C} being the cavity lifetime.

Assuming quasi-steady state allows us to derive the polariton density from Equation (7.1) and (7.2):

$$n_{\mathrm{LP}} = \frac{\eta\, P_{\mathrm{X}}}{\tau_{\mathrm{X}\to\mathrm{LP}}} \left(\frac{\alpha}{\tau_{\mathrm{C}}} + \frac{\beta}{\tau_{\mathrm{X}}}\right)^{-1} \left(\frac{1}{\tau_{\mathrm{X}\to\mathrm{LP}}} + \frac{1}{\tau_{\mathrm{X}}}\right)^{-1}. \tag{7.4}$$

In case of the LEFET-cavities presented here, a maximum polariton density of ~$3.6\dot{1}0^{11}\,\mathrm{cm}^{-3}$ was achieved.

Polariton lasing is associated with a ground state occupancy larger than one in which case the scattering into the ground state becomes a stimulated process. The mean ground state occupancy $\langle n_{k=0}\rangle$ is thus a measure to evaluate how close a system is to polariton condensation. In order to calculate the ground state occupancy the total number of ground state polaritons within an emission site $N_{k=0}$ and the number of states M is needed. Next, a single emission site with a 1 µm diameter D and a 5 nm depth w is considered. The number of polaritons N_{LP} present in this area can be calculated by

$$N_{\mathrm{LP}} = n_{\mathrm{LP}}\; w\; \pi\; D^2/4. \tag{7.5}$$

Next, the fraction of these polaritons, which are in the ground state, is calculated from the population along the LP. The total number of polaritons is proportional to the integrated photon-fraction-corrected intensity of the LP. The fraction in the ground state, which is emitted into ±1° (angular resolution limit), is calculated to be 0.03 of the total detected signal in Fourier imaging. This leads to the number of polaritons within the ground state to be

$$N_{k=0} = 0.03^2\; N_{\mathrm{LP}}, \tag{7.6}$$

which is equivalent to the fraction of polaritons within an angular cone of ±1°. The number of states that is present in the observed spot is given by:

$$M = \frac{1}{2}\; \frac{\pi D^2/4}{4\pi^2}\; \pi\big(k_0 \Delta\theta\big)^2 \tag{7.7}$$

with k_0 being the wave number of the emitted light and $\Delta\theta = 0.0175$ the detection half angle. Finally, the mean ground state occupancy is calculated by:

$$\langle n_{k=0}\rangle = \frac{N_{k=0}}{M}. \tag{7.8}$$

In the presented metal-clad LEFET-cavities, a ground state occupancy of 0.004 was reached at maximum current density, which was 250 times below threshold for polariton condensation. Possible strategies for increasing the polariton density as well as physical boundaries are discussed in the following subsection.

7.7.1 Toward polariton lasing & non-linear interactions

The polariton density of ~$3.6{\cdot}10^{11}$ cm^{-3} was shown to correspond to a ground state occupancy of 0.004. In previous reports on organic materials, polariton densities on the order of ~10^{13} cm^{-3} were needed to reach polariton lasing in the thermodynamic limit.[108] These cavities comprised a 120 nm thick layer that was optically pumped across the entire layer. In cavity-LEFETs, in which a 5 nm thick layer is electrically pumped, polariton lasing would be present at a polariton density of ~10^{14} cm^{-3}. In terms of polariton density, the presented LEFET-cavities were thus ~270 times below the densities needed for optical pumping of polariton condensates. This estimate is in agreement with the calculations of the ground state occupancy (~250 times below the polariton lasing threshold).

In the investigated LEFET-cavities, the accumulated polariton density was mainly limited by the short polariton lifetime of 31 fs, which was limited by the photon lifetime of 16 fs. The fast decay of the photons is a direct result of the cavity's low quality factor of 28. Replacing the metal mirrors by highly reflective DBR mirrors would significantly increase the photon lifetime within the cavity. In general, replacing the metal mirrors in a LEFET-cavity is less challenging than in an OLED-cavity as the optical feedback is decoupled from the electrical current injection. In case of LEFET-cavities, the bottom mirror can be easily replaced by a DBR reflector, as it is electrically inactive. Exchanging the top metal-mirror and gate electrode could be achieved, for example, by a split-gate device structure resulting in an emission zone that can be tuned towards a metal-free area. In this configuration, typical quality factors of DBR-clad cavities of 1,000 are readily achievable. The enhanced photon lifetime in such a high quality cavity would boost the polariton density in the LEFET-cavities to ~$1.3{\cdot}10^{13}$ cm^{-3} for identical pumping rates. In this case, the ground state occupancy would increase significantly to 0.15. Further, the electrical performance of the LEFET can be optimized to increase the pumping rate. Among possible strategies are aligned SWCNTs,[213] double-gated device structures,[214] and patterning of the SWCNT network for current focusing within the channel area. With the aid of these concepts, the exciton pump rate could be readily increased by two orders of magnitude. Thus, achieving a polariton density above ~10^{14} cm^{-3}, as required for polariton lasing, is feasible in LEFET-cavities.

Nonlinear interaction in polariton condensates result in a rich set of phenomena, for example, superfluidity.[97, 127] These interactions originate from the excitonic nature of the polaritons occurring between spatially overlapping polaritons. At the same time, high densities of excitons in the material can lead to ground state bleaching and transparency of the material. In the following, these aspects are evaluated for SWCNTs. Excitons in SWCNTs were shown to exhibit a Bohr radius a_B of ~10 nm leading to a Mott density of ~10^{18} cm^{-3} at which the oscillator strength of the nanotubes would be bleached.[32] Exciton-exciton interaction in SWCNTs was, however, shown to be present at densities of ~10^{15} cm^{-3} – well below the Mott-density.[215] The increased interactions in SWCNTs are explained by the long exciton diffusion length. Since such densities were not reached in the devices, nonlinear interactions were not observed in the

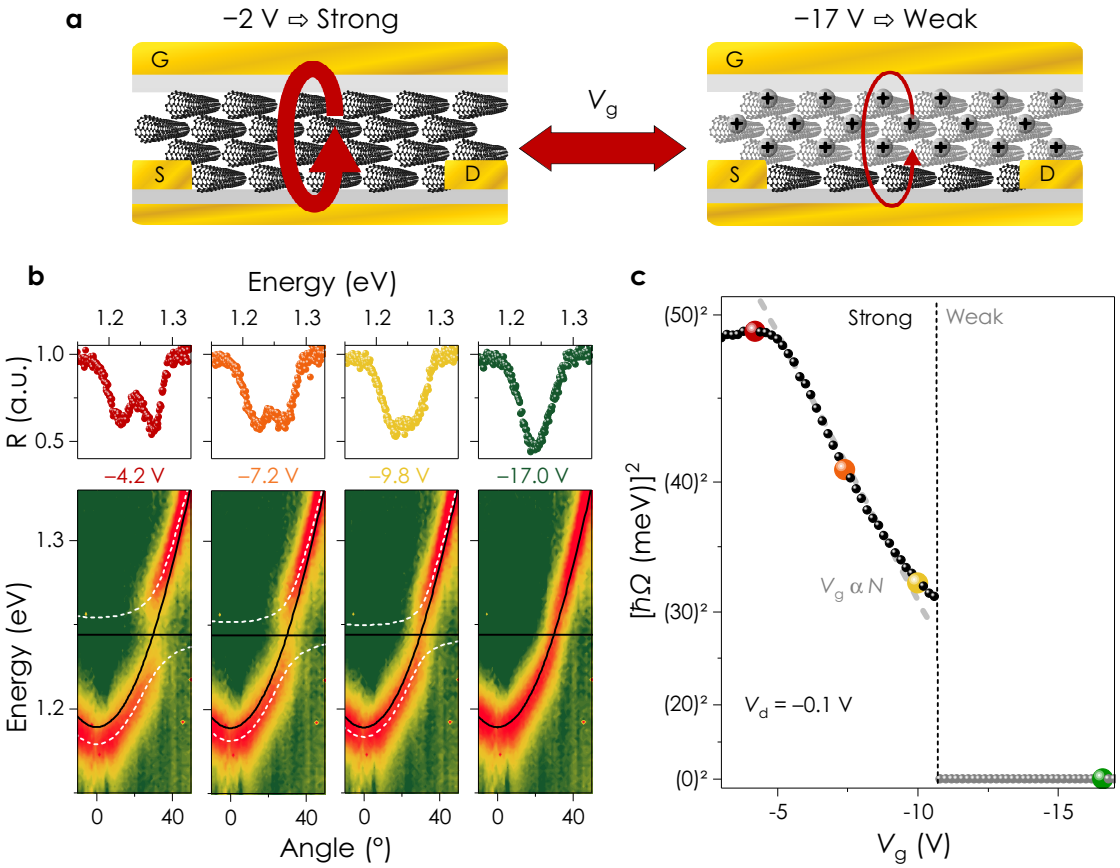

FIGURE 7.10. Electrically tuning light-matter coupling.
a, Illustration of the oscillator strength tuning by charge accumulation in cavity-LEFETs. At low applied voltage the full oscillator strength of SWCNTs leads to strong light-matter coupling while at high voltages the oscillator strength is reduced resulting in weak coupling. b, Angular reflectivity spectra (bottom row) for different applied gate voltages in the channel region of a cavity-LEFET. Reflectivity spectra at k for which exciton and cavity are resonant (top) for the same gate voltages. c, experimentally observed Rabi splitting plotted against gate voltage.

presented LEFET-cavities. As shown above, in more advanced devices densities of $>10^{14}$ cm^{-3} could be achieved for which nonlinear interactions are likely to occur. All these densities are well below the Mott density highlighting the suitability of SWCNT-based exciton-polaritons for polariton lasing and nonlinear interactions.

7.8 Electrically tuned light-matter interaction

So far, the LEFET-cavities were operated in the ambipolar regime for electrical excitation, i.e., gate and source-drain voltages were chosen to inject electrons and holes into the SWCNT layer. In this operation mode, relatively high source-drain biases are used. In the ambipolar regime, the

light-matter interaction was almost unaffected even at high current densities (*cf.* Figure 7.8). In this section, the LEFET-cavities are investigated in the unipolar regime – at very low source-drain bias and variable gate voltage and thus carrier density in the channel – and can be used to tune the light-matter coupling from the strong to the weak regime as illustrated in Figure 7.10a.

Accumulation of free charges in the SWCNTs bleaches the ground state and consequently reduces the oscillator strength of the S_{11}-tranistion.[153] Consequently, significant charge accumulation should result in a change of the coupling strength within the LEFET-cavities. Figure 7.10b shows the angle-resolved reflectivity spectra for increasing gate voltage and thus charge accumulation at low source-drain bias. While for low gate voltages (–4.2 V) the Rabi splitting remained constant at 49 meV, the energy separation was reduced by further charge accumulation. At larger gate bias (–17 V) no avoided crossing of the cavity and exciton was observed anymore. In this case, the reduced oscillator strength of the excitonic transition resulted in a weakly coupled cavity. The reduction in Rabi splitting can be further visualized in the reflectivity spectrum at resonant angle (29°) in the top part of Figure 7.10b. Again, the energetic separation of the UP and LP shrank with increasing gate voltage until only a single mode was observed for large gate voltages.

In Figure 7.10c, the measured Rabi splitting is plotted against the applied gate voltage. The data indicates that below a certain threshold, the charge density scales linearly with the gate voltages. In that regime, the Rabi splitting is proportional to the square root of the gate voltage (dashed line in Figure 7.10c). Overall, the coupling strength was continuously tuned by up to 15 meV. At a certain voltage (–10.6 V), no splitting could be observed anymore and the weak coupling regime was entered. After turning off the gate voltage, the coupling strength of 49 meV was recovered. The LEFET-cavities could thus be repetitively switched between the strong and weak coupling regime and could be tuned to any light-matter coupling in between.

7.9 Summary & conclusions

In this chapter, LEFET-cavities based on SWCNTs were used for electrical pumping of exciton polaritons at room temperature and in the nIR. The devices supported high current densities of >10 kA cm^{-2} leading to exciton-polariton pumping rates ~10^4 times higher than previously reported for organic materials. At these pumping rates, strong coupling and efficient polariton-relaxation towards the ground state was maintained. Calculations of the polariton density in the channel area revealed that in these devices the ground state occupancy reached 0.004. Furthermore, in the unipolar regime, the LEFET-cavities were shown to facilitate controlled tuning of the light-matter interaction and reversibly switching between strong and weak coupling.

These results present a promising step towards electrically pumped polariton lasing at room temperature. Following the ideas described in Chapter 7.7.11, technologically feasible steps are presented to accomplish polariton condensation. In particular, increasing the polariton

lifetime and the pumping rate promise to increase the polariton density significantly in next generation of LEFET-cavities. Further, the experiments on different cavity thicknesses highlight the fundamental advantages of a LEFET-cavity – the decoupling of the charge injection and the cavity mirrors. In addition, the spatial confinement of the recombination zone in LEFETs might be advantageous to accumulate larger densities of polaritons. Due to the charges present in the vicinity of the recombination zone, polariton diffusion might be prevented supporting higher polariton densities.[216] In these devices, no significant difference on charge carrier mobility between the strongly coupled LEFET-cavity and a reference LEFET was observed. Whether these results contradict the results observed in the group of Ebbesen, which demonstrated an enhanced charge-carrier mobility in plasmonic polaritons, needs to be elaborated in further studies.[217]

In analogy to optically pumped SWCNT-based polaritons, the emission wavelength of the cavities was widely tuned from 1,030 nm up to 1,530 nm. Embedding SWCNT in strongly coupled cavities might thus make the tedious selection process of other chiralities obsolete. Additionally, the wide tunability suggest efficient relaxation mechanisms for polaritons based on SWCNTs. Overall, strongly coupled LEFET-cavities present a new platform for practical polariton devices that can be employed for various materials as well as electrically pumped polariton lasing.

CHAPTER 8

CONCLUSIONS & OUTLOOK

This chapter draws conclusions from the results and insights presented in this thesis. Finally, an outlook on potential future research, based on these findings and related work, is given.

In this thesis, the intriguing properties of SWCNTs were employed for studying fundamental physics and for developing advanced optoelectronic devices. At the outset of this thesis in 2014, selecting monochiral SWCNTs at large scale was a time-consuming task and the behavior of nanotubes in microcavities was largely unexplored. This thesis demonstrated a method to obtain large amounts of monochiral (6,5) nanotubes and used those to shed light on the underlying physics and presented a proof-of-concept of various optoelectronic applications of SWCNTs. The characteristics of the developed devices highlight the advantageous properties of SWCNTs but reveal, at the same time, major limitations that need to be tackled in future research. These obstacles, and strategies to overcome them, are elaborated in the following.

Large-scale dispersion of monochiral SWCNTs for optoelectronics. To date, post-growth separation of SWCNTs is needed to provide monodisperse nanotubes for applications. Polymer wrapping of SWCNTs proved to provide the highest quality but is, so far, limited to few chiralities that can be efficiently selected. Testing further combination of SWCNT sources and polymers is necessary to supplement the spectrum of nanotubes. Concerning the initial dispersion, SFM solves some of the major problems in post-growth selection and separation of SWCNTs, such as, scalability and damage to the carbon lattice. The amount and quality of SWCNTs yielded by SFM drastically expands and simplifies their application in macroscopic optoelectronic devices. To date, shear-force mixed SWCNTs were employed

- in OLEDs as nIR light sources,[2]
- in optical microcavities for strong light-matter coupling,[3] and trion-polaritons,[186]

- in LEFET-cavities for electrically pumped exciton-polaritons,[4]
- for coupling to plasmonic crystals,[218–220]
- in electrochromic notch filters,[221]
- in LEFET for studying electronic properties,[46, 222–225]
- in solar cells as absorbing material (in collaboration with Prof. C. Brabec, FAU Erlangen).

Nevertheless, the obtained SWCNTs exhibit a still rather moderate PLQY of 2% impeding the performance of light-emitting devices. The PL efficiency is intrinsically limited by the formation of dark excitons and additionally suffers from imperfections of the carbon nanotubes.[37] The introduction of radiative sp^3 defects was shown to increase radiative recombination.[29, 193, 194, 226] As an example, aryl functional groups were attached to the carbon lattice resulting in the formation of a radiative trap state. Owing to the efficient harvesting of radiative excitons by localization and simultaneously brightening of dark excitons, the overall PLQY is increased. So far, these experiments are limited to aqueous dispersions and small volumes. Incorporation of sp^3 defects in high quality polymer-wrapped SWCNTs on a large scale might provide efficient nanotube emitters for optoelectronic devices. In addition to intrinsic non-radiative processes, the PLQY is decreased by an order of magnitude in thin films compared to that in dispersion. This effect is associated with environmental fluctuations of the surrounding host material and the resulting interactions.[35] Reducing these inhomogeneities and interactions by, for example, exciton-localization or novel host materials is an important step towards efficient nIR-emission from SWCNT-based devices. The separation of monochiral SWCNTs on large scale paves the way for applications of carbon nanotubes as nIR-emitters beyond the scope of previous reports that focused on individual nanotubes or sparse networks.

Near-infrared light sources: SWCNT-based OLEDs. The lack of suitable organic materials impedes the use of OLED in the nIR, beyond 800 nm. Such OLEDs, however, hold great promise for providing controlled illumination in biomedical applications, optical data communication and night vision. In this thesis, the first OLED based on SWCNT emitters was presented. Narrow linewidth and pure nIR electroluminescence (>1,000 nm) was obtained from these devices. In contrast to other low-bandgap carbon-based materials, SWCNTs provide superior stability against bleaching and high currents as well as tunable emission by varying the employed chirality. Further, SWCNTs are processed from solution, highly flexible and do not contain heavy metals – limitations of previous nIR-OLEDs.

The first generation of OLEDs based on SWCNT emitters exhibited an EQE that was limited by the efficiency of radiative decay. The overall EQE of the light-emitting devices would thus significantly gain from an improved PLQY of the SWCNTs. With respect to the electrical performance, the OLEDs showed efficient charge-carrier injection and balanced recombination. The

used device architecture will be suitable for OLEDs comprising other chiralities than (6,5) and hence can cover the entire nIR. For this purpose, the selection of different chiralities must be optimized, e.g., by polymer-wrapping.[57] The devices will also benefit from improved deposition techniques leading to more evenly distributed nanotube thin films. Recently developed methods, including aerosol jet printing[46] and aligned deposition by filtration[213], would improve device characteristics and result in pure excitonic emission. In the field of OLEDs, SWCNT will ultimately need to compete with more efficient emitter materials, such as quantum dots[180] and small molecules[89].

SWCNT-filled optical cavities: Strong light-matter coupling in the nIR. The formation of hybrid light-matter particles, called exciton-polaritons, promise to make quantum-mechanical phenomena, e.g. BEC and superfluidity, easily accessible. The high oscillator strength and binding energy of excitons in SWCNTs favor the observation of strong light-matter coupling at room temperature. Embedded in metal-clad cavities, SWCNTs showed significant photon-exciton hybridization – even at moderate concentrations of 2 wt% – in the nIR and at room-temperature. Owing to the narrow linewidth of excitonic excitations in SWCNTs, the coupling becomes particularly pronounced, which supports unambiguous observations of light-matter coupling in more advanced cavities, for example, within highly reflective DBR-mirrors.

As a result of the extremely high oscillator strength, SWCNTs facilitate strong light-matter coupling even at moderate concentrations. In the future, these properties might be utilized to achieve 1) strong coupling in individual SWCNTs, 2) ultrastrong coupling, and 3) high densities of polaritons by optical pumping.

First, the oscillator strength of an individual SWCNT is sufficient to achieve strong light-matter coupling in a cavity with sufficiently small mode-volume. Ultra-low mode volume photonic crystals[99] or nanoparticles[100] could be employed for coupling to single nanotubes. In combination with appropriate pump sources – optically or electrically[227, 228] – such cavities might support low-threshold polariton lasing as the number of states is limited in these systems.

Second, based on the extrapolation of the results in Chapter 6, ultrastrong coupling can be readily achieved using SWCNTs. These data suggest that a SWCNT concentration of 10 wt% is needed to result in a Rabi splitting larger than 20% of the exciton energy (in metal-clad cavities). Recently, ultrastrong coupling has been achieved in SWCNT-cavities using aligned nanotubes showing the peculiar emergence of exceptional points.[229] PL spectroscopy and thus polariton dynamics at the exceptional points might reveal interesting phenomena. Towards this end, these experiments must be conducted with high quality SWCNTs. Further increasing the concentration of the nanotubes could even increase the coupling strength beyond the exciton energy. In this case, deep strong coupling would be reached for which exciting new physics are predicted, for example, ultra-efficient emission.[230]

Third, the density of exciton polaritons can be increased to achieve, ultimately, polariton lasing in SWCNT-filled cavities. The polariton density, presented in this thesis, is mainly limited

by the short polariton lifetime leading to rapid leakage from the cavity. In order to increase the polariton lifetime, highly reflective DBR-mirrors must be employed. Additionally, in-plane confinement of polaritons by etching micro-pillars or a top mirror with a Gaussian defect might prevent polariton diffusion.[118, 231] Apart from the lifetime, enhanced relaxation favors the accumulation of polaritons in the ground state. Here, polariton relaxation can be enhanced by using a dense and thin layer of SWCNTs as observed for LEFET-cavities. Moreover, the introduction of sp^3 defects might improve, in addition to enhancing the lifetime, radiative as well as non-radiative relaxation and scattering paths. Finally, the excellent photostability and thermal conductivity of SWCNTs enables pumping these cavities with intense laser pulses as required for polariton condensation. Future research needs to show whether the structural stability is maintained when incorporating bright defects along the nanotubes.

LEFET-cavities: Electrical pumping and tuning of exciton-polaritons with SWCNTs. Current-driven strongly coupled cavities are typically associated with low pumping rates (organic materials) or require complex device fabrication and low temperatures for operation (inorganic materials). In this thesis, SWCNT-based LEFETs were built to generate electrically pumped exciton-polaritons at high current densities and at room temperature. Compared to previous work on strongly coupled OLED-cavities, exciton-pumping rates 10^4 higher than previously reported were reached in the LEFET-cavities. These results highlight that high current densities and room temperature stable exciton-polaritons are no longer mutually exclusive. In the unipolar regime, gate-dependent charge accumulation in the LEFETs leads to on-demand switching between strong and weak coupling. Electrical control of the light-matter coupling in the cavity might prove useful for precisely tuning the energy of the LP. Overall, the concept of the developed LEFET-cavities can be applied to any ambipolar material as demonstrated in a co-authored publication on electrical pumping of polaritons in DPPT-BT polymer.[203] Devices based on SWCNTs, however, exhibit superior electrical properties and support higher current densities due to the superior charge carrier mobilities inherent in carbon nanotubes.

Towards electrically pumped polariton lasing. Electrical pumping of polaritons in LEFET-cavities was achieved at high current densities. An analysis of the experimental results suggests that a mean ground state occupation of 0.004 was reached in these devices, while polariton lasing requires an occupation above unity. Owing to the employed metal-clad cavities, the accumulated polariton density is mainly limited by the short polariton lifetime leading to rapid polariton leakage. By increasing the quality factor of the cavity from 28 to, for example, 400 (1000) the ground state occupation in the LEFET-cavities would increase 14 (35) times. The required implementation of DBR mirrors to LEFET-cavities can be achieved by using a split-gate device architecture.[232] In this way, a metal-free optical cavity can be formed while maintaining efficient charge carrier injection and transport.

In addition to improvements of the optical characteristics, an advanced electrical pumping scheme can be employed to operate at higher current densities. Patterning the SWCNT layer

inside the channel can effectively increase the pumping rate by current focusing towards the center of the channel. The current can be further enhanced by alignment of the SWCNTs inside the LEFETs.[233] Moreover, the presented work on electrical pumping and tuning of exciton-polaritons in LEFETs is not limited to the use of SWCNTs. In the course of this work, ultrastrong light-matter coupling and electrically excited polaritons were observed for the donor-acceptor polymer DPPT-BT. Using a material, which offers similarly high ambipolar charge transport and exhibits a high PLQY, would additionally increase the polariton density. These improvements bring electrical pumping of polariton condensates at room temperature within realistic reach.

Final remarks. To conclude, SWCNTs are a fascinating material that promises to overcome past limitations in the field of carbon-based optoelectronics. The experimental realization and fundamental understanding of prospects and properties greatly benefit from the extensive research over the past decades. Beyond the work of this thesis, other pioneering research enabled the recent development of SWCNT-based single-photon sources[42, 234, 235] and carbon nanotube electronics outperforming silicon transistors[16]. The intriguing properties of SWCNTs hold the potential to enable the discovery of novel physical effects as well as future optoelectronic applications in the nIR.

BIBLIOGRAPHY

[1] Arko Graf, Yuriy Zakharko, Stefan P Schießl, Claudia Backes, Moritz Pfohl, Benjamin S Flavel, and Jana Zaumseil.
Large scale, selective dispersion of long single-walled carbon nanotubes with high photoluminescence quantum yield by shear force mixing.
Carbon, 105:593–599, 2016.

[2] Arko Graf, Caroline Murawski, Yuriy Zakharko, Jana Zaumseil, and Malte C Gather.
Infrared organic light-emitting diodes with carbon nanotube emitters.
Advanced Materials, 30(12):1706711, 2018.

[3] Arko Graf, Laura Tropf, Yuriy Zakharko, Jana Zaumseil, and Malte C Gather.
Near-infrared exciton-polaritons in strongly coupled single-walled carbon nanotube microcavities.
Nature communications, 7:13078, 2016.

[4] Arko Graf, Martin Held, Yuriy Zakharko, Laura Tropf, Malte C Gather, and Jana Zaumseil.
Electrical pumping and tuning of exciton-polaritons in carbon nanotube microcavities.
Nature materials, 16(9):911, 2017.

[5] Arko Graf, Laura Tropf, Jana Zaumseil, and Malte C Gather.
Chapter 9 – strong light-matter interactions and exciton-polaritons in organic materials.
In O. Ostroverkhova, editor, *Handbook of Organic Materials for Electronic and Photonic Devices*, pages 281–307. Woodhead Publishing, Duxford, second edition, 2018.

[6] Riichiro Saito and Mildred S. Dresselhaus.
Chapter 5 – optical properties of carbon nanotubes.
In K. Tanaka and S. Iijima, editors, *Carbon Nanotubes and Graphene*, pages 77 – 98. Elsevier, Oxford, second edition, 2014.

[7] François Léonard.
Physics of carbon nanotube devices.
William Andrew, Norwich, first edition, 2008.

[8] Alexander A Balandin.

Thermal properties of graphene and nanostructured carbon materials.
Nature materials, 10(8):569, 2011.

[9] Francesco Bonaccorso, Z Sun, Ta Hasan, and AC Ferrari.
Graphene photonics and optoelectronics.
Nature photonics, 4(9):611, 2010.

[10] Moritz Pfohl, Konstantin Glaser, Arko Graf, Adrian Mertens, Daniel D Tune, Tanja Puerckhauer, Asiful Alam, Li Wei, Yuan Chen, Jana Zaumseil, et al.
Probing the diameter limit of single walled carbon nanotubes in swcnt: fullerene solar cells.
Advanced Energy Materials, 6(21):1600890, 2016.

[11] Wuxu Zhang, Zhenzhong Zhang, and Yingge Zhang.
The application of carbon nanotubes in target drug delivery systems for cancer therapies.
Nanoscale research letters, 6(1):555, 2011.

[12] H-S Philip Wong and Deji Akinwande.
Carbon nanotube and graphene device physics.
Cambridge University Press, 2011.

[13] Shaoming Huang, Xinyu Cai, and Jie Liu.
Growth of millimeter-long and horizontally aligned single-walled carbon nanotubes on flat substrates.
Journal of the American Chemical Society, 125(19):5636–5637, 2003.

[14] Ali Javey and Jing Kong.
Carbon nanotube electronics.
Springer Science & Business Media, 2009.

[15] Carter T White and Tchavdar N Todorov.
Carbon nanotubes as long ballistic conductors.
Nature, 393(6682):240, 1998.

[16] Gerald J Brady, Austin J Way, Nathaniel S Safron, Harold T Evensen, Padma Gopalan, and Michael S Arnold.
Quasi-ballistic carbon nanotube array transistors with current density exceeding si and gaas.
Science advances, 2(9):e1601240, 2016.

[17] Riichiro Saito, G Dresselhaus, and MS Dresselhaus.
Trigonal warping effect of carbon nanotubes.
Physical Review B, 61(4):2981, 2000.

[18] Jeroen WG Wilder, Liesbeth C Venema, Andrew G Rinzler, Richard E Smalley, and Cees Dekker.
Electronic structure of atomically resolved carbon nanotubes.
Nature, 391(6662):59, 1998.

[19] Christophe Voisin, Sebastien Berger, Stephane Berciaud, Hugen Yan, Jean-Sébastien Lauret, Guillaume Cassabois, Philippe Roussignol, James Hone, and Tony F Heinz.
Excitonic signatures in the optical response of single-wall carbon nanotubes.
Physica Status Solidi (B), 249(5):900–906, 2012.

[20] Mai Takase, Hiroshi Ajiki, Yoshihiko Mizumoto, Keiichiro Komeda, Masanobu Nara, Hideki Nabika, Satoshi Yasuda, Hajime Ishihara, and Kei Murakoshi.
Selection-rule breakdown in plasmon-induced electronic excitation of an isolated single-walled carbon nanotube.
Nature Photonics, 7(7):550, 2013.

[21] R Bruce Weisman and Sergei M Bachilo.
Dependence of optical transition energies on structure for single-walled carbon nanotubes in aqueous suspension: an empirical kataura plot.
Nano Letters, 3(9):1235–1238, 2003.

[22] Catalin D Spataru, Sohrab Ismail-Beigi, Lorin X Benedict, and Steven G Louie.
Excitonic effects and optical spectra of single-walled carbon nanotubes.
Physical Review Letters, 92(7):077402, 2004.

[23] J Maultzsch, R Pomraenke, S Reich, E Chang, D Prezzi, Alice Ruini, Elisa Molinari, MS Strano, C Thomsen, and C Lienau.
Exciton binding energies in carbon nanotubes from two-photon photoluminescence.
Physical Review B, 72(24):241402, 2005.

[24] Shinji Yamashita, Yahachi Saito, and Jong Hyun Choi.
Carbon nanotubes and graphene for photonic applications.
Elsevier, 2013.

[25] Mildred S Dresselhaus, Gene Dresselhaus, Riichiro Saito, and Ado Jorio.
Exciton photophysics of carbon nanotubes.
Annu. Rev. Phys. Chem., 58:719–747, 2007.

[26] Phaedon Avouris, Marcus Freitag, and Vasili Perebeinos.
Carbon-nanotube photonics and optoelectronics.
Nature photonics, 2(6):341, 2008.

[27] Jeffrey L Blackburn, Josh M Holt, Veronica M Irurzun, Daniel E Resasco, and Garry Rumbles.
Confirmation of k-momentum dark exciton vibronic sidebands using 13c-labeled, highly enriched (6, 5) single-walled carbon nanotubes.
Nano letters, 12(3):1398–1403, 2012.

[28] Rodrigo B Capaz, Catalin D Spataru, Sohrab Ismail-Beigi, and Steven G Louie.
Diameter and chirality dependence of exciton properties in carbon nanotubes.
Physical Review B, 74(12):121401, 2006.

[29] Yanmei Piao, Brendan Meany, Lyndsey R Powell, Nicholas Valley, Hyejin Kwon, George C Schatz, and YuHuang Wang.
Brightening of carbon nanotube photoluminescence through the incorporation of sp 3 defects.
Nature chemistry, 5(10):840, 2013.

[30] Ryusuke Matsunaga, Kazunari Matsuda, and Yoshihiko Kanemitsu.
Origin of low-energy photoluminescence peaks in single carbon nanotubes: K-momentum dark excitons and triplet dark excitons.
Physical Review B, 81(3):033401, 2010.

[31] Kotaro Nagatsu, Shohei Chiashi, Satoru Konabe, and Yoshikazu Homma.
Brightening of triplet dark excitons by atomic hydrogen adsorption in single-walled carbon nanotubes observed by photoluminescence spectroscopy.
Physical review letters, 105(15):157403, 2010.

[32] Christoph Mann and Tobias Hertel.
13 nm exciton size in (6, 5) single-wall carbon nanotubes.
The journal of physical chemistry letters, 7(12):2276–2280, 2016.

[33] Friedrich Schöppler, Christoph Mann, Tilman C Hain, Felix M Neubauer, Giulia Privitera, Francesco Bonaccorso, Daping Chu, Andrea C Ferrari, and Tobias Hertel.
Molar extinction coefficient of single-wall carbon nanotubes.
The Journal of Physical Chemistry C, 115(30):14682–14686, 2011.

[34] Giancarlo Soavi, Francesco Scotognella, Guglielmo Lanzani, and Giulio Cerullo.
Ultrafast photophysics of single-walled carbon nanotubes.
Advanced Optical Materials, 4(11):1670–1688, 2016.

[35] Matthias S Hofmann, Jan T Glückert, Jonathan Noé, Christian Bourjau, Raphael Dehmel, and Alexander Högele.
Bright, long-lived and coherent excitons in carbon nanotube quantum dots.
Nature nanotechnology, 8(7):502, 2013.

[36] Yuhei Miyauchi, Hideki Hirori, Kazunari Matsuda, and Yoshihiko Kanemitsu.
Radiative lifetimes and coherence lengths of one-dimensional excitons in single-walled carbon nanotubes.
Physical Review B, 80(8):081410, 2009.

[37] Tonya K Cherukuri, Dmitri A Tsyboulski, and R Bruce Weisman.
Length-and defect-dependent fluorescence efficiencies of individual single-walled carbon nanotubes.
ACS nano, 6(1):843–850, 2011.

[38] Ibrahim Sarpkaya, Zhengyi Zhang, William Walden-Newman, Xuesi Wang, James Hone, Chee W Wong, and Stefan Strauf.
Prolonged spontaneous emission and dephasing of localized excitons in air-bridged carbon nanotubes.
Nature communications, 4:2152, 2013.

[39] Tobias Hertel, Sabine Himmelein, Thomas Ackermann, Dominik Stich, and Jared Crochet.
Diffusion limited photoluminescence quantum yields in 1-d semiconductors: single-wall carbon nanotubes.
ACS nano, 4(12):7161–7168, 2010.

[40] J Lefebvre, Paul Finnie, and Y Homma.
Temperature-dependent photoluminescence from single-walled carbon nanotubes.
Physical Review B, 70(4):045419, 2004.

[41] Brian A Larsen, Pravas Deria, Josh M Holt, Ian N Stanton, Michael J Heben, Michael J Therien, and Jeffrey L Blackburn.
Effect of solvent polarity and electrophilicity on quantum yields and solvatochromic shifts of single-walled carbon nanotube photoluminescence.
Journal of the American Chemical Society, 134(30):12485–12491, 2012.

[42] Svetlana Khasminskaya, Felix Pyatkov, Karolina Słowik, Simone Ferrari, Oliver Kahl, Vadim Kovalyuk, Patrik Rath, Andreas Vetter, Frank Hennrich, Manfred M Kappes, et al.
Fully integrated quantum photonic circuit with an electrically driven light source.
Nature Photonics, 10(11):727, 2016.

[43] Xiaowei He, Nicolai F Hartmann, Xuedan Ma, Younghee Kim, Rachelle Ihly, Jeffrey L Blackburn, Weilu Gao, Junichiro Kono, Yohei Yomogida, Atsushi Hirano, et al.
Tunable room-temperature single-photon emission at telecom wavelengths from sp 3 defects in carbon nanotubes.
Nature Photonics, 11(9):577, 2017.

[44] Takumi Endo, Junko Ishi-Hayase, and Hideyuki Maki.
Photon antibunching in single-walled carbon nanotubes at telecommunication wavelengths and room temperature.
Applied Physics Letters, 106(11):113106, 2015.

[45] Guosong Hong, Shuo Diao, Junlei Chang, Alexander L Antaris, Changxin Chen, Bo Zhang, Su Zhao, Dmitriy N Atochin, Paul L Huang, Katrin I Andreasson, et al.
Through-skull fluorescence imaging of the brain in a new near-infrared window.
Nature Photonics, 8(9):723, 2014.

[46] Marcel Rother, Maximilian Brohmann, Shuyi Yang, Stefan B Grimm, Stefan P Schießl, Arko Graf, and Jana Zaumseil.
Aerosol-jet printing of polymer-sorted (6, 5) carbon nanotubes for field-effect transistors with high reproducibility.
Advanced Electronic Materials, 3(8):1700080, 2017.

[47] Hiroaki Ozawa, Natsuko Ide, Tsuyohiko Fujigaya, Yasuro Niidome, and Naotoshi Nakashima.
One-pot separation of highly enriched (6, 5)-single-walled carbon nanotubes using a fluorene-based copolymer.
Chemistry letters, 40(3):239–241, 2011.

[48] Stefan P Schießl, Nils Fröhlich, Martin Held, Florentina Gannott, Manuel Schweiger, Michael Forster, Ullrich Scherf, and Jana Zaumseil.
Polymer-sorted semiconducting carbon nanotube networks for high-performance ambipolar field-effect transistors.
ACS applied materials & interfaces, 7(1):682–689, 2014.

[49] Giulio Lolli, Liang Zhang, Leandro Balzano, Nataphan Sakulchaicharoen, Yongqiang Tan, and Daniel E Resasco.
Tailoring (n, m) structure of single-walled carbon nanotubes by modifying reaction conditions and the nature of the support of como catalysts.
The Journal of Physical Chemistry B, 110(5):2108–2115, 2006.

[50] Juan Ramon Sanchez-Valencia, Thomas Dienel, Oliver Gröning, Ivan Shorubalko, Andreas Mueller, Martin Jansen, Konstantin Amsharov, Pascal Ruffieux, and Roman Fasel.
Controlled synthesis of single-chirality carbon nanotubes.
Nature, 512(7512):61, 2014.

[51] Shuchen Zhang, Lianming Tong, and Jin Zhang.
The road to chirality-specific growth of single-walled carbon nanotubes.
National Science Review, 5(3):310–312, 2017.

[52] Xiulan Zhao, Shuchen Zhang, Zhenxing Zhu, Jin Zhang, Fei Wei, and Yan Li.
Catalysts for single-wall carbon nanotube synthesis—from surface growth to bulk preparation.
MRS Bulletin, 42(11):809–818, 2017.

[53] Yabin Chen, Yingying Zhang, Yue Hu, Lixing Kang, Shuchen Zhang, Huanhuan Xie, Dan Liu, Qiuchen Zhao, Qingwen Li, and Jin Zhang.
State of the art of single-walled carbon nanotube synthesis on surfaces.
Advanced Materials, 26(34):5898–5922, 2014.

[54] Sergei M Bachilo, Leandro Balzano, Jose E Herrera, Francisco Pompeo, Daniel E Resasco, and R Bruce Weisman.
Narrow (n, m)-distribution of single-walled carbon nanotubes grown using a solid supported catalyst.
Journal of the American Chemical Society, 125(37):11186–11187, 2003.

[55] Huaping Liu, Daisuke Nishide, Takeshi Tanaka, and Hiromichi Kataura.
Large-scale single-chirality separation of single-wall carbon nanotubes by simple gel chromatography.
Nature communications, 2:309, 2011.

[56] Naoki Komatsu and Feng Wang.
A comprehensive review on separation methods and techniques for single-walled carbon nanotubes.
Materials, 3(7):3818–3844, 2010.

[57] Huiliang Wang and Zhenan Bao.
Conjugated polymer sorting of semiconducting carbon nanotubes and their electronic applications.
Nano Today, 10(6):737–758, 2015.

[58] Wen Hui Duan, Quan Wang, and Frank Collins.
Dispersion of carbon nanotubes with sds surfactants: a study from a binding energy perspective.
Chemical Science, 2(7):1407–1413, 2011.

[59] Jeffrey A Fagan, Constantine Y Khripin, Carlos A Silvera Batista, Jeffrey R Simpson, Erik H Hároz, Angela R Hight Walker, and Ming Zheng.
Isolation of specific small-diameter single-wall carbon nanotube species via aqueous two-phase extraction.
Advanced Materials, 26(18):2800–2804, 2014.

[60] F Bonaccorso, T Hasan, PH Tan, C Sciascia, G Privitera, G Di Marco, PG Gucciardi, and AC Ferrari.
Density gradient ultracentrifugation of nanotubes: Interplay of bundling and surfactants encapsulation.
The Journal of Physical Chemistry C, 114(41):17267–17285, 2010.

[61] Saunab Ghosh, Sergei M Bachilo, and R Bruce Weisman.
Advanced sorting of single-walled carbon nanotubes by nonlinear density-gradient ultracentrifugation.
Nature nanotechnology, 5(6):443, 2010.

[62] Jared Crochet, Michael Clemens, and Tobias Hertel.
Quantum yield heterogeneities of aqueous single-wall carbon nanotube suspensions.
Journal of the American Chemical Society, 129(26):8058–8059, 2007.

[63] Suman Kalyan Samanta, Martin Fritsch, Ullrich Scherf, Widianta Gomulya, Satria Zulkarnaen Bisri, and Maria Antonietta Loi.
Conjugated polymer-assisted dispersion of single-wall carbon nanotubes: the power of polymer wrapping.
Accounts of chemical research, 47(8):2446–2456, 2014.

[64] Adrian Nish, Jeong-Yuan Hwang, James Doig, and Robin J Nicholas.
Highly selective dispersion of single-walled carbon nanotubes using aromatic polymers.
Nature nanotechnology, 2(10):640, 2007.

[65] Widianta Gomulya, Jia Gao, and Maria Antonietta Loi.
Conjugated polymer-wrapped carbon nanotubes: physical properties and device applications.
The European Physical Journal B, 86(10):404, 2013.

[66] Jia Gao, Maria Antonietta Loi, Elton José Figueiredo de Carvalho, and Maria Cristina dos Santos.
Selective wrapping and supramolecular structures of polyfluorene–carbon nanotube hybrids.
ACS nano, 5(5):3993–3999, 2011.

[67] Florian Jakubka, Stefan P Schießl, Sebastian Martin, Jan M Englert, Frank Hauke, Andreas Hirsch, and Jana Zaumseil.
Effect of polymer molecular weight and solution parameters on selective dispersion of single-walled carbon nanotubes.
ACS Macro Letters, 1(7):815–819, 2012.

[68] Shinichiro Mouri, Yuhei Miyauchi, and Kazunari Matsuda.
Dispersion-process effects on the photoluminescence quantum yields of single-walled carbon nanotubes dispersed using aromatic polymers.
The Journal of Physical Chemistry C, 116(18):10282–10286, 2012.

[69] W Helfrich and WG Schneider.
Recombination radiation in anthracene crystals.
Physical Review Letters, 14(7):229, 1965.

[70] Ching W Tang and Steven A VanSlyke.
Organic electroluminescent diodes.
Applied physics letters, 51(12):913–915, 1987.

[71] J Blochwitz, Martin Pfeiffer, Torsten Fritz, and Karl Leo.
Low voltage organic light emitting diodes featuring doped phthalocyanine as hole transport material.
Applied Physics Letters, 73(6):729–731, 1998.

[72] Hiroki Uoyama, Kenichi Goushi, Katsuyuki Shizu, Hiroko Nomura, and Chihaya Adachi.
Highly efficient organic light-emitting diodes from delayed fluorescence.
Nature, 492(7428):234, 2012.

[73] Bernard Geffroy, Philippe Le Roy, and Christophe Prat.
Organic light-emitting diode (oled) technology: materials, devices and display technologies.
Polymer International, 55(6):572–582, 2006.

[74] K Walzer, B Maennig, M Pfeiffer, and K Leo.
Highly efficient organic devices based on electrically doped transport layers.
Chemical reviews, 107(4):1233–1271, 2007.

[75] Kiran T Kamtekar, Andrew P Monkman, and Martin R Bryce.
Recent advances in white organic light-emitting materials and devices (woleds).
Advanced Materials, 22(5):572–582, 2010.

[76] M Pfeiffer, K Leo, X Zhou, JS Huang, M Hofmann, A Werner, and J Blochwitz-Nimoth.
Doped organic semiconductors: Physics and application in light emitting diodes.
Organic Electronics, 4(2-3):89–103, 2003.

[77] Caroline Weichsel, Sebastian Reineke, Mauro Furno, Björn Lüssem, and Karl Leo.
Organic light-emitting diodes for lighting: High color quality by controlling energy transfer processes in host-guest-systems.
Journal of Applied Physics, 111(3):033102, 2012.

[78] K Harada, AG Werner, M Pfeiffer, CJ Bloom, CM Elliott, and K Leo.
Organic homojunction diodes with a high built-in potential: Interpretation of the current-voltage characteristics by a generalized einstein relation.
Physical review letters, 94(3):036601, 2005.

[79] Philipp Liehm, Caroline Murawski, Mauro Furno, Björn Lüssem, Karl Leo, and Malte C Gather.
Comparing the emissive dipole orientation of two similar phosphorescent green emitter molecules in highly efficient organic light-emitting diodes.
Applied Physics Letters, 101(25):253304, 2012.

[80] Moon Sung Kang and C Daniel Frisbie.
A pedagogical perspective on ambipolar fets.
ChemPhysChem, 14(8):1547–1552, 2013.

[81] Jana Zaumseil, Richard H Friend, and Henning Sirringhaus.
Spatial control of the recombination zone in an ambipolar light-emitting organic transistor.
Nature materials, 5(1):69, 2006.

[82] Jana Zaumseil, Chris Groves, Jessica M Winfield, Neil C Greenham, and Henning Sirringhaus.
Electron–hole recombination in uniaxially aligned semiconducting polymers.
Advanced Functional Materials, 18(22):3630–3637, 2008.

[83] Michael C Gwinner, Florian Jakubka, Florentina Gannott, Henning Sirringhaus, and Jana Zaumseil.
Enhanced ambipolar charge injection with semiconducting polymer/carbon nanotube thin films for light-emitting transistors.
ACS nano, 6(1):539–548, 2011.

[84] Jana Zaumseil and Henning Sirringhaus.
Electron and ambipolar transport in organic field-effect transistors.
Chemical reviews, 107(4):1296–1323, 2007.

[85] Zachary A Lamport, Hamna F Haneef, Sajant Anand, Matthew Waldrip, and Oana D Jurchescu.
Tutorial: Organic field-effect transistors: Materials, structure and operation.
Journal of Applied Physics, 124(7):071101, 2018.

[86] Roland Schmechel, Marcus Ahles, and Heinz von Seggern.
A pentacene ambipolar transistor: Experiment and theory.
Journal of applied physics, 98(8):084511, 2005.

[87] Mauro Furno, Rico Meerheim, Michael Thomschke, Simone Hofmann, Björn Lüssem, and Karl Leo.
Outcoupling efficiency in small-molecule oleds: from theory to experiment.
In *Light-Emitting Diodes: Materials, Devices, and Applications for Solid State Lighting XIV*, volume 7617, page 761716. International Society for Optics and Photonics, 2010.

[88] Chihaya Adachi, Marc A Baldo, Mark E Thompson, and Stephen R Forrest.
Nearly 100% internal phosphorescence efficiency in an organic light-emitting device.
Journal of Applied Physics, 90(10):5048–5051, 2001.

[89] Kiet Tuong Ly, Ren-Wu Chen-Cheng, Hao-Wu Lin, Yu-Jeng Shiau, Shih-Hung Liu, Pi-Tai Chou, Cheng-Si Tsao, Yu-Ching Huang, and Yun Chi.
Near-infrared organic light-emitting diodes with very high external quantum efficiency and radiance.
Nature Photonics, 11(1):63, 2017.

[90] Wolfgang Brütting, Jörg Frischeisen, Tobias D Schmidt, Bert J Scholz, and Christian Mayr.
Device efficiency of organic light-emitting diodes: Progress by improved light outcoupling.
Physica Status Solidi (A), 210(1):44–65, 2013.

[91] Michael C Gwinner, Dinesh Kabra, Matthew Roberts, Thomas JK Brenner, Bodo H Wallikewitz, Christopher R McNeill, Richard H Friend, and Henning Sirringhaus.
Highly efficient single-layer polymer ambipolar light-emitting field-effect transistors.
Advanced Materials, 24(20):2728–2734, 2012.

[92] Malte C Gather and Sebastian Reineke.
Recent advances in light outcoupling from white organic light-emitting diodes.
Journal of Photonics for Energy, 5(1):057607, 2015.

[93] Matthew J Jurow, Christian Mayr, Tobias D Schmidt, Thomas Lampe, Peter I Djurovich, Wolfgang Brütting, and Mark E Thompson.
Understanding and predicting the orientation of heteroleptic phosphors in organic light-emitting materials.
Nature materials, 15(1):85, 2016.

[94] Rodney Loudon.
The quantum theory of light.
OUP Oxford, 2000.

[95] Edward Mills Purcell.
Spontaneous emission probabilities at radio frequencies.
In *Confined Electrons and Photons*, pages 839–839. Springer, 1995.

[96] Daniele Bajoni.
Polariton lasers. hybrid light–matter lasers without inversion.
Journal of Physics D: Applied Physics, 45(31):313001, 2012.

[97] KS Daskalakis, SA Maier, Ray Murray, and Stéphane Kéna-Cohen.
Nonlinear interactions in an organic polariton condensate.
Nature materials, 13(3):271, 2014.

[98] Alberto Amo, Jérôme Lefrère, Simon Pigeon, Claire Adrados, Cristiano Ciuti, Iacopo Carusotto, Romuald Houdré, Elisabeth Giacobino, and Alberto Bramati.
Superfluidity of polaritons in semiconductor microcavities.
Nature Physics, 5(11):805, 2009.

[99] R Miura, S Imamura, R Ohta, A Ishii, X Liu, T Shimada, S Iwamoto, Y Arakawa, and YK Kato.
Ultralow mode-volume photonic crystal nanobeam cavities for high-efficiency coupling to individual carbon nanotube emitters.
Nature communications, 5:5580, 2014.

[100] Rohit Chikkaraddy, Bart de Nijs, Felix Benz, Steven J Barrow, Oren A Scherman, Edina Rosta, Angela Demetriadou, Peter Fox, Ortwin Hess, and Jeremy J Baumberg.
Single-molecule strong coupling at room temperature in plasmonic nanocavities.
Nature, 535(7610):127, 2016.

[101] Kerry J Vahala.
Optical microcavities.
Nature, 424(6950):839, 2003.

[102] K Thyagarajan and Ajoy Ghatak.
Lasers: fundamentals and applications.
Springer Science & Business Media, 2010.

[103] Stéphane Kéna-Cohen, Stefan A Maier, and Donal DC Bradley.
Ultrastrongly coupled exciton–polaritons in metal-clad organic semiconductor microcavities.
Advanced Optical Materials, 1(11):827–833, 2013.

[104] Peter A Hobson, William L Barnes, DG Lidzey, GA Gehring, DM Whittaker, MS Skolnick, and S Walker.
Strong exciton–photon coupling in a low-q all-metal mirror microcavity.
Applied Physics Letters, 81(19):3519–3521, 2002.

[105] Jonathan Keeling and Natalia G Berloff.
Exciton–polariton condensation.
Contemporary Physics, 52(2):131–151, 2011.

[106] Shaoqiang Chen, Masahiro Yoshita, Akira Ishikawa, Toshimitsu Mochizuki, Shun Maruyama, Hidefumi Akiyama, Yuhei Hayamizu, Loren N Pfeiffer, and Ken W West.
Intrinsic radiative lifetime derived via absorption cross section of one-dimensional excitons.
Scientific reports, 3:1941, 2013.

[107] Ibrahim Sarpkaya, Ehsaneh D Ahmadi, Gabriella D Shepard, Kevin S Mistry, Jeffrey L Blackburn, and Stefan Strauf.
Strong acoustic phonon localization in copolymer-wrapped carbon nanotubes.
ACS nano, 9(6):6383–6393, 2015.

[108] S Kéna-Cohen and SR Forrest.
Room-temperature polariton lasing in an organic single-crystal microcavity.
Nature Photonics, 4(6):371, 2010.

[109] Tim Byrnes, Na Young Kim, and Yoshihisa Yamamoto.
Exciton–polariton condensates.
Nature Physics, 10(11):803, 2014.

[110] Christian Schneider, Arash Rahimi-Iman, Na Young Kim, Julian Fischer, Ivan G Savenko, Matthias Amthor, Matthias Lermer, Adriana Wolf, Lukas Worschech, Vladimir D Kulakovskii, et al.
An electrically pumped polariton laser.
Nature, 497(7449):348, 2013.

[111] Xiaoze Liu, Tal Galfsky, Zheng Sun, Fengnian Xia, Erh-chen Lin, Yi-Hsien Lee, Stéphane Kéna-Cohen, and Vinod M Menon.
Strong light–matter coupling in two-dimensional atomic crystals.
Nature Photonics, 9(1):30, 2015.

[112] David M Coles, Paolo Michetti, Caspar Clark, Wing Chung Tsoi, Ali M Adawi, Ji-Seon Kim, and David G Lidzey.
Vibrationally assisted polariton-relaxation processes in strongly coupled organic-semiconductor microcavities.
Advanced Functional Materials, 21(19):3691–3696, 2011.

[113] Dario Ballarini, Milena De Giorgi, Emiliano Cancellieri, Romuald Houdré, Elisabeth Giacobino, Roberto Cingolani, Alberto Bramati, Giuseppe Gigli, and Daniele Sanvitto.
All-optical polariton transistor.
Nature communications, 4:1778, 2013.

[114] GG Paschos, Niccolo Somaschi, SI Tsintzos, D Coles, JL Bricks, Zacharias Hatzopoulos, DG Lidzey, PG Lagoudakis, and Pavlos G Savvidis.
Hybrid organic-inorganic polariton laser.
Scientific Reports, 7(1):11377, 2017.

[115] J-M Ménard, Christoph Pöllmann, Michael Porer, Ursula Leierseder, E Galopin, A Lemaître, A Amo, J Bloch, and Rupert Huber.
Revealing the dark side of a bright exciton–polariton condensate.
Nature communications, 5:4648, 2014.

[116] David M Coles, Niccolo Somaschi, Paolo Michetti, Caspar Clark, Pavlos G Lagoudakis, Pavlos G Savvidis, and David G Lidzey.
Polariton-mediated energy transfer between organic dyes in a strongly coupled optical microcavity.
Nature materials, 13(7):712, 2014.

[117] Christof P Dietrich, Anja Steude, Laura Tropf, Marcel Schubert, Nils M Kronenberg, Kai Ostermann, Sven Höfling, and Malte C Gather.
An exciton-polariton laser based on biologically produced fluorescent protein.
Science advances, 2(8):e1600666, 2016.

[118] Daniele Bajoni, Pascale Senellart, Esther Wertz, Isabelle Sagnes, Audrey Miard, Aristide Lemaître, and Jacqueline Bloch.
Polariton laser using single micropillar gaas- gaalas semiconductor cavities.
Physical review letters, 100(4):047401, 2008.

[119] Guillaume Malpuech, Alexey Kavokin, and Fabrice P Laussy.
Polariton bose condensation in microcavities.
Physica Status Solidi (A), 195(3):568–578, 2003.

[120] Dmitry S Dovzhenko, Sergey V Ryabchuk, Yu P Rakovich, and IR Nabiev.
Light–matter interaction in the strong coupling regime: configurations, conditions, and applications.
Nanoscale, 10(8):3589–3605, 2018.

[121] David M Coles, Richard T Grant, David G Lidzey, Caspar Clark, and Pavlos G Lagoudakis.
Imaging the polariton relaxation bottleneck in strongly coupled organic semiconductor microcavities.
Physical Review B, 88(12):121303, 2013.

[122] AI Tartakovskii, M Emam-Ismail, RM Stevenson, MS Skolnick, VN Astratov, DM Whittaker, Jeremy J Baumberg, and JS Roberts.

Relaxation bottleneck and its suppression in semiconductor microcavities.
Physical Review B, 62(4):R2283, 2000.

[123] RM Stevenson, VN Astratov, MS Skolnick, DM Whittaker, M Emam-Ismail, AI Tartakovskii, PG Savvidis, JJ Baumberg, and JS Roberts.
Continuous wave observation of massive polariton redistribution by stimulated scattering in semiconductor microcavities.
Physical Review Letters, 85(17):3680, 2000.

[124] Konstantinos S Daskalakis, Stefan A Maier, and Stéphane Kéna-Cohen.
Spatial coherence and stability in a disordered organic polariton condensate.
Physical Review Letters, 115(3):035301, 2015.

[125] Johannes D Plumhof, Thilo Stöferle, Lijian Mai, Ullrich Scherf, and Rainer F Mahrt.
Room-temperature bose–einstein condensation of cavity exciton–polaritons in a polymer.
Nature materials, 13(3):247, 2014.

[126] Tamsin Cookson, Kyriacos Georgiou, Anton Zasedatelev, Richard T Grant, Tersilla Virgili, Marco Cavazzini, Francesco Galeotti, Caspar Clark, Natalia G Berloff, David G Lidzey, et al.
A yellow polariton condensate in a dye filled microcavity.
Advanced Optical Materials, 5(18):1700203, 2017.

[127] Giovanni Lerario, Antonio Fieramosca, Fábio Barachati, Dario Ballarini, Konstantinos S Daskalakis, Lorenzo Dominici, Milena De Giorgi, Stefan A Maier, Giuseppe Gigli, Stéphane Kéna-Cohen, et al.
Room-temperature superfluidity in a polariton condensate.
Nature Physics, 13(9):837, 2017.

[128] Rui Su, Carole Diederichs, Jun Wang, Timothy CH Liew, Jiaxin Zhao, Sheng Liu, Weigao Xu, Zhanghai Chen, and Qihua Xiong.
Room-temperature polariton lasing in all-inorganic perovskite nanoplatelets.
Nano letters, 17(6):3982–3988, 2017.

[129] David M Coles, Yanshen Yang, Yaya Wang, Richard T Grant, Robert A Taylor, Semion K Saikin, Alán Aspuru-Guzik, David G Lidzey, Joseph Kuo-Hsiang Tang, and Jason M Smith.
Strong coupling between chlorosomes of photosynthetic bacteria and a confined optical cavity mode.
Nature communications, 5:5561, 2014.

[130] Claude Weisbuch, Mr Nishioka, A Ishikawa, and Y Arakawa.

Observation of the coupled exciton-photon mode splitting in a semiconductor quantum microcavity.
Physical Review Letters, 69(23):3314, 1992.

[131] H Cao, S Pau, JM Jacobson, G Björk, Y Yamamoto, and A Imamoglu.
Transition from a microcavity exciton polariton to a photon laser.
Physical Review A, 55(6):4632, 1997.

[132] Stanley Pau, Hui Cao, Joseph Jacobson, Gunnar Björk, Yoshihisa Yamamoto, and Atac Imamoğlu.
Observation of a laserlike transition in a microcavity exciton polariton system.
Physical Review A, 54(3):R1789, 1996.

[133] Thilo Stöferle.
Exciton-polaritons: In full flow.
Nature Physics, 13(9):825, 2017.

[134] Pavlos G Savvidis.
Optoelectronics: A practical polariton laser.
Nature Photonics, 8(8):588, 2014.

[135] Daniele Sanvitto and Stéphane Kéna-Cohen.
The road towards polaritonic devices.
Nature materials, 15(10):1061, 2016.

[136] Junseok Heo, Shafat Jahangir, Bo Xiao, and Pallab Bhattacharya.
Room-temperature polariton lasing from gan nanowire array clad by dielectric microcavity.
Nano letters, 13(6):2376–2380, 2013.

[137] Ying-Yu Lai, Yu-Hsun Chou, Yu-Pin Lan, Tien-Chang Lu, Shing-Chung Wang, and Yoshihisa Yamamoto.
Crossover from polariton lasing to exciton lasing in a strongly coupled zno microcavity.
Scientific reports, 6:20581, 2016.

[138] David G Lidzey, DDC Bradley, MS Skolnick, T Virgili, S Walker, and DM Whittaker.
Strong exciton–photon coupling in an organic semiconductor microcavity.
Nature, 395(6697):53, 1998.

[139] Nataliya Bobrovska, Michał Matuszewski, Konstantinos S Daskalakis, Stefan A Maier, and Stéphane Kéna-Cohen.
Dynamical instability of a nonequilibrium exciton-polariton condensate.
ACS Photonics, 5(1):111–118, 2017.

[140] Jonathan R Tischler, M Scott Bradley, Vladimir Bulović, Jung Hoon Song, and Arto Nurmikko.
Strong coupling in a microcavity led.
Physical review letters, 95(3):036401, 2005.

[141] Grant H Lodden and Russell J Holmes.
Thermally activated population of microcavity polariton states under optical and electrical excitation.
Physical Review B, 83(7):075301, 2011.

[142] Grant H Lodden and Russell J Holmes.
Polarization splitting in polariton electroluminescence from an organic semiconductor microcavity with metallic reflectors.
Applied Physics Letters, 98(23):102, 2011.

[143] Nikolaos Christogiannis, Niccolo Somaschi, Paolo Michetti, David M Coles, Pavlos G Savvidis, Pavlos G Lagoudakis, and David G Lidzey.
Characterizing the electroluminescence emission from a strongly coupled organic semiconductor microcavity led.
Advanced Optical Materials, 1(7):503–509, 2013.

[144] Christopher R Gubbin, Stefan A Maier, and Stéphane Kéna-Cohen.
Low-voltage polariton electroluminescence from an ultrastrongly coupled organic light-emitting diode.
Applied Physics Letters, 104(23):85_1, 2014.

[145] M Mazzeo, A Genco, S Gambino, D Ballarini, F Mangione, O Di Stefano, S Patanè, S Savasta, D Sanvitto, and G Gigli.
Ultrastrong light-matter coupling in electrically doped microcavity organic light emitting diodes.
Applied Physics Letters, 104(23):86_1, 2014.

[146] Salvatore Gambino, Marco Mazzeo, Armando Genco, Omar Di Stefano, Salvatore Savasta, Salvatore Patané, Dario Ballarini, Federica Mangione, Giovanni Lerario, Daniele Sanvitto, et al.
Exploring light–matter interaction phenomena under ultrastrong coupling regime.
ACS Photonics, 1(10):1042–1048, 2014.

[147] John C de Mello, H Felix Wittmann, and Richard H Friend.
An improved experimental determination of external photoluminescence quantum efficiency.
Advanced materials, 9(3):230–232, 1997.

[148] Tai-Sang Ahn, Rabih O Al-Kaysi, Astrid M Müller, Katherine M Wentz, and Christopher J Bardeen.
Self-absorption correction for solid-state photoluminescence quantum yields obtained from integrating sphere measurements.
Review of Scientific Instruments, 78(8):086105, 2007.

[149] Nicole M Iverson, Paul W Barone, Mia Shandell, Laura J Trudel, Selda Sen, Fatih Sen, Vsevolod Ivanov, Esha Atolia, Edgardo Farias, Thomas P McNicholas, et al.
In vivo biosensing via tissue-localizable near-infrared-fluorescent single-walled carbon nanotubes.
Nature nanotechnology, 8(11):873, 2013.

[150] Svetlana Khasminskaya, Feliks Pyatkov, Benjamin S Flavel, Wolfram H Pernice, and Ralph Krupke.
Waveguide-integrated light-emitting carbon nanotubes.
Advanced Materials, 26(21):3465–3472, 2014.

[151] Florian Jakubka, Claudia Backes, Florentina Gannott, Udo Mundloch, Frank Hauke, Andreas Hirsch, and Jana Zaumseil.
Mapping charge transport by electroluminescence in chirality-selected carbon nanotube networks.
ACS nano, 7(8):7428–7435, 2013.

[152] Manuel Schweiger, Maximilian Schaudig, Florentina Gannott, Manuela S Killian, Erik Bitzek, Patrik Schmuki, and Jana Zaumseil.
Controlling the diameter of aligned single-walled carbon nanotubes on quartz via catalyst reduction time.
Carbon, 95:452–459, 2015.

[153] Florian Jakubka, Stefan B Grimm, Yuriy Zakharko, Florentina Gannott, and Jana Zaumseil.
Trion electroluminescence from semiconducting carbon nanotubes.
ACS nano, 8(8):8477–8486, 2014.

[154] Benjamin S Flavel, Katherine E Moore, Moritz Pfohl, Manfred M Kappes, and Frank Hennrich.
Separation of single-walled carbon nanotubes with a gel permeation chromatography system.
ACS nano, 8(2):1817–1826, 2014.

[155] Francesca Bottacchi, Luisa Petti, Florian Späth, Imge Namal, Gerhard Tröster, Tobias Hertel, and Thomas D Anthopoulos.

Polymer-sorted (6, 5) single-walled carbon nanotubes for solution-processed low-voltage flexible microelectronics.
Applied Physics Letters, 106(19):52_1, 2015.

[156] Anton V Naumov, Dmitri A Tsyboulski, Sergei M Bachilo, and R Bruce Weisman.
Length-dependent optical properties of single-walled carbon nanotube samples.
Chemical Physics, 422:255–263, 2013.

[157] Jeffrey A Fagan, Jeffrey R Simpson, Barry J Bauer, Silvia H De Paoli Lacerda, Matthew L Becker, Jaehun Chun, Kalman B Migler, Angela R Hight Walker, and Erik K Hobbie.
Length-dependent optical effects in single-wall carbon nanotubes.
Journal of the American Chemical Society, 129(34):10607–10612, 2007.

[158] Stefan P Schießl, Xander de Vries, Marcel Rother, Andrea Massé, Maximilian Brohmann, Peter A Bobbert, and Jana Zaumseil.
Modeling carrier density dependent charge transport in semiconducting carbon nanotube networks.
Physical Review Materials, 1(4):046003, 2017.

[159] Howon Yoon, Motoi Yamashita, Seisuke Ata, Don N Futaba, Takeo Yamada, and Kenji Hata.
Controlling exfoliation in order to minimize damage during dispersion of long swcnts for advanced composites.
Scientific reports, 4:3907, 2014.

[160] Keith R Paton, Eswaraiah Varrla, Claudia Backes, Ronan J Smith, Umar Khan, Arlene O'Neill, Conor Boland, Mustafa Lotya, Oana M Istrate, Paul King, et al.
Scalable production of large quantities of defect-free few-layer graphene by shear exfoliation in liquids.
Nature materials, 13(6):624, 2014.

[161] Eswaraiah Varrla, Claudia Backes, Keith R Paton, Andrew Harvey, Zahra Gholamvand, Joe McCauley, and Jonathan N Coleman.
Large-scale production of size-controlled mos2 nanosheets by shear exfoliation.
Chemistry of Materials, 27(3):1129–1139, 2015.

[162] Marcel Rother, Stefan P Schießl, Yuriy Zakharko, Florentina Gannott, and Jana Zaumseil.
Understanding charge transport in mixed networks of semiconducting carbon nanotubes.
ACS applied materials & interfaces, 8(8):5571–5579, 2016.

[163] Widianta Gomulya, Jorge Mario Salazar Rios, Vladimir Derenskyi, Satria Zulkarnaen Bisri, Stefan Jung, Martin Fritsch, Sybille Allard, Ullrich Scherf, Maria Cristina dos Santos, and Maria Antonietta Loi.

Effect of temperature on the selection of semiconducting single walled carbon nanotubes using poly (3-dodecylthiophene-2, 5-diyl).
Carbon, 84:66–73, 2015.

[164] Jason K Streit, Sergei M Bachilo, Saunab Ghosh, Ching-Wei Lin, and R Bruce Weisman.
Directly measured optical absorption cross sections for structure-selected single-walled carbon nanotubes.
Nano letters, 14(3):1530–1536, 2014.

[165] Jianfu Ding, Zhao Li, Jacques Lefebvre, Fuyong Cheng, Girjesh Dubey, Shan Zou, Paul Finnie, Amy Hrdina, Ludmila Scoles, Gregory P Lopinski, et al.
Enrichment of large-diameter semiconducting swcnts by polyfluorene extraction for high network density thin film transistors.
Nanoscale, 6(4):2328–2339, 2014.

[166] Frank Hennrich, Ralph Krupke, Katharina Arnold, Jan A Rojas Stütz, Sergei Lebedkin, Thomas Koch, Thomas Schimmel, and Manfred M Kappes.
The mechanism of cavitation-induced scission of single-walled carbon nanotubes.
The Journal of Physical Chemistry B, 111(8):1932–1937, 2007.

[167] Yasumitsu Miyata, Kazunari Shiozawa, Yuki Asada, Yutaka Ohno, Ryo Kitaura, Takashi Mizutani, and Hisanori Shinohara.
Length-sorted semiconducting carbon nanotubes for high-mobility thin film transistors.
Nano Research, 4(10):963–970, 2011.

[168] A Ishii, M Yoshida, and YK Kato.
Exciton diffusion, end quenching, and exciton-exciton annihilation in individual air-suspended carbon nanotubes.
Physical Review B, 91(12):125427, 2015.

[169] Ninette Sturzl, Sergei Lebedkin, and Manfred M Kappes.
Revisiting the laser dye styryl-13 as a reference near-infrared fluorophore: implications for the photoluminescence quantum yields of semiconducting single-walled carbon nanotubes.
The Journal of Physical Chemistry A, 113(38):10238–10240, 2009.

[170] Matthias Kastner, Sabine Stahl, Ivonne Vollert, Christian Loi, Nicolas Rühl, Tobias Hertel, and Friedrich Schöppler.
A comparison of raman and photoluminescence spectra for the assessment of single-wall carbon nanotube sample quality.
Chemical Physics Letters, 635:245–249, 2015.

[171] Samsung.
http://www.samsung.com/uk/tvs/curved-oled-s9c/, visited on 2017-12-12.

[172] Andrea Zampetti, Alessandro Minotto, Benedetta Maria Squeo, Vasilis G Gregoriou, Sybille Allard, Ullrich Scherf, Christos L Chochos, and Franco Cacialli.
Highly efficient solid-state near-infrared organic light-emitting diodes incorporating ada dyes based on α, β-unsubstituted "bodipy" moieties.
Scientific reports, 7(1):1611, 2017.

[173] Zhi Yuan Wang.
Near-infrared organic materials and emerging applications.
CRC press, 2013.

[174] Gang Qian, Ze Zhong, Min Luo, Dengbin Yu, Zhiqiang Zhang, Zhi Yuan Wang, and Dongge Ma.
Simple and efficient near-infrared organic chromophores for light-emitting diodes with single electroluminescent emission above 1000 nm.
Advanced Materials, 21(1):111–116, 2009.

[175] Fei Yan, Wenlian Li, Bei Chu, Huihui Liu, Guang Zhang, Zisheng Su, Jianzhuo Zhu, Liangliang Han, Tianle Li, Yiren Chen, et al.
Sensitized infrared electrophosphorescence based on divalent copper complex by an iridium (iii) complex.
Organic Electronics, 10(7):1408–1411, 2009.

[176] Afshin Shahalizad, Anthony D'aléo, Chantal Andraud, Muhammad Hasnan Sazzad, Dae-Hyeon Kim, Youichi Tsuchiya, Jean-Charles Ribierre, Jean-Michel Nunzi, and Chihaya Adachi.
Near infrared electroluminescence from nd (tta) 3phen in solution-processed small molecule organic light-emitting diodes.
Organic Electronics, 44:50–58, 2017.

[177] Ryo Nagata, Hajime Nakanotani, and Chihaya Adachi.
Near-infrared electrophosphorescence up to 1.1 μm using a thermally activated delayed fluorescence molecule as triplet sensitizer.
Advanced Materials, 29(5):1604265, 2017.

[178] Giulia Tregnago, Timothy T Steckler, Oliver Fenwick, Mats R Andersson, and Franco Cacialli.
Thia-and selena-diazole containing polymers for near-infrared light-emitting diodes.
Journal of Materials Chemistry C, 3(12):2792–2797, 2015.

[179] Nir Tessler, Vlad Medvedev, Miri Kazes, ShiHai Kan, and Uri Banin.
Efficient near-infrared polymer nanocrystal light-emitting diodes.
Science, 295(5559):1506–1508, 2002.

[180] Xiwen Gong, Zhenyu Yang, Grant Walters, Riccardo Comin, Zhijun Ning, Eric Beauregard, Valerio Adinolfi, Oleksandr Voznyy, and Edward H Sargent.
Highly efficient quantum dot near-infrared light-emitting diodes.
Nature Photonics, 10(4):253, 2016.

[181] Manuel Schweiger, Yuriy Zakharko, Florentina Gannott, Stefan B Grimm, and Jana Zaumseil.
Photoluminescence enhancement of aligned arrays of single-walled carbon nanotubes by polymer transfer.
Nanoscale, 7(40):16715–16720, 2015.

[182] Yuhei Miyauchi.
Photoluminescence studies on exciton photophysics in carbon nanotubes.
Journal of Materials Chemistry C, 1(40):6499–6521, 2013.

[183] Amanda R Amori, Zhentao Hou, and Todd D Krauss.
Excitons in single-walled carbon nanotubes and their dynamics.
Annual review of physical chemistry, 69:81–99, 2018.

[184] Angela Eckstein, Renata Karpicz, Ramūnas Augulis, Kipras Redeckas, Mikas Vengris, Imge Namal, Tobias Hertel, and Vidmantas Gulbinas.
Excitation quenching in polyfluorene polymers bound to (6, 5) single-wall carbon nanotubes.
Chemical Physics, 467:1–5, 2016.

[185] Mauro Furno, Rico Meerheim, Simone Hofmann, Björn Lüssem, and Karl Leo.
Efficiency and rate of spontaneous emission in organic electroluminescent devices.
Physical Review B, 85(11):2074, 2012.

[186] Charles Möhl, Arko Graf, Felix J Berger, Jan Lüttgens, Yuriy Zakharko, Victoria Lumsargis, Malte C Gather, and Jana Zaumseil.
Trion-polariton formation in single-walled carbon nanotube microcavities.
ACS Photonics, 5(6):115205, 2018.

[187] Holger Hartleb, Florian Späth, and Tobias Hertel.
Evidence for strong electronic correlations in the spectra of gate-doped single-wall carbon nanotubes.
ACS nano, 9(10):10461–10470, 2015.

[188] Ryusuke Matsunaga, Kazunari Matsuda, and Yoshihiko Kanemitsu.
Observation of charged excitons in hole-doped carbon nanotubes using photoluminescence and absorption spectroscopy.
Physical review letters, 106(3):037404, 2011.

[189] Arko Graf, Philipp Liehm, Caroline Murawski, Simone Hofmann, Karl Leo, and Malte Christian Gather.
Correlating the transition dipole moment orientation of phosphorescent emitter molecules in oleds with basic material properties.
Journal of Materials Chemistry C, 2(48):10298–10304, 2014.

[190] Lieven Penninck, Frank Steinbacher, Ralf Krause, and Kristiaan Neyts.
Determining emissive dipole orientation in organic light emitting devices by decay time measurement.
Organic Electronics, 13(12):3079–3084, 2012.

[191] Kouta Watanabe and Kenichi Asano.
Trions in semiconducting single-walled carbon nanotubes.
Physical Review B, 85(3):035416, 2012.

[192] Caroline Murawski, Karl Leo, and Malte C Gather.
Efficiency roll-off in organic light-emitting diodes.
Advanced Materials, 25(47):6801–6827, 2013.

[193] Yuhei Miyauchi, Munechiyo Iwamura, Shinichiro Mouri, Tadashi Kawazoe, Motoichi Ohtsu, and Kazunari Matsuda.
Brightening of excitons in carbon nanotubes on dimensionality modification.
Nature Photonics, 7(9):715, 2013.

[194] Qing Hua Wang and Michael S Strano.
Carbon nanotubes: A bright future for defects.
Nature chemistry, 5(10):812, 2013.

[195] Ryosuke Watahiki, Takashi Shimada, Pei Zhao, Shohei Chiashi, Satoshi Iwamoto, Yasuhiko Arakawa, Shigeo Maruyama, and Yuichiro K Kato.
Enhancement of carbon nanotube photoluminescence by photonic crystal nanocavities.
Applied Physics Letters, 101(14):141124, 2012.

[196] Adrien Jeantet, Yannick Chassagneux, Christophe Raynaud, Ph Roussignol, Jean-Sébastien Lauret, Benjamin Besga, Jérôme Estève, Jakob Reichel, and Christophe Voisin.
Widely tunable single-photon source from a carbon nanotube in the purcell regime.
Physical review letters, 116(24):247402, 2016.

[197] Marlene Glauser, Christian Mounir, Georg Rossbach, Eric Feltin, Jean-François Carlin, Raphaël Butté, and Nicolas Grandjean.
Ingan/gan quantum wells for polariton laser diodes: Role of inhomogeneous broadening.
Journal of Applied Physics, 115(23):233511, 2014.

[198] I Diniz, S Portolan, R Ferreira, JM Gérard, Patrice Bertet, and A Auffeves.
Strongly coupling a cavity to inhomogeneous ensembles of emitters: Potential for long-lived solid-state quantum memories.
Physical Review A, 84(6):063810, 2011.

[199] Richard T Grant, Paolo Michetti, Andrew J Musser, Pascal Gregoire, Tersilla Virgili, Eleonora Vella, Marco Cavazzini, Kyriacos Georgiou, Francesco Galeotti, Caspar Clark, et al.
Efficient radiative pumping of polaritons in a strongly coupled microcavity by a fluorescent molecular dye.
Advanced Optical Materials, 4(10):1615–1623, 2016.

[200] CE Finlayson, G Vijaya Prakash, and JJ Baumberg.
Strong exciton-photon coupling in a length tunable optical microcavity with j-aggregate dye heterostructures.
Applied Physics Letters, 86(4):041110, 2005.

[201] S Dufferwiel, S Schwarz, F Withers, AAP Trichet, F Li, M Sich, O Del Pozo-Zamudio, C Clark, A Nalitov, DD Solnyshkov, et al.
Exciton–polaritons in van der waals heterostructures embedded in tunable microcavities.
Nature communications, 6:8579, 2015.

[202] Sinan Balci, Coskun Kocabas, Simge Ates, Ertugrul Karademir, Omer Salihoglu, and Atilla Aydinli.
Tuning surface plasmon-exciton coupling via thickness dependent plasmon damping.
Physical Review B, 86(23):235402, 2012.

[203] Martin Held, Arko Graf, Yuriy Zakharko, Pengning Chao, Laura Tropf, Malte C Gather, and Jana Zaumseil.
Ultrastrong coupling of electrically pumped near-infrared exciton-polaritons in high mobility polymers.
Advanced Optical Materials, 6(3):1700962, 2018.

[204] Tal Galfsky, Harish Krishnamoorthy, Ward D Newman, Evgenii Narimanov, Zubin Jacob, and Vinod M Menon.
Directional emission from quantum dots in a hyperbolic metamaterial.
In *CLEO: QELS_Fundamental Science*, pages FTu3C–6. Optical Society of America, 2014.

[205] Jacek Kasprzak, M Richard, S Kundermann, A Baas, P Jeambrun, JMJ Keeling, FM Marchetti, MH Szymańska, R Andre, JL Staehli, et al.
Bose–einstein condensation of exciton polaritons.
Nature, 443(7110):409, 2006.

[206] Alexander JC Kuehne and Malte C Gather.
Organic lasers: recent developments on materials, device geometries, and fabrication techniques.
Chemical reviews, 116(21):12823–12864, 2016.

[207] Deepak Venkateshvaran, Mark Nikolka, Aditya Sadhanala, Vincent Lemaur, Mateusz Zelazny, Michal Kepa, Michael Hurhangee, Auke Jisk Kronemeijer, Vincenzo Pecunia, Iyad Nasrallah, et al.
Approaching disorder-free transport in high-mobility conjugated polymers.
Nature, 515(7527):384, 2014.

[208] AO Slobodeniuk and DM Basko.
Exciton-phonon relaxation bottleneck and radiative decay of thermal exciton reservoir in two-dimensional materials.
Physical Review B, 94(20):205423, 2016.

[209] PG Lagoudakis, MD Martin, JJ Baumberg, A Qarry, E Cohen, and LN Pfeiffer.
Electron-polariton scattering in semiconductor microcavities.
Physical review letters, 90(20):206401, 2003.

[210] Iacopo Carusotto and Cristiano Ciuti.
Probing microcavity polariton superfluidity through resonant rayleigh scattering.
Physical review letters, 93(16):166401, 2004.

[211] Pallab Bhattacharya, Bo Xiao, Ayan Das, Sishir Bhowmick, and Junseok Heo.
Solid state electrically injected exciton-polariton laser.
Physical review letters, 110(20):206403, 2013.

[212] Martijn Kemerink, DSH Charrier, ECP Smits, SGJ Mathijssen, DM de Leeuw, and RAJ Janssen.
On the width of the recombination zone in ambipolar organic field effect transistors.
Applied physics letters, 93(3):268, 2008.

[213] Xiaowei He, Weilu Gao, Lijuan Xie, Bo Li, Qi Zhang, Sidong Lei, John M Robinson, Erik H Hároz, Stephen K Doorn, Weipeng Wang, et al.
Wafer-scale monodomain films of spontaneously aligned single-walled carbon nanotubes.
Nature nanotechnology, 11(7):633, 2016.

[214] Bongjun Kim, Kelly Liang, Michael L Geier, Mark C Hersam, and Ananth Dodabalapur.
Enhancement of minority carrier injection in ambipolar carbon nanotube transistors using double-gate structures.
Applied Physics Letters, 109(2):023515, 2016.

[215] Yoichi Murakami and Junichiro Kono.
Nonlinear photoluminescence excitation spectroscopy of carbon nanotubes: exploring the upper density limit of one-dimensional excitons.
Physical review letters, 102(3):037401, 2009.

[216] Ch Schneider, K Winkler, MD Fraser, M Kamp, Y Yamamoto, EA Ostrovskaya, and Sven Höfling.
Exciton-polariton trapping and potential landscape engineering.
Reports on Progress in Physics, 80(1):016503, 2016.

[217] E Orgiu, J George, JA Hutchison, E Devaux, JF Dayen, B Doudin, F Stellacci, C Genet, J Schachenmayer, C Genes, et al.
Conductivity in organic semiconductors hybridized with the vacuum field.
Nature materials, 14(11):1123, 2015.

[218] Yuriy Zakharko, Arko Graf, and Jana Zaumseil.
Plasmonic crystals for strong light–matter coupling in carbon nanotubes.
Nano letters, 16(10):6504–6510, 2016.

[219] Yuriy Zakharko, Martin Held, Arko Graf, Tobias Rödlmeier, Ralph Eckstein, Gerardo Hernandez-Sosa, Bernd Hähnlein, Jörg Pezoldt, and Jana Zaumseil.
Multispectral electroluminescence enhancement of single-walled carbon nanotubes coupled to periodic nanodisk arrays.
Optics Express, 25(15):18092–18106, 2017.

[220] Yuriy Zakharko, Marcel Rother, Arko Graf, Bernd Hähnlein, Maximilian Brohmann, Jörg Pezoldt, and Jana Zaumseil.
Radiative pumping and propagation of plexcitons in diffractive plasmonic crystals.
Nano letters, 18(8):4927–4933, 2018.

[221] Felix J Berger, Thomas M Higgins, Marcel Rother, Arko Graf, Yuriy Zakharko, Sybille Allard, Maik Matthiesen, Jan M Gotthardt, Ullrich Scherf, and Jana Zaumseil.
From broadband to electrochromic notch filters with printed monochiral carbon nanotubes.
ACS applied materials & interfaces, 10(13):11135–11142, 2018.

[222] Andreas Malhofer, Marcel Rother, Yuriy Zakharko, Arko Graf, Stefan P Schießl, and Jana Zaumseil.

Direct visualization of percolation paths in carbon nanotube/polymer composites.
Organic Electronics, 45:151–158, 2017.

[223] Marcel Rother, Adelaide Kruse, Maximilian Brohmann, Maik Matthiesen, Sebastian Grieger, Thomas M Higgins, and Jana Zaumseil.
Vertical electrolyte-gated transistors based on printed single-walled carbon nanotubes.
ACS Applied Nano Materials, 1(7):3616–3624, 2018.

[224] Maximilian Brohmann, Marcel Rother, Stefan P Schießl, Eduard Preis, Sybille Allard, Ullrich Scherf, and Jana Zaumseil.
Temperature-dependent charge transport in polymer-sorted semiconducting carbon nanotube networks with different diameter distributions.
The Journal of Physical Chemistry C, 122(34):19886–19896, 2018.

[225] Severin Schneider, Maximilian Brohmann, Roxana Lorenz, Yvonne J Hofstetter, Marcel Rother, Eric Sauter, Michael Zharnikov, Yana Vaynzof, Hans-Joerg Himmel, and Jana Zaumseil.
Efficient n-doping and hole-blocking in single-walled carbon nanotube transistors with 1, 2, 4, 5-tetrakis (tetramethyl-guanidino) benzene.
ACS nano, 2(6):5895–5902, 2018.

[226] Nicolai F Hartmann, Kirill A Velizhanin, Erik H Haroz, Mijin Kim, Xuedan Ma, YuHuang Wang, Han Htoon, and Stephen K Doorn.
Photoluminescence dynamics of aryl sp3 defect states in single-walled carbon nanotubes.
ACS nano, 10(9):8355–8365, 2016.

[227] Marcus Freitag, Jia Chen, J Tersoff, James C Tsang, Qiang Fu, Jie Liu, and Phaedon Avouris.
Mobile ambipolar domain in carbon-nanotube infrared emitters.
Physical Review Letters, 93(7):076803, 2004.

[228] JA Misewich, R Martel, Ph Avouris, JC Tsang, S Heinze, and J Tersoff.
Electrically induced optical emission from a carbon nanotube fet.
Science, 300(5620):783–786, 2003.

[229] Weilu Gao, Xinwei Li, Motoaki Bamba, and Junichiro Kono.
Continuous transition between weak and ultrastrong coupling through exceptional points in carbon nanotube microcavity exciton-polaritons.
Nature Photonics, 12:362–367, 2018.

[230] Simone De Liberato.
Light-matter decoupling in the deep strong coupling regime: The breakdown of the purcell effect.

Physical review letters, 112(1):016401, 2014.

[231] Darius Urbonas, Thilo Stöferle, Fabio Scafirimuto, Ullrich Scherf, and Rainer F Mahrt.
Zero-dimensional organic exciton–polaritons in tunable coupled gaussian defect microcavities at room temperature.
ACS Photonics, 3(9):1542–1545, 2016.

[232] Ben BY Hsu, Chunhui Duan, Ebinazar B Namdas, Andrea Gutacker, Jonathan D Yuen, Fei Huang, Yong Cao, Guillermo C Bazan, Ifor DW Samuel, and Alan J Heeger.
Control of efficiency, brightness, and recombination zone in light-emitting field effect transistors.
Advanced Materials, 24(9):1171–1175, 2012.

[233] Gerald J Brady, Yongho Joo, Susmit Singha Roy, Padma Gopalan, and Michael S Arnold.
High performance transistors via aligned polyfluorene-sorted carbon nanotubes.
Applied Physics Letters, 104(8):083107, 2014.

[234] Felix Pyatkov, Valentin Fütterling, Svetlana Khasminskaya, Benjamin S Flavel, Frank Hennrich, Manfred M Kappes, Ralph Krupke, and Wolfram HP Pernice.
Cavity-enhanced light emission from electrically driven carbon nanotubes.
Nature Photonics, 10(6):420, 2016.

[235] Xuedan Ma, Nicolai F Hartmann, Jon KS Baldwin, Stephen K Doorn, and Han Htoon.
Room-temperature single-photon generation from solitary dopants of carbon nanotubes.
Nature nanotechnology, 10(8):671, 2015.

Eidesstattliche Versicherung

Eidesstattliche Versicherung gemäß §8 der Promotionsordnung der Naturwissenschaftlich-Mathematischen Gesamtfakultät der Universität Heidelberg:

Bei der eingereichten Dissertation zu dem Thema strong light-matter interactions and exciton-polaritons in carbon nanotubes handelt es sich um meine eigenständig erbrachte Leistung.

Ich habe nur die angegebenen Quellen und Hilfsmittel benutzt und mich keiner unzulässigen Hilfe Dritter bedient. Insbesondere habe ich wörtlich oder sinngemäß aus anderen Werken übernommene Inhalte als solche kenntlich gemacht.

Die Arbeit oder Teile davon habe ich nicht an einer Hochschule des In- oder Auslands als Bestandteil einer Prüfungs- oder Qualifikationsleitung vorgelegt.

Die Richtigkeit der vorstehenden Erklärungen bestätige ich.

Die Bedeutung der eidesstattlichen Versicherung und die strafrechtlichen Folgen einer unrichtigen oder unvollständigen eidesstattlichen Versicherung sind mir bekannt.

Ich versichere an Eides statt, dass ich nach bestem Wissen die reine Wahrheit erklärt und nichts verschwiegen habe.

Ort, Datum: ..... Unterschrift: .....

I got a Ph.D. in how to make ends meet

(Money is, Quincy Jones)